Electrical Transport in Thin Film Systems for Energy Harvesting

by

Bingyuan Huang

A dissertation submitted in partial fulfillment
of the requirements for the degree of
Doctor of Philosophy
(Materials Science and Engineering)
in the University of Michigan
2014

Doctoral Committee:

Professor Peter F. Green, Chair
Assistant Professor Akram I. Boukai
Associate Professor Jinsang Kim
Associate Professor Pramod S. Reddy

To my late maternal grandfather

ACKNOWLEDGEMENTS

Now that I am approaching the very end of my PhD and starting to look back, things that fade into the past resurface once more. The whole degree pursuit is not only a demanding intellectual quest, but also a long process of self-awareness for me. Both research and life taught me a lot and I have to admit that some lessons were learned in a very hard way. Very luckily, I have never been alone over the time and have received attention, help and care from many people, to whom I feel deeply indebted and want to express my wholehearted appreciation here.

Foremost, I want to say a big thank you to my advisor and mentor, Prof. Peter F. Green, for his strong support on all fronts. I still clearly remember how relieved and grateful I was when Peter accepted me into the group at my most difficult time. As an academic advisor, Peter guides me in the field of conjugated polymer research with his solid knowledge and deep insight. As a mentor, Peter is always encouraging, show full confidence on me and does his best to create open environment to accommodate my thoughts. He once told me, “You are my student. You don’t need to sign up to see me. Come and find me directly”, though he is routinely burdened with heavy administrative work. Without his true care and guidance, I would never have achieved this step.

I am also sincerely grateful to my other committee members, Prof. Akram Boukai, Prof. Jinsang Kim and Prof. Pramod Reddy for their continuous comments and suggestions throughout my work. Akram has co-advised me on the strained silicon project and I learn a lot from his academic excellence. Prof. Kim and Prof. Reddy has helped me solve many puzzles in the research with their profound knowledge in the fields. I also want to give special thanks to Prof. Barry Dunietz in the Department of Chemistry for inspiring discussion on the P3HT mobility project.

I will never forget each and every of former and current members in the Green research group as well. It is them that I truly work with every day and that give me the mostly direct help. Dr. Chelsea Chen, Dr. Bradley Frieberg, Dr. Emmanouil Glynos, Dr. Jenny Kim, Dr. Ernest McIntyre, Dr. Hyun Joon Oh, Dr. Aaron Tan, Dr. Hengxi Yang, Jojo Amonoo, Peter Chung, Ban Dong, Kyle Johnson, Anton Li, Ravi Sharma and Junnan Zhao, thank you all very much.

Many thanks to my collaborators Dr. Xiao Guo, Dr. Duck Hyun Lee, Prof. Anish Tuteja, Dr. David Bilby, Adam Barito, Matthew Sykes and Prof. Max Shtein for collaborations on many projects that deepen my material understanding.

Last but not least, I thank my families and friends, especially my beloved wife and parents, for their unreserved love and moral support during my degree. PhD degree marks an important stage I achieved so far. But it is the love and friendship with them that I cherish most throughout my life.

TABLE OF CONTENTS

LIST OF FIGURES

ABSTRACT

Many energy conversion technologies rely on the function and properties of thin films. In many cases, the fundamental physics underlying the structure-property-performance interrelationship is not completely understood. So it is not possible to fully exploit the true capabilities of these systems. Therefore, investigating and understanding such interrelationships in different systems is of both scientific and technological importance.

In this dissertation, both conjugated polymer systems for photovoltaic application and strained silicon system for thermoelectric application are investigated in order to develop a clearer understanding of the effect of film thickness and microstructural features on electrical transport. Morphological features such as domain size, phase purity are investigated in the polymers in order to understand the effects on charge mobility, recombination and further on device performance. With regard to silicon, the effects of lattice strain on electrical conductivity and thermopower are studied.

The out-of-plane hole mobility was investigated in regioregular P3HT thin films. It was shown that the hole mobilities monotonically increased an order of magnitude when film thickness increased from 80 nm to 700 nm. Based on X-ray diffraction, spectroscopic ellipsometry and simulations, this thickness-dependent mobility is associated with substrate induced anisotropies of the P3HT film structure.

The role of microstructural features on the performance characteristics of the archetypal P3HT:PCBM (1:1) bulk heterojunction solar cell was investigated. It is demonstrated that small domain sizes and correspondingly large interfacial areas accommodated a high initial carrier density. However in these materials, non-geminate recombination of carriers could be significant, leading to low open circuit voltages and low fill factors. The purity of the domains also influenced the charge carrier mobilities and non-germinate recombination. One important finding from this study is that high short circuit currents were readily achieved with smaller domain sizes than 10 nm, which is believed to the best domain size.

With regard to the thermoelectric characterizations in the strained silicon thin film possessing nanomesh topology, the electrical conductivity was found to increase several folds and the power factor doubled. This enhancement is attributed to the splitting of silicon conduction band under the biaxial tensile strain, which affects the effective mass, inter-valley scattering and energy distribution of transporting electrons.

CHAPTER 1

INTRODUCTION

1.1 BACKGROUND AND MOTIVATION

With the global population explosion and ever-growing economy, the world's energy demand continues to increase. The global primary energy demand is expected to increase by one-third from 2011 to 2035, reaching around 17400 million tonnes of oil equivalent.[1] Whether or not the future energy demands will be met by fossil fuels is unclear. Nevertheless, the consequences associated with combustion of fossil fuels, such as climate change, are certain. As a result, alternative energy sources that are efficient, non-polluting, renewable and cost effective are necessary.

Energy exists in different forms, such as electricity, light and heat. Among all various forms for different applications, electricity certainly is the utmost important form in modern society. Power generation varies over places and electricity is the most efficient and fastest way to transmit power across long distances using high voltage transmission towers. Electricity is also the most widely used energy form in industries and everyday livings. According to the International Energy Agency, demand for electricity grows faster than any other final form of energy between 2011 and 2035; the total demand will increase by two-thirds during this period with an average growing rate of 2.2-2.5% per

year.[1] It is therefore of significant importance to study and explore new sources and methods for electricity generation.

In this thesis we will primarily be concerned with thin film electricity generation technologies involving photovoltaics and thermoelectrics. In the remainder of this section, I will describe the basic photovoltaic effect in organic semiconductors and the thermoelectric effect in silicon. The next section of the chapter will be devoted to describing two experimental techniques that I used to investigate various transport processes associated with energy conversion in materials.

1.1.1 Photovoltaic systems

Solar power is one of the cleanest and most renewable energy sources. The total amount of energy that comes from sunlight onto the Earth in one hour is nearly comparable to the energy consumed on the planet in a year. The physical process of transforming sunlight into electricity is referred as photovoltaic (PV) effect. Devices operating via a mechanism based on this effect are thus called photovoltaic devices, or solar cells.

The performance of a solar cell is usually characterized by a $\boldsymbol{J}$-$\boldsymbol{V}$ curve, as shown in Figure 1.1, and its efficiency is defined by a power conversion efficiency ($\boldsymbol{PCE}$). The $\boldsymbol{PCE}$ is a standard metric used by industry to describe the solar cell performance and it is defined as the ratio of the electrical power produced by a solar cell per unit area over the power of incident light per unit area under certain standard test conditions.[2] Based on the parameters of the $\boldsymbol{J}$-$\boldsymbol{V}$ curve, $\boldsymbol{PCE}$ is defined as:

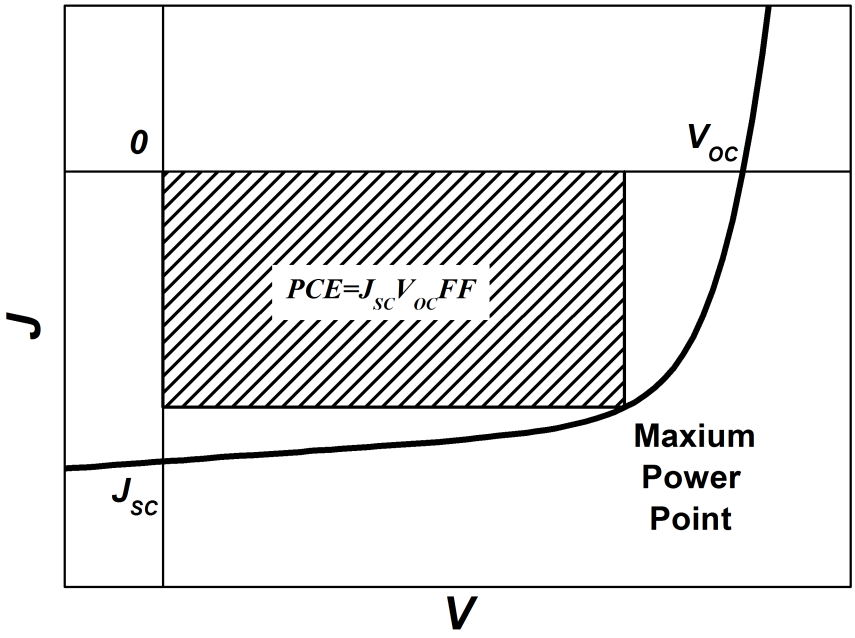

Figure 1.1 A representative J-V curve of a solar cell measured under the standard test conditions. Key parameters (J_{SC}, V_{OC}, FF) are all labeled.

$$PCE = J_{SC}V_{OC}FF \tag{1.1}$$

where J_{SC} is the short circuit current, photocurrent produced by the solar cell under no external electric field; V_{OC} is the open circuit voltage, external voltage applied across the device to fully compensate J_{SC}; and FF is the fill factor, the ratio of the most obtainable power over the product of V_{OC} and J_{SC}; all are labeled in Figure 1.1.

High efficiency solar cells have been manufactured using traditional inorganic semiconducting materials like Si or GaAs.[3] However, the fabrication of high efficiency inorganic solar cells is subject to strict processing conditions including highly controlled temperature and vacuum environments, requiring expensive manufacturing facilities worth millions of dollars. Some of these materials are also not earth abundant and limited

in supply. Moreover, the choice of inorganic materials for high efficiency solar cell performance is fairly limited.[4] Therefore, research is necessary to identify newer and more cost effective materials.

The emergence of conjugated polymers has an important impact on device technologies because of their ability to conduct electricity. Conventional polymers like polystyrene or poly(methyl methacrylate) are usually insulating because electrons are localized in the covalent bonds and do not contribute to conductivity. In contrast, conjugated polymers are materials that possess conjugation along the polymer backbone, involving an overlap of p-orbitals with intervening sigma bonds. The interjacent single bonds are thus bridged by the overlapped p-orbitals so pi electrons are delocalized in the entire conjugated region. As a result, a band structure is formed and charges can move along backbones; so conjugated polymers can therefore be either metallic or semiconducting.[5] Because of their ability to conduct charges, conjugated polymers have been broadly used in different types of solar cells including bulk heterojunction solar cell, dye-sensitized solar cell and other excitonic solar cells.[6-9] The absorption coefficients of conjugated polymers are so high that ~100 nm thick film can absorb ~90% of sunlight at peak wavelength. Therefore solar cells made from conjugated polymers are usually of thicknesses between 100 nm and 200 nm. Such thinness makes polymer solar cells much lighter in weight, more adaptable to flexible substrate, and more suitable for cheap fabrication techniques such as roll-to-roll processing, compared to their inorganic counterparts.[10-12] However, in a typical organic solar cell, the photon excited hole-electron pairs (excitons) have much higher binding energy due to the intrinsically low

dielectric constant in the organic systems and therefore cannot dissociate into free carriers immediately as in inorganic systems. Excitons can typically diffuse ~10 nm before either geminate recombination or complete dissociation.[13, 14] This relatively short exciton diffusion length, together with the aforementioned high absorption coefficient, imposes some dimensional requirements on the solar cell structure. Morphological features on this scale of tens to hundreds of nanometers are also expected to influence the electrical transport properties and further the device performance. The interrelationship between the nanoscale morphology, electrical transport properties and solar cell performance is far from being fully understood. Additional research is required to comprehend the underlying physical mechanism in order to improve device performance.

Chapters 2 and 3 are dedicated to the study of a widely used conjugated polymer, poly(3-hexylthiophene) (P3HT) and its bulk heterojunction blend with a fullerene derivation, phenyl-C61-butyric acid methyl ester (PCBM). Before discussing these studies, we described the operation of a series of experimental techniques we used to investigate physical processes in these materials.

1.1.2 Thermoelectric systems

The direct energy interconversion between heat and electricity is referred as the thermoelectric effect. More specifically, the energy transformation from temperature gradient into electric voltage is known as the Seebeck effect. Devices whose operation relies on this effect are broadly used for power generation, waste heat recovery and solid state refrigeration. One important technology for power generation is radioisotope

thermoelectric generators (RTGs) used in deep space probes.[15] Remote from the Sun where solar panels are less efficient, the RTGs can generate electricity from the heat released by the decay of some radioactive materials. Compared to conventional power generators or compression engines, thermoelectric devices contains no moving parts and thus no friction loss. As a result, they should have less energy dissipation and longer lifetime.

The total conversion efficiency of a thermoelectric device can be calculated by[16]

$$\eta = \eta_c \frac{\sqrt{1+ZT}-1}{\sqrt{1+ZT}+T_c/T_h} \tag{1.2}$$

In the above equation, η_c is the Carnot efficiency, T_c and T_h are temperatures at cold and hot ends, and ZT is a dimensionless figure of merit used to evaluate thermoelectric materials,

$$ZT = \frac{S^2\sigma}{\kappa}T \tag{1.3}$$

where S is the Seebeck coefficient or thermopower, σ is the electrical conductivity, κ is the thermal conductivity and T is the absolute temperature; $S^2\sigma$ is also known as the thermoelectric power factor. Conventional compression engines typically operate at ~30% of Carnot efficiency. Therefore, thermoelectric materials with $ZT > 2\sim3$ are desired in order for thermoelectric devices to achieve competitive efficiencies with traditional heat engines.[17]

According to equation (1.1.3), maximization of ZT relies on optimization of a set of intrinsic material properties. Since electrical and thermal conduction are always highly related in a material, these properties are actually conflicting with one another in terms

for thermoelectrics. For example, $\boldsymbol{S}$ is proportional to the effective mass $\boldsymbol{m}^*$ of the primary charge carrier in degenerate semiconductors so large $\boldsymbol{m}^*$ produces high thermopower. However, carriers with large $\boldsymbol{m}^*$ move slowly and result in low carrier mobility and electrical conductivity. Therefore, an optimal $\boldsymbol{m}^*$ is needed to strike a balance between $\boldsymbol{S}$ and $\boldsymbol{\sigma}$.[18] Charge carrier density $\boldsymbol{n}$ is also of great importance to both $\boldsymbol{S}$ and $\boldsymbol{\sigma}$. $\boldsymbol{S}$ usually has a negative dependence on $\boldsymbol{n}$ while $\boldsymbol{\sigma}$ is proportional to $\boldsymbol{n}$. Such competition also leads to a non-monotonic dependence of $\boldsymbol{ZT}$ on $\boldsymbol{n}$ and the peak typically occurs at carrier concentration between 10^{19} and 10^{21} cm^{-3} depending on the material system.[18] High $\boldsymbol{ZT}$ is thus usually found in heavily doped semiconducting materials like Bi_2Te_3, PbTe and Sb_2Te_3.

Compared to those materials, the most common semiconducting material silicon is not considered as a good thermoelectric material. Because of its fairly high thermal conductivity, bulk silicon has a very low $\boldsymbol{ZT} \approx 0.01$ at room temperature. However, by incorporating structure on a scale smaller than the phonon mean free path (~10^2 nm), the thermal conductivity can be greatly reduced and $\boldsymbol{ZT}$ can be tremendously enhanced.[19, 20] An alternative approach to improve $\boldsymbol{ZT}$ is to increase the power factor. *Ab initio* calculations have shown that compressive or tensile lattice strain has certain effects on the $\boldsymbol{m}^*$ and can improve the power factor to some extent.[21, 22] However, this idea has not been experimentally realized to our best knowledge. Chapter 4 is therefore devoted to study the effect of biaxial tensile strain in silicon thin films on the thermopower and electrical conductivity.

1.2 EXPERIMENTAL TECHNIQUES

Various experimental techniques were used to fabricate the nanoscale features in the systems and investigate both structural and electrical properties thereof. Most fabrication and investigation were completed in our own lab while some were conducted in other groups or in university facilities. X-ray diffraction and energy filtered transmission electron microscopy were done in EAML and XMAL facilities; microfabrication and scanning electron microscopy were carried out in LNF cleanroom; Raman spectroscopy was finished with help from Prof. Matzger's group in the Department of Chemistry. Discussed here are only two major techniques for electrical property characterization for the apparatus of these techniques were newly set up in the lab by the author. Details of other methods will be referred to in the following chapters accordingly.

1.2.1 Time of flight

Time of flight (ToF) technique is a well-developed and commonly used method to characterize carrier mobility in the direction normal to the substrate.[23] A scheme of the experimental setup is shown in Figure 1.2(a). A film of thickness $\boldsymbol{d}$ is sandwiched between an Al electrode and an ITO electrode, as in a typical polymer solar cell. A pulse of laser is incident to one side of the sample to generate a very thin layer (~100 nm) of excitons upon absorption by the material. The side can be either ITO or Al side depending on the ease of probing. If the laser is incident on the Al side, the Al layer needs to be thin (~20 nm) for transparency. Laser-generated excitons are then dissociated into holes and electrons under the applied external voltage $\boldsymbol{V_{dc}}$ and depending on the

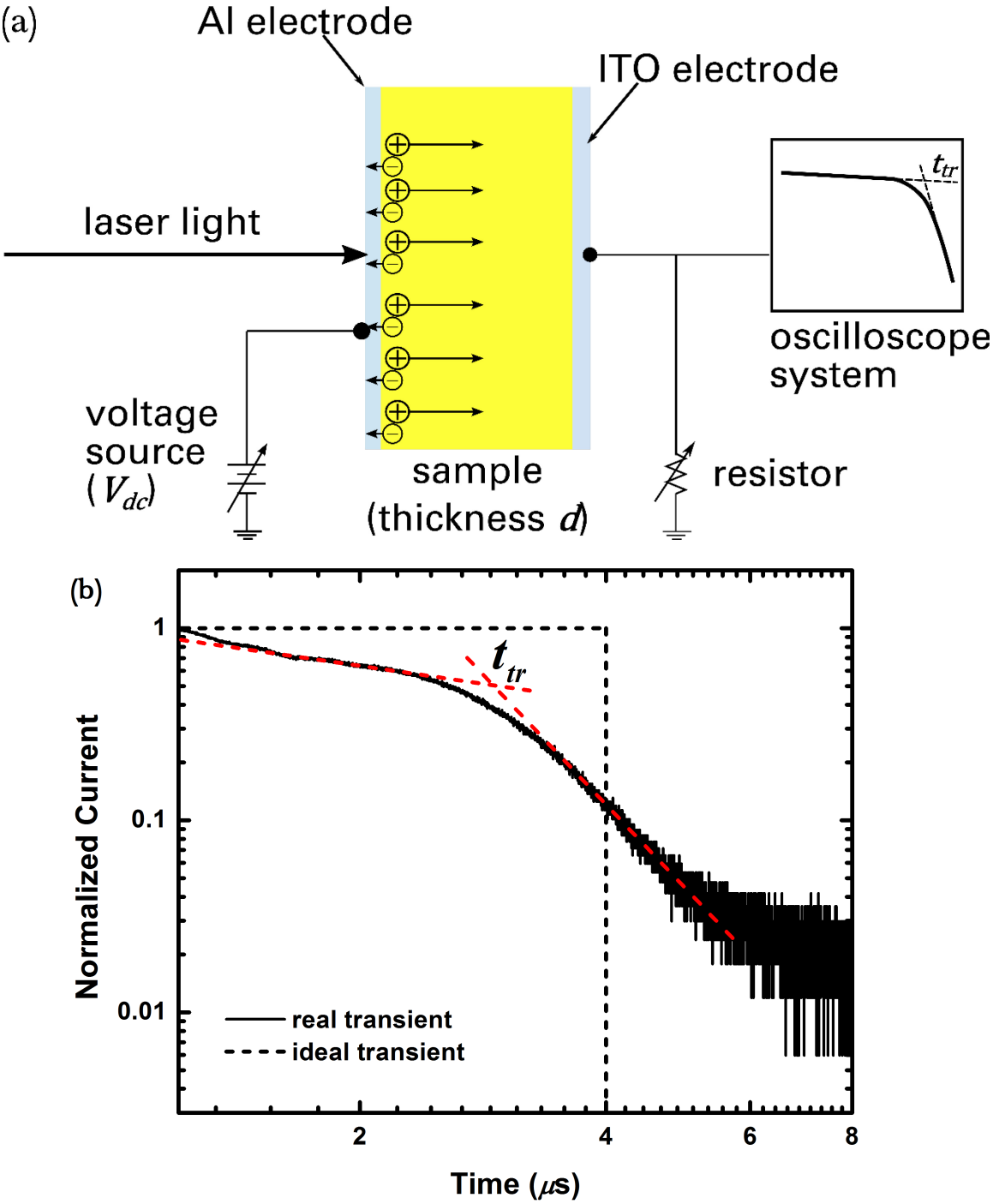

Figure 1.2 (a) A scheme of ToF experiment setup; (b) a representative ToF current transient.

voltage polarity, either holes or electrons are transported to the other side of the sample and collected by the opposite electrode. The current transient produced by such charge

carrier transport is then recorded by an oscilloscope system. Most equipment operations are automated using the LabVIEW program.

A representative ToF current transient is plotted on a double log scale as in Figure 1.2(b). If there is no trapping and carrier transport is non-dispersive (all carriers having the same mobility), the ideal current transient would be a leveled line with a turning point indicating the moment at which all carriers reach the opposite electrode, as the dashed line in Figure 1.2(b). However, trapping sites are ubiquitous in almost all practical materials and carriers always have at least a Maxwell-Boltzmann distribution of mobilities due to the thermal environment. So in a real current transient as the solid curve in Figure 1.2(b), current decreases slowly with time due largely to carrier trapping during the transport within the film; after a distinct "knee" area, the current falls faster but not steeply, meaning the collection of carriers with different mobilities at the opposite electrode. Such "knee" area can be characterized by two asymptotes to the pre-knee and post-knee curve; the crossing of these two asymptotes is defined as the transit time $\boldsymbol{t_{tr}}$ for carriers to be transported from one side of the film to the other, as indicated in Figure 1.2(b). The average carrier velocity $\boldsymbol{v}$ is then

$$\boldsymbol{v = \frac{d}{t_{tr}} = \mu E = \mu \frac{V_{dc}}{d}} \tag{1.4}$$

where $\boldsymbol{\mu}$ is the carrier mobility and $\boldsymbol{E}$ is the electric field induced by the external voltage. So $\boldsymbol{\mu}$ can be calculated by

$$\boldsymbol{\mu = \frac{d^2}{V_{dc} t_{tr}}} \tag{1.5}$$

In practice, trapped carriers in the film have the space charge effect and would disturb the uniform external electric field. In order to eliminate this, the density of generated carriers, or the laser intensity in use, should be as low as is consistent with the sensitivity of the oscilloscope. Another simple but effective way is running the laser pulses with both electrode grounded before turning on $\boldsymbol{V_{dc}}$ to collect charges.[23] Another practical convention is that since the generated carrier layer upon laser excitation is ~100 nm, the film thickness should be much larger than that in order for carriers to be transported for enough time to give a clear knee area. So ToF is usually applied to films thicker than 1 μm.[24-26]

1.2.2 Charge extraction by linearly increasing voltage

In order to overcome the limitation of the ToF technique being only able to measure carrier mobilities in thick films, a newly developed technique, charge extraction by linearly increasing voltage (CELIV), and its variant photo-CELIV are employed in the study.[27-29] The CELIV experimental setup is very similar to that of the ToF measurement without the laser, as shown in Figure 1.3(a). The sample structure is the same as that for ToF measurement with the film of interest between two electrodes. Instead of laser excitation in ToF, CELIV applies a linearly increasing voltage across the sample to extract equilibrium charge in the sample. The extracted carriers also generate a current transient, which is recorded by an oscilloscope system as well. For photo-CELIV, a laser pulse is utilized again to generate carriers, which are extracted by a linearly increasing voltage. Unlike in ToF where the applied voltage is synchronized with the excitation laser

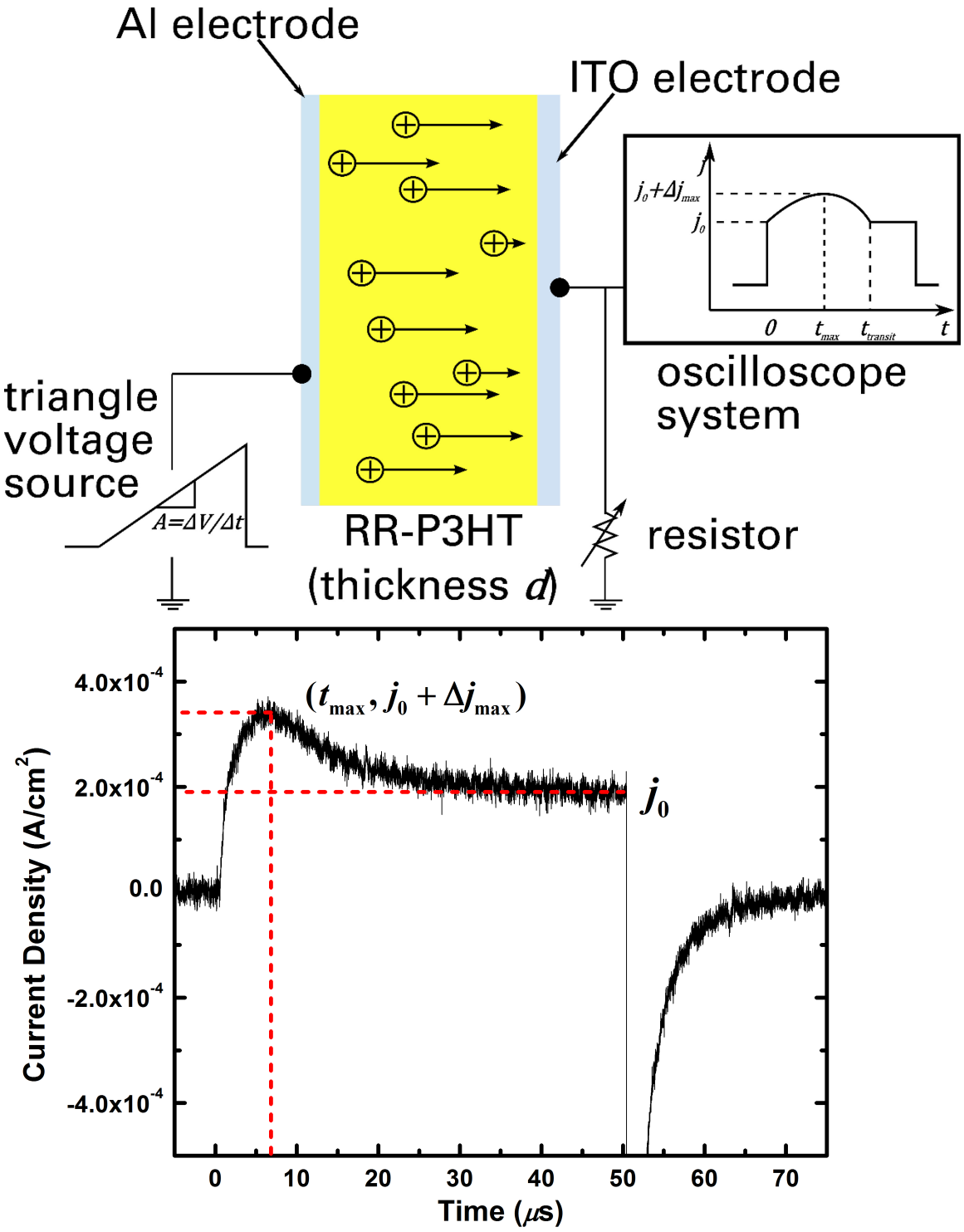

Figure 1.3 (a) A scheme of CEIV setup; (b) a typical CELIV current transient.

pulse, the onset of the increasing voltage is usually delayed from the laser pulse by a

certain period of time. Generated free carriers are confined in the sample during this delay time and recombine. So the total amount of extracted carriers decreases as the delay becomes longer. This enables photo-CELIV to characterize carrier recombination in addition to carrier mobility. Similarly to ToF, almost all operations, especially the synchronization between the laser, the applied voltage and the oscilloscope, are automated by the LabVIEW program.

A typical CELIV current transient is shown in Figure 1.3(b). Upon the start of the increasing voltage, the current transient jumps to j_0 due to the constantly changing external electric field induced by the linearly increasing voltage. This displacement current has little to do with carrier transport and is determined by the capacitance of the sample as in

$$j_0 = \varepsilon\varepsilon_0 \frac{dE}{dt} = \frac{\varepsilon\varepsilon_0}{d}\frac{dV}{dt} = \frac{A\varepsilon\varepsilon_0}{d} \tag{1.6}$$

In the above equation, ε and ε_0 are relative and vacuum permittivity, d is the film thickness and A is the voltage changing slope. As the voltage ramps, carriers are extracted out so the carrier density is lower in the sample, while higher voltage gives higher carrier conductivity. These two competing properties give rise to the peak of the drift current. By solving the continuity, current and Poisson equations, an analytic solution of the carrier mobility is obtained[27]

$$\mu = \frac{2d^2}{3At_{max}^2} \tag{1.7}$$

where t_{max} is the current peak time, as labeled in Figure 1.3(b). In practice, a numerically estimated correction factor arising from calculating the extraction length is included for mobility estimation:[28]

$$\mu = \frac{2d^2}{3At_{max}^2(1+0.36\frac{\Delta j_{max}}{j_0})} \quad (1.8)$$

Compared to ToF, CELIV analytical model takes the self-field of carriers into consideration and is less strict with the film thickness; thin films down to ~100 nm can be accurately measured by CELIV provided that equilibrium carriers are enough at test temperature to distinguish the drift current from the displacement current. However, CELIV is not selective about the carriers probed as in ToF; the measured value is a convolution of mobilities of holes and electrons if they have similar mobilities.

1.3 STUDY SCOPE

As mentioned earlier, conjugated polymer system for photovoltaic application and strained silicon system for thermoelectric application have been studied and will be discussed in the following chapters. These systems are all composed of thin films with thicknesses between 1 and 10^2 nm while the areas are macroscopic.

To be specific, Chapter 2 will discuss the effect of a film thickness dependent structural evolution on the out-of-plane hole mobility in neat P3HT films. An order of magnitude enhancement of the mobility is shown to be caused by the change of P3HT aggregate orientations.

Chapter 3 will discuss the role of domain size and phase purity on the initial carrier density, recombination and carrier mobility in P3HT:PCBM bulk heterojunction solar cells. Largest $\boldsymbol{J_{SC}}$ is found in supercritical CO_2 ($scCO_2$) processed device where high phase purity gives high carrier mobility and large interfacial areas produces most initial carriers. $\boldsymbol{V_{OC}}$ and $\boldsymbol{FF}$ are affected by fast recombination though.

Chapter 4 will discuss how biaxial tensile strain affects the silicon band structure and improves the power factor in silicon thin films with nanomesh structure. Electrical conductivity is shown to increase by several folds and the power factor is doubled.

1.4 REFERENCES

1. IEA, Global energy trends to 2035. In *World Energy Look 2013*, IEA: 2013.
2. ASTM Standard G173, Standard Tables for Reference Solar Spectral Irradiances: Direct Normal and Hemispherical on 37° Tilted Surface. In ASTM International: West Conshohocken, PA, 2012.
3. Green, M. A.; Emery, K.; Hishikawa, Y.; Warta, W.; Dunlop, E. D. *Progress in Photovoltaics: Research and Applications* **2013,** 21, (1), 1-11.
4. Goetzberger, A.; Hebling, C.; Schock, H.-W. *Materials Science and Engineering: R: Reports* **2003,** 40, (1), 1-46.
5. Inzelt, G., *Conducting Polymers*. Springer Berlin Heidelberg: 2012.
6. Sariciftci, N. S.; Smilowitz, L.; Heeger, A. J.; Wudl, F. *Science* **1992,** 258, (5087), 1474-1476.
7. Brabec, C. J.; Sariciftci, N. S.; Hummelen, J. C. *Advanced Functional Materials* **2001,** 11, (1), 15-26.
8. Gratzel, M. *Nature* **2001,** 414, (6861), 338-344.
9. Gregg, B. A. *The Journal of Physical Chemistry B* **2003,** 107, (20), 4688-4698.
10. Coakley, K. M.; McGehee, M. D. *Chemistry of Materials* **2004,** 16, (23), 4533-4542.
11. Krebs, F. C.; Gevorgyan, S. A.; Gholamkhass, B.; Holdcroft, S.; Schlenker, C.; Thompson, M. E.; Thompson, B. C.; Olson, D.; Ginley, D. S.; Shaheen, S. E.; Alshareef, H. N.; Murphy, J. W.; Youngblood, W. J.; Heston, N. C.; Reynolds, J. R.; Jia, S.; Laird, D.; Tuladhar, S. M.; Dane, J. G. A.; Atienzar, P.; Nelson, J.; Kroon, J. M.; Wienk, M. M.; Janssen, R. A. J.; Tvingstedt, K.; Zhang, F.; Andersson, M.; Inganäs, O.; Lira-Cantu, M.; de Bettignies, R.; Guillerez, S.; Aernouts, T.; Cheyns, D.; Lutsen, L.; Zimmermann, B.; Würfel, U.; Niggemann, M.; Schleiermacher, H.-F.; Liska, P.; Grätzel, M.; Lianos, P.; Katz, E. A.; Lohwasser, W.; Jannon, B. *Solar Energy Materials and Solar Cells* **2009,** 93, (11), 1968-1977.
12. Deibel, C.; Dyakonov, V. *Reports on Progress in Physics* **2010,** 73, (9), 096401.
13. Shaw, P. E.; Ruseckas, A.; Samuel, I. D. W. *Advanced Materials* **2008,** 20, (18), 3516-3520.
14. Marsh, R. A.; Hodgkiss, J. M.; Albert-Seifried, S.; Friend, R. H. *Nano Letters* **2010,** 10, (3), 923-930.
15. B.C. Blanke, J. H. B., K.C. Jordan, E.L. Murphy *Nuclear battery-thermocouple type summary report*; Monsanto Research Corporation: January 15 1962.
16. Hochbaum, A. I.; Yang, P. *Chemical Reviews* **2009,** 110, (1), 527-546.
17. Majumdar, A. *Science* **2004,** 303, (5659), 777-778.
18. Snyder, G. J.; Toberer, E. S. *Nat Mater* **2008,** 7, (2), 105-114.
19. Boukai, A. I.; Bunimovich, Y.; Tahir-Kheli, J.; Yu, J.-K.; Goddard Iii, W. A.; Heath, J. R. *Nature* **2008,** 451, (7175), 168-171.
20. Tang, J.; Wang, H.-T.; Lee, D. H.; Fardy, M.; Huo, Z.; Russell, T. P.; Yang, P. *Nano Letters* **2010,** 10, (10), 4279-4283.
21. Maegawa, T.; Yamauchi, T.; Hara, T.; Tsuchiya, H.; Ogawa, M. *Electron Devices, IEEE Transactions on* **2009,** 56, (4), 553-559.

22. Hinsche, N. F.; Mertig, I.; Zahn, P. *Journal of Physics: Condensed Matter* **2011,** 23, (29), 295502.
23. Spear, W. E. *Journal of Non-Crystalline Solids* **1969,** 1, (3), 197-214.
24. Kaneto, K.; Hatae, K.; Nagamatsu, S.; Takashima, W.; Pandey, S. S.; Endo, K.; Rikukawa, M. *Jpn. J. Appl. Phys. Part 2 - Lett.* **1999,** 38, (10B), L1188-L1190.
25. Mozer, A. J.; Sariciftci, N. S. *Chemical Physics Letters* **2004,** 389, (4-6), 438-442.
26. Ballantyne, A. M.; Chen, L.; Dane, J.; Hammant, T.; Braun, F. M.; Heeney, M.; Duffy, W.; McCulloch, I.; Bradley, D. D. C.; Nelson, J. *Advanced Functional Materials* **2008,** 18, (16), 2373-2380.
27. Juška, G.; Arlauskas, K.; Viliūnas, M.; Kočka, J. *Physical Review Letters* **2000,** 84, (21), 4946-4949.
28. Juška, G.; Arlauskas, K.; Viliūnas, M.; Genevičius, K.; Österbacka, R.; Stubb, H. *Physical Review B* **2000,** 62, (24), R16235-R16238.
29. Pivrikas, A.; Sariciftci, N. S.; Juška, G.; Österbacka, R. *Progress in Photovoltaics: Research and Applications* **2007,** 15, (8), 677-696.

CHAPTER 2

EFFECT OF THICKNESS-DEPENDENT STRUCTURAL EVOLUTION ON OUT-OF-PLANE HOLE MOBILITY IN POLY(3-HEXYLTHIOPHENE) FILMS

2.1 INTRODUCTION

As organic semiconductors, conjugated polymers are of great importance for various solid state electronic devices that include field-effect transistors (FETs), light emitting diodes (LEDs) and solar cells.[1-4] Benefits of organic materials for devices include cost effective and low-temperature processing strategies such as spin coating, drop casting, inkjet printing and roll-to-roll manufacturing.[5] However, compared to their inorganic counterparts, such as silicon and germanium, one major limitation of many conjugated polymers is their intrinsically low carrier mobilities, associated with the effects of chemical bonding rendering the carrier transport to occur via hopping among localized sites.

The charge carrier mobility impacts the performance of electronic devices in different ways. In organic LEDs, the imbalance between hole and electron mobilities in the recombination layer is responsible for charge build-up and impairs the external

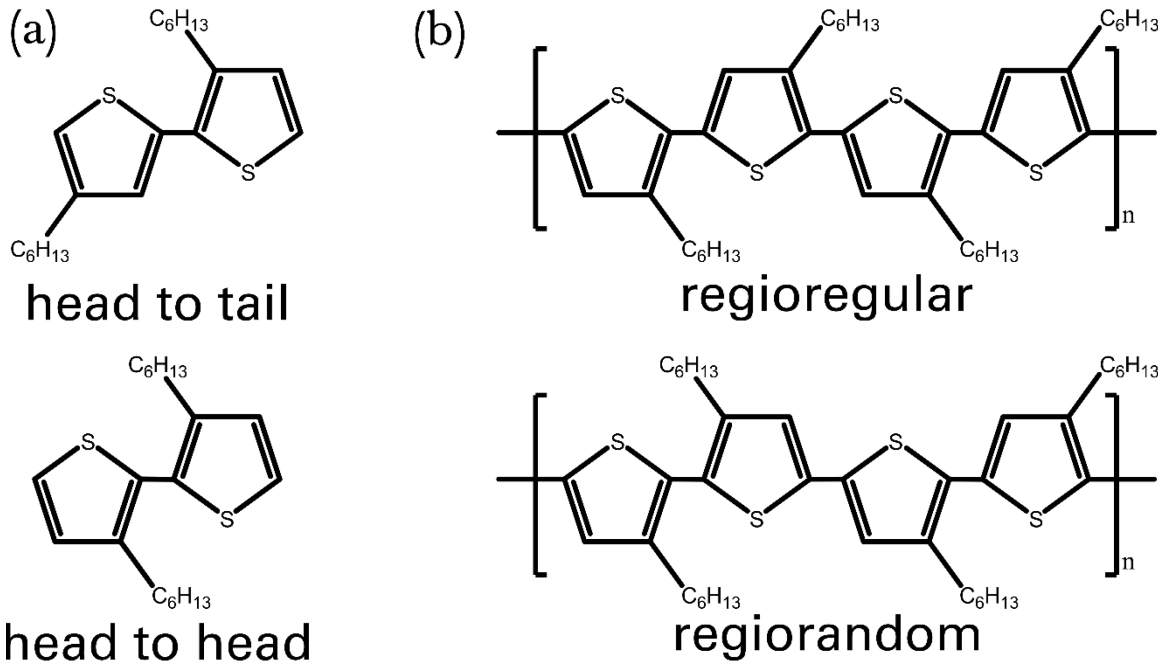

Figure 2.1 Molecular structures of (a) two regioregularities of 3-hexylthiophene and (b) regioregular and regiorandom P3HT.

quantum efficiency.[6] In polymer FETs, inherently low charge carrier mobility restricts switching speeds.[7] In solar cells, key parameters, such as $\boldsymbol{J_{SC}}$, $\boldsymbol{FF}$ and consequently $\boldsymbol{PCE}$, are also affected by charge carrier mobilities.[3,8,9] Therefore, accurate characterization of carrier mobilities and a thorough understanding of the connection between carrier mobility and film morphology is important for both scientific and technological reasons.[10-13]

One conjugated polymer of significant scientific and technological interest is poly(3-hexylthiophene) (P3HT). The incorporation of 3-hexyl substitutes into the polymer chain has two regioregularities: head to tail (HT) and head to head (HH), as shown in Figure 2.1(a). Regioregular P3HT (RR-P3HT) consists of only one kind of 3-hexylthiophene while regiorandom P3HT has both HT and HH 3-hexylthiophenes in a

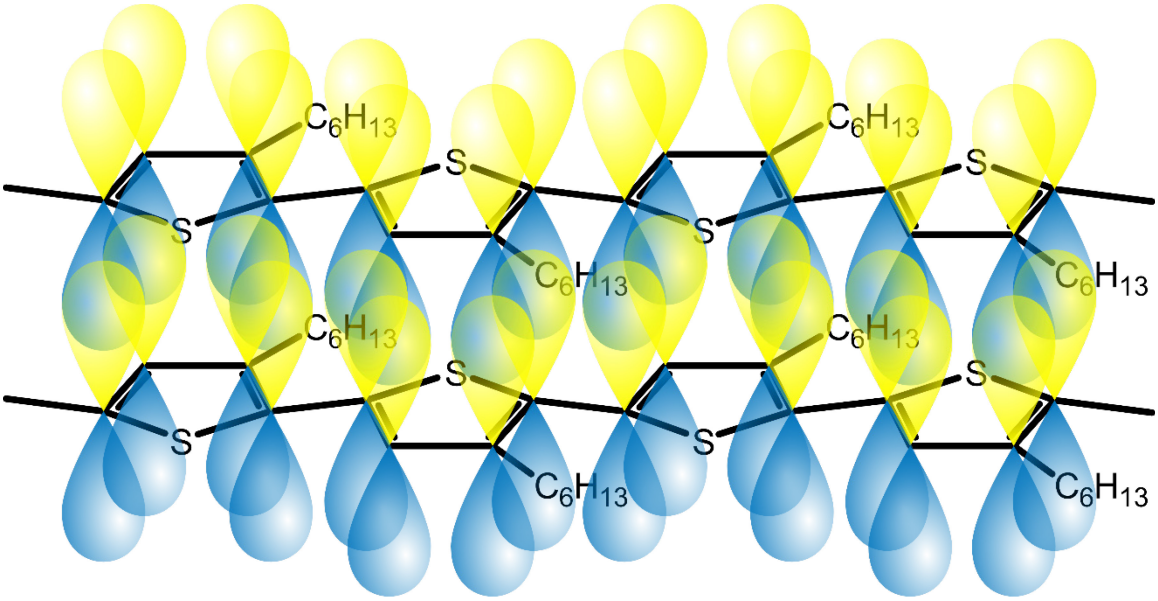

Figure 2.2 A scheme of π-π coupling between different polymer chains in a lamellar structure of a P3HT aggregate.

random pattern; both are shown in Figure 2.1(b). The hexyl functional groups improve the solubility and thus the solution processability of the polymer.[14] Structure-controlled syntheses have developed to successfully obtain RR-P3HT with HT regioregularity greater than 98.5%.[15, 16] Compared to the regiorandom one, RR-P3HT has relatively high hole mobilities for conjugated polymers, reported to be as high as 0.1 $cm^2V^{-1}s^{-1}$,[17] and has been widely used in FETs and solar cells.[18-20] Such high hole mobilities originate from the self-assembled lamellar structure of polymer chains in thin films.

RR-P3HT forms a semicrystalline structure in thin films. In the crystalline phase, the backbones of the chains of this planar shaped macromolecule self-organize to form layers, each of which stack in the π-π coupling direction to create a lamellar structure, as shown in Figure 2.2. The π-π coupling direction is orthogonal to the alkyl chain stacking direction and the strong π-π conjugation gives rise to a much higher hole mobility.[17] The

lamellae possess an "edge-on" orientation with the substrate when the π-π coupling direction is parallel to the substrate. When the π-π coupling direction is perpendicular to the substrate, the lamellae are oriented "face-on" to the substrate. Hole mobilities are much lower in the direction normal to the substrate than in the direction parallel to the substrate when the lamellae are oriented edge-on.

Generally, the absolute hole mobilities in RR-P3HT thin films depend on factors that include molecular weight,[21, 22] solvent processing conditions,[20] annealing conditions[23] and even film thickness,[24-27] all of which influence the morphology of the film. The latter, film thickness, has been a topic of controversy for some time. Measurements of transport properties in thin film FETs reveal an effect of film thickness on the in-plane hole mobility (transport direction parallel to the substrate) of RR-P3HT. In the film thickness range, from 20 nm to 200 nm, Gburek and co-authors reported an order of magnitude increase in the hole mobility; they attributed the trend to the improved ordering in thicker films.[26] However, using the same transistor structure, Reséndiz and collaborators reported only a slight decrease in the mobility within the same thickness range.[27]

With regard to the operation of solar cells, the out-of-plane hole mobility (transport direction normal to the substrate) is more relevant than the in-plane mobility, as the effective charge extraction occurs normal to the substrate in the bulk heterojunction device structure. The out-of-plane mobility is generally very different from in-plane mobility due to the anisotropy of crystalline RR-P3HT.[17] Typically, the out-of-plane hole mobility of highly regioregular P3HT is reported to be within the range of 10^{-4} to 10^{-3} $cm^2/V\text{-}s$, measured using the ToF measurement technique; no evidence of a film

thickness dependence has been reported.[13,21,28, 29] However, the ToF measurements were conducted on films in the thickness range of microns; the out-of-plane hole mobility has not been fully characterized in thinner RR-P3HT films, and indeed not less than 200nm in thickness. The effect of a substrate on the morphology of conjugated polymers is particularly important in thin films, in the thickness range of tens of nanometers. The out-of-plane carrier mobilities would be expected to be thickness dependent in this thickness regime. This issue has remained largely unexplored.

Here we report a study of the out-of-plane hole mobilities in RR-P3HT films of the same polymer, with thicknesses from 80 nm to over 1 μm, using the CELIV and ToF methods. Surprisingly the hole mobilities was lowest in the thinnest films, and increased by over an order of magnitude in film of thickness 700 nm; the mobilities remained constant for thicker films. We show that this behavior is connected to changes in the morphology, characterized using grazing incidence X-ray diffraction (GIXRD) and spectroscopic ellipsometry (SE), of the film, associated with effects of the underlying substrate.

2.2 EXPERIMENTAL SECTION

2.2.1 Materials

P3HT of high regioregularity was purchased from Rieke Metals, Inc. and used as received without further purification; it is of ~95% regioregularities and number average molecular weight 50,000 g/mol. The energy level aligning material poly(3,4-

ethylenedioxythiophene)-poly(styrenesulfonate) (PEDOT-PSS) (Clevios™ PH 500) was purchased from Heraeus Materials Technology and also used as received.

2.2.2 Experiments

2.2.2.1 Sample preparation

The samples were prepared using the following procedures. PEDOT:PSS solution was first warmed to room temperature and filtered by 0.45 μm nylon filters. A layer of PEDOT:PSS was spin-coated onto a pre-cleaned indium tin oxide (ITO)-coated glass substrate and then baked at 150 ˚C for 15 min in a nitrogen environment on a hot plate. Prior to spin coating of PEDOT:PSS, the ITO-coated glass substrates were solvent cleaned by consecutive ultrasonication in DI-water, acetone and isopropanol for 10 min each step, and then UV-cleaned for another 10 min.

The RR-P3HT was dissolved in chlorobenzene, shaken for over 10 hours and filtered with 0.45 μm Teflon filters. The solution concentrations were varied from 7 mg/ml to 52 mg/ml so that different film thicknesses could be spin coated, from the chlorobenzene solutions, onto the PEDOT:PSS/ITO substrates. These samples were then thermally annealed at 150 ˚C for 15 minutes. Subsequently, 2 nm thick layers of lithium fluoride were evaporated on top of these structures followed by evaporation of a layer of aluminum, serving as the top electrode, through shadow masks, at a typical pressure of 10^{-7} mbar. For the CELIV measurements the aluminum layer was 100 nm thick and for the ToF measurements the Al layers were 20 nm thick.

All solution spin-coating and thermal treatments were performed in a glovebox under nitrogen atmosphere (moisture<5 ppm, oxygen<5 ppm); the samples were transferred to the evaporation chamber without exposure to the atmosphere.

2.2.2.2 Hole mobility measurement

The ToF and CELIV experiments are well established techniques and carefully described in a number of publications,[30, 31] so we will describe information specific to our experiments. The ToF measurements were performed using a nitrogen laser (VSL337 from Newport) with a wavelength of λ=337 nm, an intensity per pulse of approximately 120 μJ, and a pulse width less than 4 ns, for photo-generation of charge carriers in the films. A Sorensen XHR300 DC power supply was used to apply constant voltage over devices. The current transients were then amplified using a FEMTO DLPCA-200 low noise current amplifier and recorded with a Tektronix TDS3052C digital oscilloscope.

For the CELIV measurements, a BK Precision 4075 function generator was used to apply the increasing voltage to the device to extract current transients. The current transients were then amplified using the FEMTO amplifier and recorded using the Tektronix digital oscilloscope. The ToF measurements were conducted in air while the CELIV measurements were conducted in a cryostat (VPF100 from Janis), which provided a vacuum of approximately 1 mTorr and a wide temperature range. Details of the experimental data and analysis are described later.

2.2.2.3 Structure characterization

The crystalline structure of the RR-P3HT thin film was investigated using Grazing Incidence X-ray Diffraction (GIXRD). Characterization was performed with a Rigaku Ultimate IV diffraction spectrometer (Rigaku, Tokyo, Japan) operating at 40 kV and 44 mA with CuKa radiation (λ = 1.5418 Å). Careful alignment of source and detector with respect to the sample was achieved by using a thin film attachment with three degrees of freedom. During the GIXRD measurements the incident angle was fixed at 0.5°, relative to the plane of sample surface. The scanning angle was measured every 0.02° at rate of 0.5° min^{-1} in the out-of-plane direction.

The thicknesses were measured using atomic force microscopy (AFM), and optical properties of RR-P3HT were measured using a variable angle spectroscopic ellipsometer, VASE, (M-2000, J.A. Woollam Co.). VASE measurements were performed in the transmission mode and the reflection mode at angles of 55°, 60°, 65°, 70° and 75°. The film thicknesses and complex refractive indices were measured by fitting the acquired ellipsometric angles Δ and Ψ to a Glass/PEDOT/Cauchy models using two different procedures in the CompleteEASE software (J.A. Woollam Co.). The first was accomplished by measuring films in both transmission mode and reflection mode (transmission weight of 300%),[32] and the second was done through use of multi-sample analysis (three samples of similar thickness, ±5%).[33] Samples of Glass/PEDOT were also measured to correctly determine the optical properties of PEDOT using a generalized oscillator model (GOM), which were observed to be similar to those found in the literature.[32] A glass/PEDOT/Cauchy model was used to fit to the thickness in the

transparent region of RR-P3HT, with incident energy less than 1.87 eV (λ>750 nm). This region was verified to be transparent by the transmission ellipsometry measurements. The optical constants for the entire measured spectrum (0.7 eV to 6.5 eV) were then determined by direct inversion of the ellipsometric equations. The resultant optical properties of the RR-P3HT layer were then parameterized to verify the values were physical and Kramers-Kronig (KK) consistent. The RR-P3HT layer was then confirmed to be anisotropic as has been shown in the literature.[32, 33] The degree of anisotropy was determined by the difference between refractive indices in the ordinary and extra-ordinary directions, i.e., the in-plane and out-of-plane directions respectively[33]

$$\Delta n = n_o - n_e \tag{2.1}$$

For our study the degree of anisotropy was evaluated at an incident energy of 1.00 eV (λ~1240 nm), well in the transparent region of RR-P3HT. Nevertheless, please note that any wavelength in the transparent region exhibits the same trends.

2.3 RESULTS AND DISCUSSION

The out-of-plane hole mobilities in RR-P3HT films with thicknesses ranging from 80 nm to 1.5 μm were measured by the CELIV method. Unlike ToF, the CELIV method requires no injection or photo-excitation of charge carriers, so the problem of internal electric field perturbations is avoided. This problem restricts the application of ToF to relatively thick films; the CELIV technique is more appropriate for thinner films.[30]

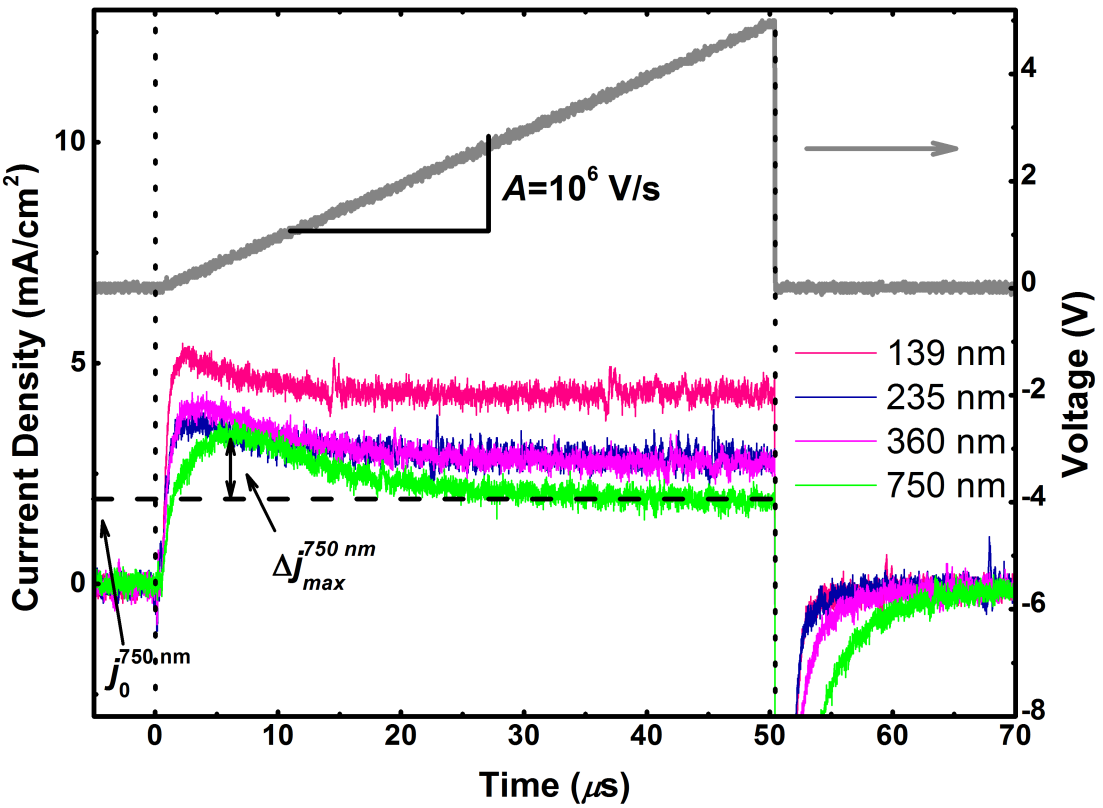

Figure 2.3 Raw data of CELIV measurements of RR-P3HT films with different thicknesses. The upper curve represents the voltage of a ramping rate of $\boldsymbol{A}$ = 1×10^6 Vs^{-1}. *The four lower curves are the current transients extracted from RR-P3HT films.* $\boldsymbol{j_0}$ *and* $\boldsymbol{\Delta j_{max}}$ *for 750 nm film are identified by arrows.*

Plotted in Figure 2.3 are the results from the CELIV measurements of RR-P3HT films; the current density is plotted as a function of time for four different film thicknesses. The upper curve represents the voltage applied to each sample at room temperature; it ramps up at the rate of $\boldsymbol{A}$ = 1×10^6 Vs^{-1}. Current transients, exhibited by each film, exhibit maxima during the early stages of the application of the fields. The CELIV model developed to interpret the data assumes that the diffusion current is negligible, so the current transients are composed of two components: the displacement current and the drift current.[30] The displacement current $\boldsymbol{j_0}$ is caused by the geometric capacitance of the sample and becomes smaller as the film thickness increases. The drift current, $\boldsymbol{\Delta j_{max}}$,

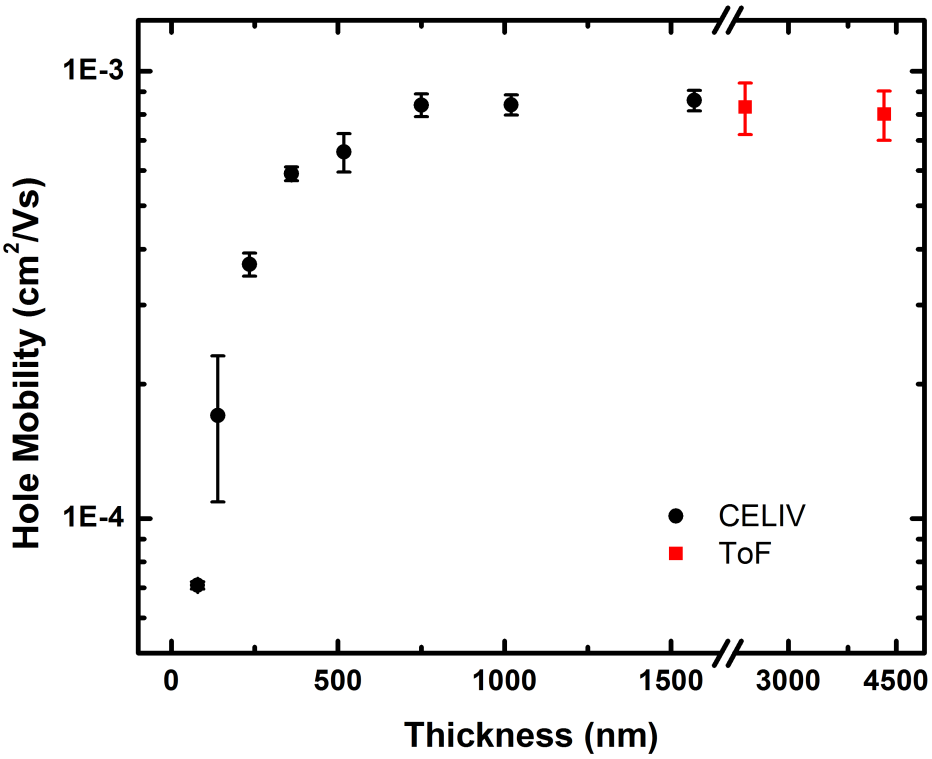

Figure 2.4 Thickness dependence of hole mobilities measured by both CELIV (black) and ToF (red) methods displayed on a semi-log scale.

represents the charges extracted from the film and becomes larger in thicker films because more charges are extracted. The values of the drift and displacement currents in the 750 nm thick film are identified by the arrows in Figure 2.3. The time at which the total current transient reaches maximum, t_{max}, is measured from the drift current, and is used to calculate the hole mobility μ:[30]

$$\mu = \frac{2d^2}{3At_{\max}^2\left(1+0.36\frac{\Delta j_{\max}}{j_0}\right)} \tag{2.2}$$

where d is the film thickness, A is the voltage ramping rate, $\Delta j_{max} = j(t_{max}) - j_0$, and $j_0 = A\varepsilon\varepsilon_0/d$.

The out-of-plane hole mobilities obtained from the CELIV measurements for seven different RR-P3HT thin films are plotted in Figure 2.4 (black circles). The mobility increases monotonically from 7.1×10^{-5} $cm^2V^{-1}s^{-1}$ to 8.6×10^{-4} $cm^2V^{-1}s^{-1}$ as the thickness is increased from 80 nm to 700 nm and reaches a plateau for thicknesses beyond 700 nm. This thickness dependence, to the best of our knowledge, has not been previously reported. It would not have been measured using ToF because ToF measurements are usually conducted on films with thicknesses typically greater than approximately one micron. Our data reveal that for thicknesses greater than 700 nm, the mobility saturates at a value of $\boldsymbol{\mu}$ = 8.6×10^{-4} $cm^2V^{-1}s^{-1}$. This value is in excellent agreement with those measured using ToF (red squares in Figure 2.4) for thicker films in the range of 2 to 5 μm. Before providing an explanation for this thickness dependence in terms of the morphology of the film, we will first discuss the field dependence of the mobilities to show that they are consistent with theory that describes transport in disordered conductors.

The hole mobility in RR-P3HT films is influenced by the external electric field. In the case of the CELIV measurements, the applied voltage is increased linearly throughout the measurement, so the electric field is not constant. The electric field of interest in our experiments is extracted at the time when the current reaches its maximum value; this specific time is the time used to calculate the carrier mobility. We examined a range of film thicknesses; each film in our study was subjected to different voltage ramping rates. Each transient current maximum value is associated with a ramping rate and a certain electric field. The field dependencies of hole mobilities are plotted in Figure 2.5. For any

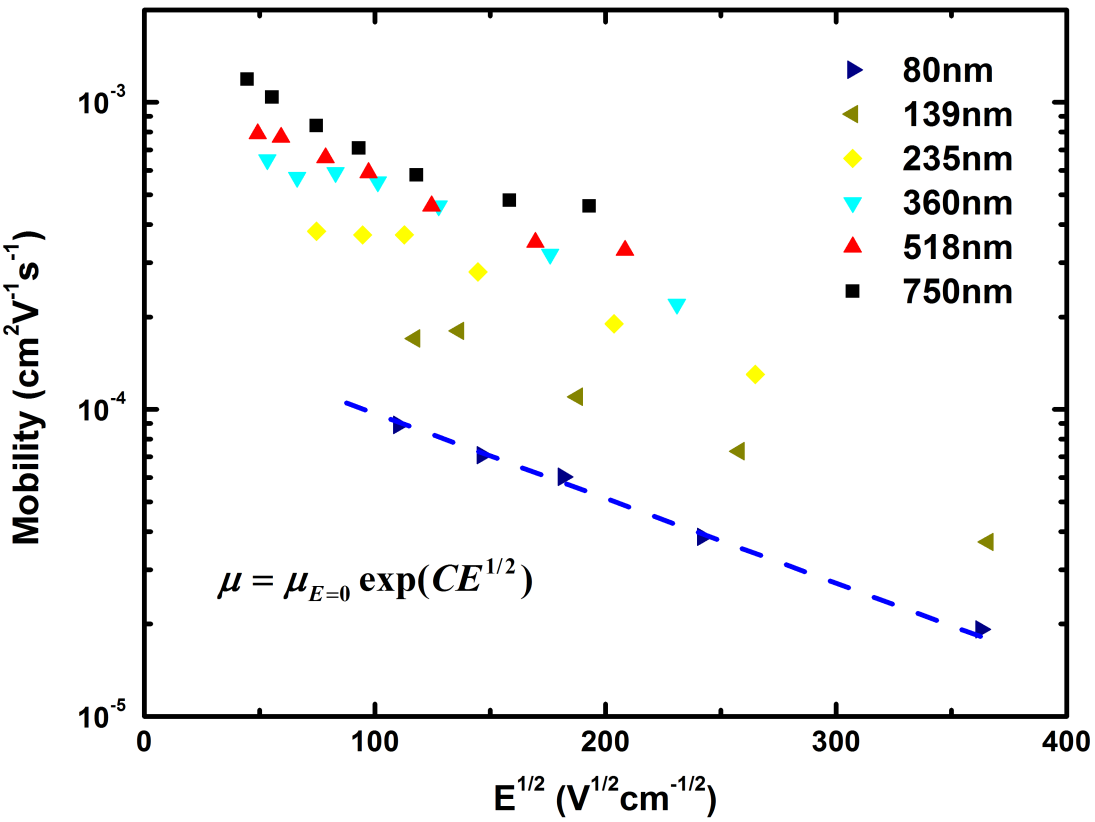

Figure 2.5 Electric field dependence of out-of-plane hole mobilities in RR-P3HT thin films of increasing thicknesses. The dashed line shows a good agreement between the experimental results and the Poole-Frenkel relationship.

specific electric field, the enhancement is almost one order of magnitude larger for the 750 nm film, compared to the 80 nm thick samples, as shown in Figure 2.4. For the 750 nm film, the hole mobilities are in excellent agreement with the results obtained using the ToF technique throughout the entire electric field region.[31]

For each thickness, the electric field dependence of hole mobility is in agreement with the Poole-Frenkel relationship (indicated by the blue dashed line in Figure 2.5):[28]

$$\mu = \mu_{E=0} \exp(CE^{1/2}) \quad (2.3)$$

even for electric fields as low as $\boldsymbol{E}$ = 2.5×10^5 Vm^{-1} ($\boldsymbol{E^{1/2}}$ = 50 V$^{1/2}$cm$^{-1/2}$). In this equation $\boldsymbol{\mu_{E=0}}$ is the mobility extrapolated to zero electric field and $\boldsymbol{C}$ is a coefficient. The Poole-

Frenkel theory describes the electric-field-assisted thermal motion of charge carriers between localized states in a semiconductor. With increasing electric field, the charge carriers require less thermal energy for delocalization and the mobility increases. This trend has been observed in low molecular weight P3HT thin films before.[34] However, we used high molecular weight P3HT. The data in Figure 2.5 show that $\boldsymbol{C} < 0$ for all film thicknesses, indicating the mobility decreases with increasing electric field. Such a decrease of the mobility with increasing electric field has been widely reported for high molecular weight RR-P3HT films in this electric field range and for other disordered conductors.[31, 35-38] Carrier transport in disordered conductors is influenced by the statistical distribution of energy states and by the spatial distribution of sites (structural disorder) into which the carriers hop. In an environment of significant structural disorder, the effect of the spatial structural disorder is to oppose the long-range transport of the carriers. If structural disorder have the dominant influence on transport, then $\boldsymbol{C} < 0$ and the mobility decreases with increasing electric field.

Specifically with regard to RR-P3HT, the hole mobility along the π-π coupling direction is two orders of magnitude faster than in the transverse direction.[17] Because the RR-P3HT film is composed of crystal domains with different orientations, associated with a distribution of π-π coupling directions, the hole mobility is influenced by the morphology. So macroscopic carrier transport in RR-P3HT in the presence of a sufficiently large E-field would be impeded by the inherent structure of the material, thereby leading to the decreasing mobility with increasing electric field (i.e.: $\boldsymbol{C} < 0$).

The film thickness dependence of the mobility of RR-P3HT may be reconciled in terms of the structure of RR-P3HT thin films. In thin RR-P3HT films, P3HT tends to form a layer of surface induced edge-on crystalline phase on PEDOT:PSS-coated ITO substrate, as shown previously in the literature.[39] Hence, the out-of-plane direction has the lowest π-π coupling direction and the hole mobility is comparatively low; recall that the hole mobility along the π-π coupling direction is two orders of magnitude faster. However, as the film thickness increases, the substrate-induce-orientation effect decreases and a larger fraction of the structure of the film will possess other orientations. So the effective π-π coupling along the out-of-plane direction is enhanced and therefore the hole mobility would be expected to increase. Beyond a threshold thickness, the distribution of orientations of crystal domains in the RR-P3HT films becomes completely random. Consequently, the mobility should reach a constant value beyond a threshold thickness.

Structural information, gleaned from grazing incidence x-ray diffraction (GIXRD) and ellipsometry, provides more insight into the issue. GIXRD, with the scattering vector in the out-of-plane direction, was performed to characterize the structure of the films. The data in Figure 2.6 show the average grain sizes, calculated from the full widths at half maximum (FWHMs) of the (100) peaks in the profiles (shown in the inset), increased from 10.9 nm to 12.7 nm; beyond which it remains constant with increasing film thickness. This increase in grain size is in part responsible for the enhancement of the hole mobility; with a larger grain size, the carriers experience fewer crystalline/amorphous/crystalline boundaries to transport as they traverse the film. Carrier mobilities in the amorphous regions are appreciably lower than in the crystalline regions.

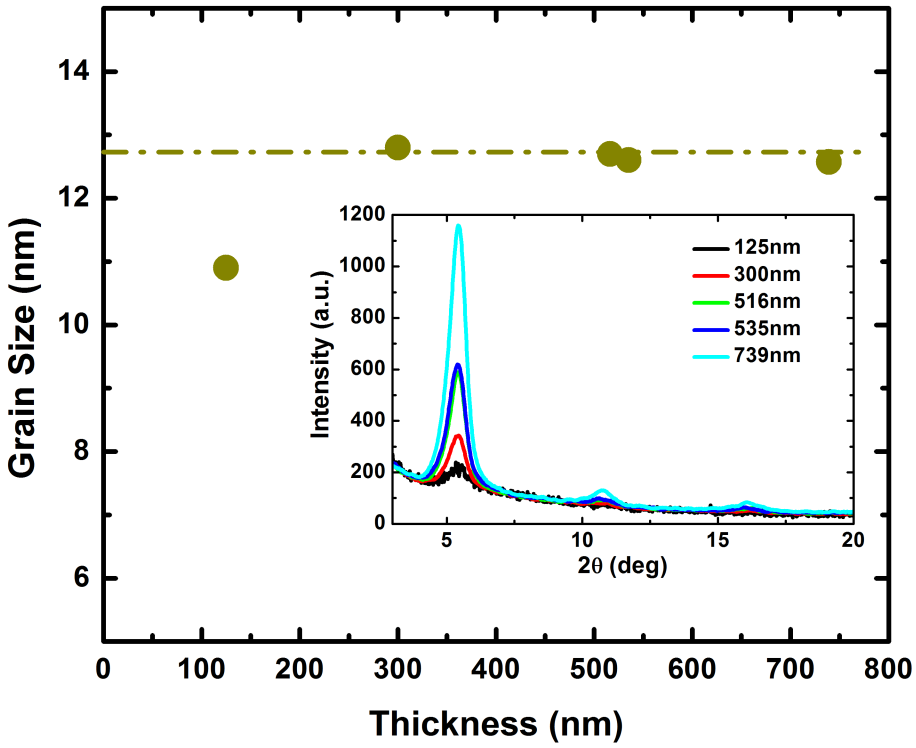

Figure 2.6 Thickness dependence of grain size in RR-P3HT films. The inset shows raw XRD profiles from which the grain sizes are calculated. The dash-dot lines indicate where the values saturate.

It is important to note, however, that the grain sizes become constant at thicknesses just less than 300 nm, whereas the carrier mobilities become constant in films that are much thicker, greater than 700 nm. For films thicker than 300nm, the XRD profiles show no significant change with regard to crystal orientations. The appearance of strong (100) peaks reveals the existence of a significant amount of edge-on crystalline phases in each film. Nevertheless, this cannot exclude the possible existence of face-on crystalline phase because the characteristic (020) peak of face-on phase is centered at $2\theta \approx 21.6^{\circ}$,[17] which is beyond our current measurement range.

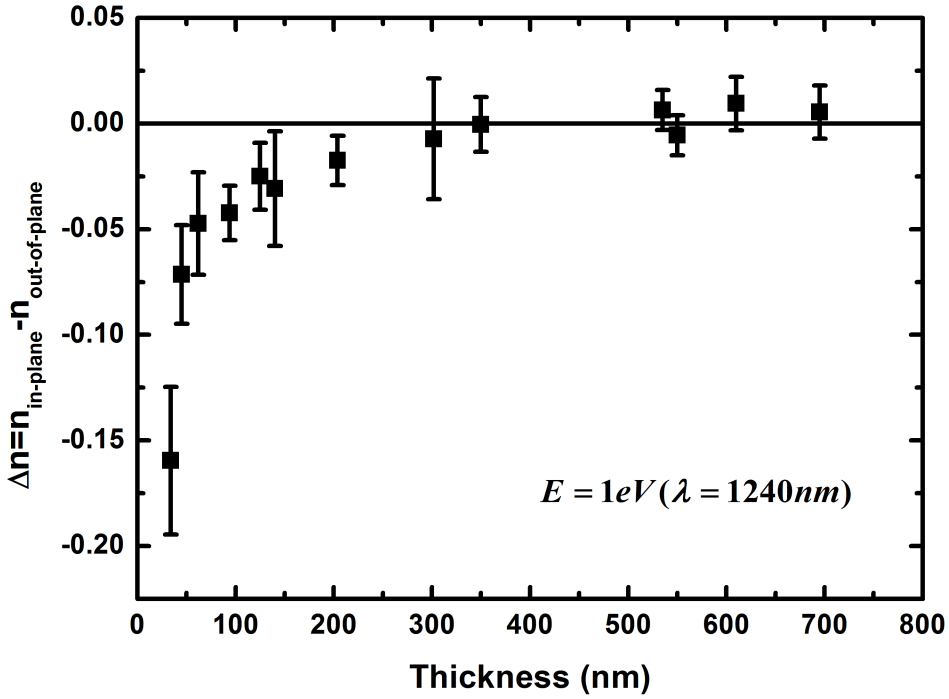

Figure 2.7 Difference between the in-plane and out-of-plane refractive indices against the film thickness. The dash-dot line shows the zero anisotropy level.

However we show below that a comparable fraction of face-on phases exist in all these films. The different orientations of the edge-on and face-on phases contributes to optical anisotropy of the film.[33] The degree of optical anisotropy of the films was investigated using VASE. Refractive indices in the ordinary and extra-ordinary directions, which are the in-plane and out-of-plane directions respectively, were determined by fitting the ellipsometric data through a careful procedure previously described by Ng and Campoy-Quiles.[32,33] The degree of anisotropy is then determined from the difference of these two indices, as shown in Figure 2.7, as a function of film thickness. In thin films, the out-of-plane refractive index is larger than the in-plane refractive index, indicating an anisotropic film structure. This is due to the effect of the substrate-induced orientation of

edge-on crystals.[39] As the film thickness increases, the difference diminishes and sufficiently far from the interfaces the two indices become comparable. This implies that the film structure gradually changes from a highly anisotropic state to a totally isotropic state. Since we have already confirmed the existence of edge-on crystalline phase from the GIXRD, such isotropy indicates that a comparable amount of face-on crystalline phase must also exist in the films, which is favorable to the out-of-plane mobility. Interestingly, the isotropic state begins to develop at about 300 nm from the substrate. This is consistent with the thickness at which grain size becomes constant. We note, however, that this thickness is less than the thickness of 700 nm, beyond which the hole mobilities become constant.

In order to reconcile the difference between these two thresholds, a simple simulation of the thickness dependence of optical and electric transport properties is carried out on a thin film structure. The film is modeled as a three-dimensional lattice of cubes, with 100×100 cubes in the xy-plane parallel to the substrate, and the number of layers of cubes in *z*-direction represents the film thickness. Each cube is treated as a crystal domain, which has defined specific optical and electric transport properties related to its orientation with respect to the substrate, indexed from 1 to 10. A value of 1 denotes a completely edge-on configuration, which has the highest resistivity in the out-of-plane direction; a value of 10 denotes a purely face-on configuration, which has the lowest resistivity. The other values denote intermediate cases. The highest resistivity is assumed to be 100 times larger than the lowest one; see supporting information for more details. To illustrate the substrate effect on crystalline orientations, we created the film such that

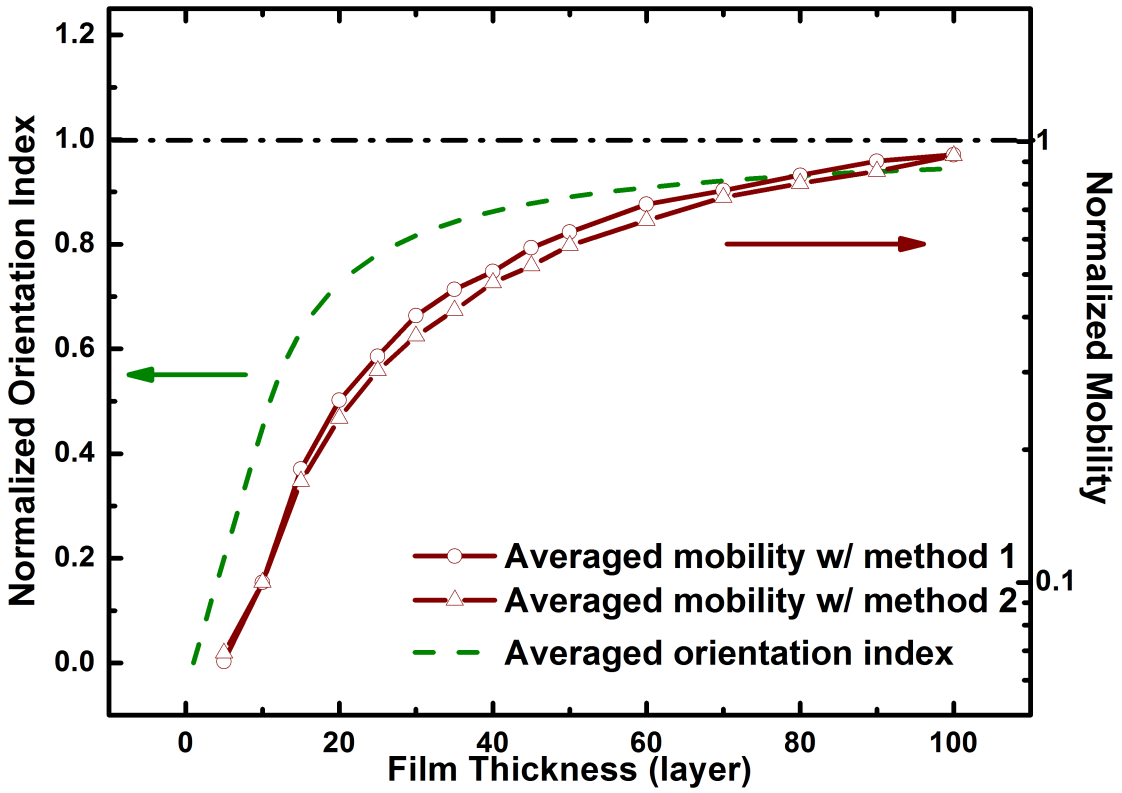

Figure 2.8 Simulated results of optical property, which is represented by orientation index, and transport property, which is represented by effective mobility. The dash-dot line indicates where the properties saturate. Methods 1 and 2 are discussed in detail in the supporting information.

the first layer is composed of a purely edge-on configuration, identified as Cube 1. The second layer is composed of 90% Cube 1 and 10% randomly assigned cubes. For the third layer: 80% Cube 1 and 20% randomly chosen cubes. The subsequent layers are described accordingly; at the 11^{th} layer the structure is completely random. Our system is defined such that the fraction of Cube 1 in the entire film would gradually saturate at 10%.

The anisotropy, represented by the orientation index, is calculated by the arithmetic mean of indices of all cubes for film thickness, in analogy to how ellipsometry averages the optical properties of a film. As for the electric transport property, a charge carrier follows a random walk from the first layer to the last through a path determined

by a probabilistic criterion (please refer to supporting information for details). The value resistivities of all cubes in this path are then averaged to generate the conductivity, which can be scaled to a mobility value. For each thickness, 1000 runs are performed and the final mobility was averaged over the 1000 values. Both the anisotropy and mobility data were normalized to (0,1] range and shown in the Figure 2.8. As the film thickness increases, the normalized orientation index approaches from 0 (completely edge-on, anisotropy) to 1 (completely random, isotropy), which qualitatively reflect the change of film from anisotropic to isotropic, as shown by the ellipsometry data. Likewise, the mobility increases along with the thickness and saturates at certain value, which is also consistent with the measured mobility values. Both saturations result from the introduction of additional cubes of random orientations in higher order layers. This reflects the reality that the effect of substrate on the formation of edge-on phase is diminished with distance away from the substrate. However, the simulated optical property converges at a much thinner thickness than the simulated electric transport property, which indicate that isotropy and grain size saturates at a thinner film thickness than out-of-plane hole mobility. We would like to point out here that despite the fact that the results are based on a film of 10% gradient per layer, the observed saturations of optical and electrical properties and the existence of the difference between the thresholds of two saturations are universal for any gradient film structure which is induced by the substrate effect (results from films with other gradients are in the supporting information).

As it was previously described, the changes and saturations of both anisotropy and out-of-plane mobility are caused by the substrate-induced gradient in film structure. When the thickness of the film is small, 100nm, this effect is more pronounced. Therefore the electronic properties of the bulk do not necessarily represent the properties of the material used in devices of thicknesses around 100nm. On the other hand, the discrepancy between two saturation thresholds in the simulation essentially comes from the different ways of averaging the optical and electric transport properties. Since the experimentally measured anisotropy, grain size and mobility are also averaged values; such consistency between the simulated and the experimental results suggests that there is also an inherent difference between the averaging methods of structural characterization and that of mobility characterization. In other words, while the average film structure does not change significantly, the average electric transport property, generally, does. This is important toward understanding the connection between the transport property and the structure: characterization of macroscopic structure may not be enough to predict the behavior of the macroscopic transport properties. Transport properties are generally influenced by microscopic structures like pathways.

2.4 CONCLUSIONS

In this paper, we studied the thickness dependence of the out-of-plane hole mobility in RR-P3HT thin films ranging in thickness from 80 nm to over 1 μm. The mobility monotonically increased by an order of magnitude as the thickness increased

and reached a value of approximately 1×10^{-3} $cm^2/V\cdot s$ for thicknesses greater than 700 nm. The implication here is that the carrier mobilities are not constant in this material. At the substrate the orientation of the molecules is edge-on, and with increasing distance from the substrate the fraction of face-on orientations increase. The out-of-plane hole mobilities in the edge-on direction are orders of magnitude slower than in the face-on orientations. Such structural changes are due to the substrate effect, as shown by the ellipsometric measurements of anisotropy and simulations. The increase of the hole mobilities is qualitatively understood from the fact that as film thickness increases, the structural anisotropy of the film decreases, due to the increase in the fraction of different orientations that favor more rapid out-of-plan carrier transport. Measurements that reflect structural evolution reveal that for film thicknesses greater than 300nm, the average grain size and anisotropy remains constant. However, the hole mobility continues to increase for films as thick as 700nm. This difference between the threshold values associated structural and electric transport properties is likely associated with the fact that the transport properties are influenced not only macroscopic morphology but also by microscopic pathways, which are often tortuous.

2.5 SUPPORTING INFORMATION

The film was modeled as a three dimensional lattice of cubes of equal size, representing the various grains. Each *xy*-plane, which is parallel to the substrate, consisted of 100 × 100 cubes and the number of *xy*-planes in *z*-direction was varied depending on

the thickness of the film of interest. Each cube was assigned certain orientation with a corresponding resistivity. The orientation was indexed from 1 to 10 (1 being completely edge-on with the highest resistivity and 10 being completely face-on with the lowest). The resistivity for each cube is calculated using two methods:

$$\begin{cases} \textbf{Method 1: } R_i = \dfrac{1}{i^2} (i = 1, 2, \cdots, 10); \\ \textbf{Method 2: } R_i = \dfrac{R_1 R_{10}}{\sqrt{(R_1 \sin\theta_i)^2 + (R_{10} \cos\theta_i)^2}}, \\ R_1 = 1, R_{10} = 0.01, \theta_i = \dfrac{i-1}{9}\dfrac{\pi}{2} (i = 1, 2, \cdots, 10) \end{cases} \tag{2.4}$$

For each method, R_1 = 1 (edge-on) and R_{10} = 0.01 (face-on), based on the fact that the hole mobility in the π-π coupling direction is 100 times large of that in the non-coupling direction.[17] The difference between the two methods lies in how the intermediate resistivities are distributed. Method 1 assumes that the conductivity of each cube is a square number; Method 2 makes use of an elliptical analogy, with R_1 and R_{10} being the semi-major and the semi-minor axes, respectively. Each intermediate resistance is the radius of ellipse at a given angle from the semi-major axis, in which the angles were linearly divided.

In order to mimic a real film in which the substrate induces orientation, the model incorporates a substrate-induced enrichment of the highest-resistivity domain (Cube 1, face-on). In our film we assumed a gradient in orientation, in which the first layer contained only edge-on crystals (Cube 1), 90% edge-on and 10% randomly chosen orientations in the second layer, 80% edge-on and 20% randomly chosen orientations in the third layer, and so on until it is completely random starting from the 11th layer. As the

film gets thicker (the number of layers goes to infinite), structurally it would be more and more bulk-like, and the fraction of edge-on crystals (Cube 1) in the entire film would gradually saturate at 10%.

As the cube numbers is equivalent to the crystal orientation of the grain, the average of all the cube numbers gives an estimate of the average orientation of the crystal domains throughout the film. Because ellipsometry also yields the average orientation of the crystals through measuring the anisotropy, the results are comparable. The optical property is thus averaged by the arithmetic mean of numbers of all cubes and is normalized to (0,1] scale.

To determine the path along which a charge carrier would travel through the film from the first layer to the last, we set up the following protocol. The charge carrier can only go to the adjacent cubes, except the one in the previous layer (5 possible directions in total); the probability of going in each direction is proportional to the number of each cube. In other words, given the numbers of the 5 adjacent cubes a_1, a_2, a_3, a_4 and a_5 (a_1, ..., a_5 = 1, 2, ..., 10), the probability that the charge carrier takes the direction of a_i is determined by

$$P(a_i) = \frac{a_i}{\sum_{k=1}^{5} a_k} \tag{2.5}$$

As the path of the charge carriers is determined using probabilities, even starting from the same location the carrier may travel along different paths for multiple runs of the procedure (a 2D case is shown in Figure 2.9). In practice, we randomly select a position in the first layer and record the path of the charge carrier. By averaging 1,000

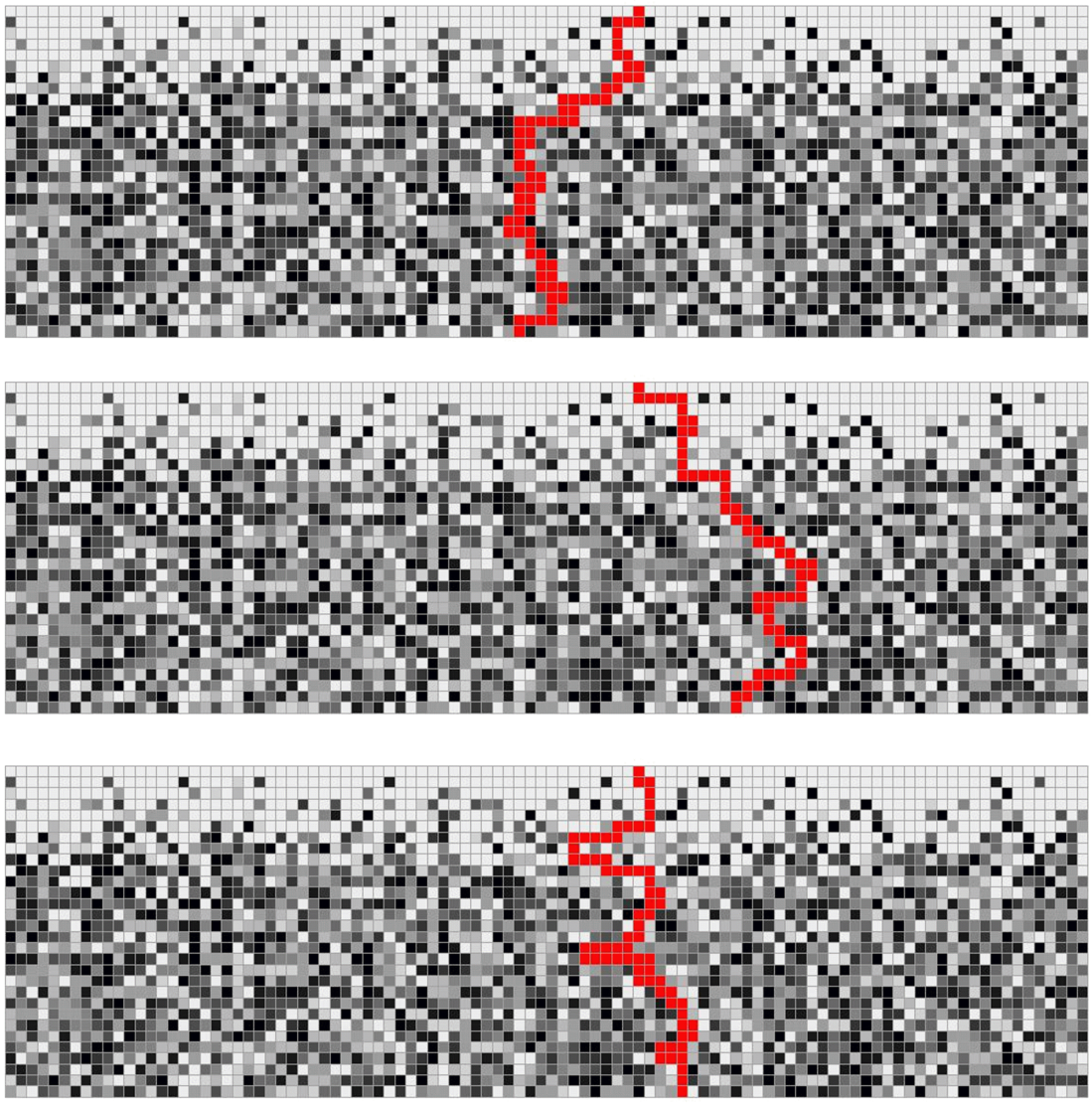

Figure 2.9 Three examples of random walk that a charge carrier takes from the same starting spot in the first layer to the last layer. The grayscale represents the index of each cube. The first layer is composed of only Cube1 and 10% gradient is applied to the first ten layers. It is obvious that in the same film structure, a charge carrier does take different routes through the film based on the same path protocol.

runs of the same procedure, we obtain the macroscopic electrical properties of the film: the resistivity and the conductivity of the entire film. Since only one charge carrier follows a random walk in each run, the effect of the interaction between electrons on the transport property is eliminated. So the charge carrier density does not play a role and

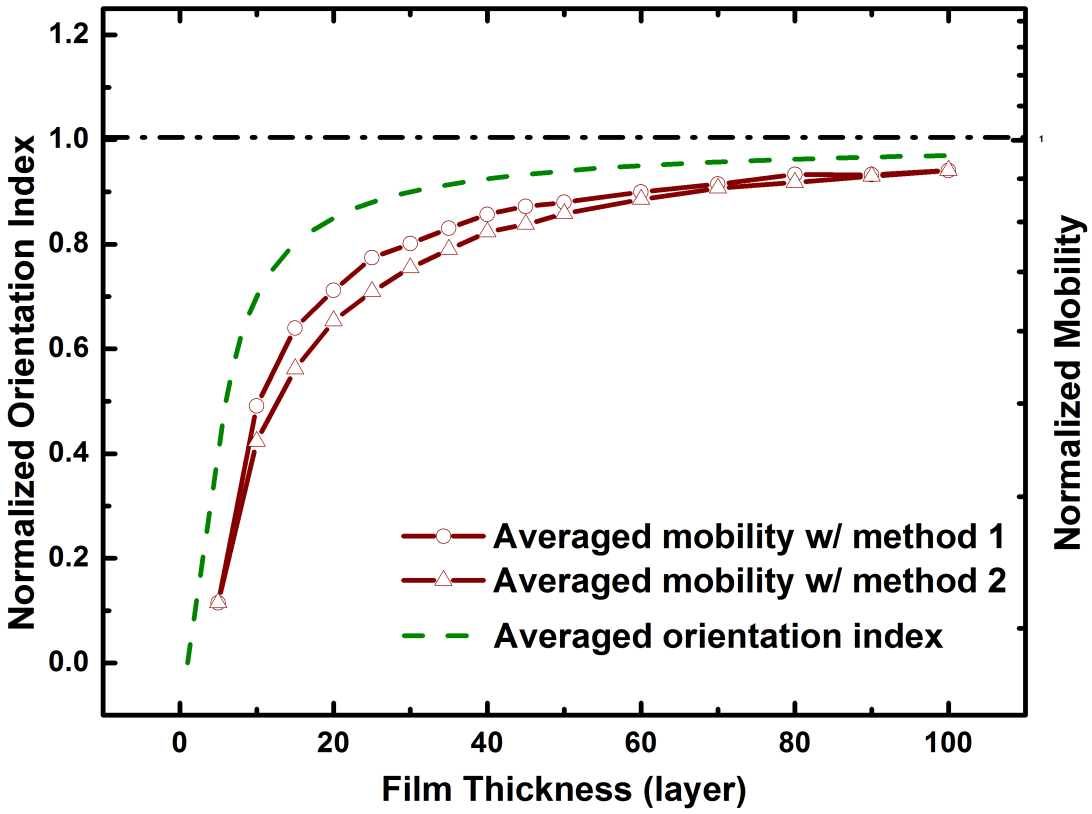

Figure 2.10 Simulated results of optical property and transport property from a 20% gradient film structure. The dash-dot line indicates where the properties saturate.

the calculated conductivity is essentially the mobility scaled by some constant. The mobility calculated with the two methods are then normalized to the same (0,1] scale.

Final results for the thickness dependence of both orientation index and effective mobility based on the film structure of a 10% gradient are shown in the main text of the paper. But the observation of saturations of both properties and the difference between the two saturation thresholds are universal to other gradient film structures. This is demonstrated by another set of simulated data based on a 20% gradient as shown in Figure 2.10.

2.6 REFERENCES

1. Facchetti, A. *Materials Today* **2007,** 10, (3), 28-37.
2. Kulkarni, A. P.; Tonzola, C. J.; Babel, A.; Jenekhe, S. A. *Chemistry of Materials* **2004,** 16, (23), 4556-4573.
3. Guenes, S.; Neugebauer, H.; Sariciftci, N. S. *Chemical Reviews* **2007,** 107, (4), 1324-1338.
4. Kroon, R.; Lenes, M.; Hummelen, J. C.; Blom, P. W. M.; de Boer, B. *Polymer Reviews* **2008,** 48, (3), 531 - 582.
5. Hoth, C. N.; Schilinsky, P.; Choulis, S. A.; Brabec, C. J. *Nano Letters* **2008,** 8, (9), 2806-2813.
6. Giebink, N. C.; Forrest, S. R. *Physical Review B* **2008,** 77, (23), 235215.
7. Newman, C. R.; Frisbie, C. D.; da Silva Filho, D. A.; Brédas, J.-L.; Ewbank, P. C.; Mann, K. R. *Chemistry of Materials* **2004,** 16, (23), 4436-4451.
8. Schilinsky, P.; Waldauf, C.; Hauch, J.; Brabec, C. J. *Journal of Applied Physics* **2004,** 95, (5), 2816-2819.
9. Scharber, M. C.; Mühlbacher, D.; Koppe, M.; Denk, P.; Waldauf, C.; Heeger, A. J.; Brabec, C. J. *Advanced Materials* **2006,** 18, (6), 789-794.
10. Lebedev, E.; Dittrich, T.; Petrova-Koch, V.; Karg, S.; Brutting, W. *Applied Physics Letters* **1997,** 71, (18), 2686-2688.
11. Hertel, D.; Bassler, H.; Scherf, U.; Horhold, H. H. *The Journal of Chemical Physics* **1999,** 110, (18), 9214-9222.
12. Martens, H. C. F.; Blom, P. W. M.; Schoo, H. F. M. *Physical Review B* **2000,** 61, (11), 7489-7493.
13. Choulis, S. A.; Kim, Y.; Nelson, J.; Bradley, D. D. C.; Giles, M.; Shkunov, M.; McCulloch, I. *Applied Physics Letters* **2004,** 85, (17), 3890-3892.
14. Hotta, S.; Soga, M.; Sonoda, N. *Synthetic Metals* **1988,** 26, (3), 267-279.
15. Chen, T.-A.; Wu, X.; Rieke, R. D. *Journal of the American Chemical Society* **1995,** 117, (1), 233-244.
16. McCullough, R. D.; Lowe, R. D.; Jayaraman, M.; Anderson, D. L. *The Journal of Organic Chemistry* **1993,** 58, (4), 904-912.
17. Sirringhaus, H.; Brown, P. J.; Friend, R. H.; Nielsen, M. M.; Bechgaard, K.; Langeveld-Voss, B. M. W.; Spiering, A. J. H.; Janssen, R. A. J.; Meijer, E. W.; Herwig, P.; de Leeuw, D. M. *Nature* **1999,** 401, (6754), 685-688.
18. Sirringhaus, H.; Tessler, N.; Friend, R. H., Integrated Optoelectronic Devices Based on Conjugated Polymers. In 1998; Vol. 280, pp 1741-1744.
19. Padinger, F.; Rittberger, R. S.; Sariciftci, N. S. *Advanced Functional Materials* **2003,** 13, (1), 85-88.
20. Bao, Z.; Dodabalapur, A.; Lovinger, A. J. *Applied Physics Letters* **1996,** 69, (26), 4108-4110.
21. Ballantyne, A. M.; Chen, L.; Dane, J.; Hammant, T.; Braun, F. M.; Heeney, M.; Duffy, W.; McCulloch, I.; Bradley, D. D. C.; Nelson, J. *Advanced Functional Materials* **2008,** 18, (16), 2373-2380.

22. Zhang, R.; Li, B.; Iovu, M. C.; Jeffries-El, M.; Sauvé, G.; Cooper, J.; Jia, S.; Tristram-Nagle, S.; Smilgies, D. M.; Lambeth, D. N.; McCullough, R. D.; Kowalewski, T. *Journal of the American Chemical Society* **2006,** 128, (11), 3480-3481.
23. Xiao, X.; Wang, Z.; Hu, Z.; He, T. *The Journal of Physical Chemistry B* **2010,** 114, (22), 7452-7460.
24. Sandberg, H. G. O.; Frey, G. L.; Shkunov, M. N.; Sirringhaus, H.; Friend, R. H.; Nielsen, M. M.; Kumpf, C. *Langmuir* **2002,** 18, (26), 10176-10182.
25. Wang, G. *J. Appl. Phys.* **2003,** 93, (10), 6137.
26. Gburek, B.; Wagner, V. *Organic Electronics* **2010,** 11, (5), 814-819.
27. Reséndiz, L.; Estrada, M.; Cerdeira, A.; Iñiguez, B.; Deen, M. J. *Organic Electronics* **2010,** 11, (12), 1920-1927.
28. Ballantyne, A. M.; Wilson, J. S.; Nelson, J.; Bradley, D. D. C.; Durrant, J. R.; Heeney, M.; Duffy, W.; McCulloch, I. In *TOF mobility measurements in pristine films of P3HT: control of hole injection and influence of film thickness*, Organic Photovoltaics VII, San Diego, CA, USA, 2006; SPIE: San Diego, CA, USA, 2006; pp 633408-11.
29. Malhotra, B. D.; Takashima, W.; Pandey, S. S.; Singhal, R.; Endo, K.; Rikukawa, M.; Kaneto, K. *Japanese Journal of Applied Physics Part 1-Regular Papers Short Notes & Review Papers* **1999,** 38, (12A), 6768-6771.
30. Genevicius, K.; Österbacka, R.; Juska, G.; Arlauskas, K.; Stubb, H. *Thin Solid Films* **2002,** 403-404, 415-418.
31. Kaneto, K.; Hatae, K.; Nagamatsu, S.; Takashima, W.; Pandey, S. S.; Endo, K.; Rikukawa, M. *Jpn. J. Appl. Phys. Part 2 - Lett.* **1999,** 38, (10B), L1188-L1190.
32. Ng, A.; Li, C. H.; Fung, M. K.; Djuris ̆ic ́, A. B.; Zapien, J. A.; Chan, W. K.; Cheung, K. Y.; Wong, W.-Y. *The Journal of Physical Chemistry C* **2010,** 114, (35), 15094-15101.
33. Campoy-Quiles, M.; Etchegoin, P. G.; Bradley, D. D. C. *Physical Review B* **2005,** 72, (4), 045209.
34. Goh, C.; Kline, R. J.; McGehee, M. D.; Kadnikova, E. N.; Frechet, J. M. J. *Applied Physics Letters* **2005,** 86, (12), 122110-3.
35. Takashima, W.; Pandey, S. S.; Endo, T.; Rikukawa, M.; Tanigaki, N.; Yoshida, Y.; Yase, K.; Kaneto, K. *Thin Solid Films* **2001,** 393, (1-2), 334-342.
36. Mozer, A. J.; Sariciftci, N. S. *Chemical Physics Letters* **2004,** 389, (4-6), 438-442.
37. Borsenberger, P. M. *Journal of Applied Physics* **1990,** 68, (11), 5682-5686.
38. Van der Auweraer, M.; De Schryver, F. C.; Borsenberger, P. M.; Bässler, H. *Advanced Materials* **1994,** 6, (3), 199-213.
39. Kim, J. S.; Park, Y.; Lee, D. Y.; Lee, J. H.; Park, J. H.; Kim, J. K.; Cho, K. *Advanced Functional Materials* **2010,** 20, (4), 540-545.

CHAPTER 3
ROLE OF DOMAIN SIZE AND PHASE PURITY ON CHARGE TRANSPORT IN BULK HETEROJUNCTION SOLAR CELLS

3.1 INTRODUCTION

Bulk heterojunction (BHJ) organic solar cells are promising alternatives to inorganic solar cells for certain applications because they are easily fabricated at relatively low cost using solution based methods that include spincoating and jet printing;[1, 2] their adaptability to flexible substrates makes them viable for large scale applications using roll-to-roll processing methods.[3] In BHJ organic solar cells, the active layer is composed of a conjugated polymer, which typically serves the role of the donor material (D), and a fullerene derivative as the acceptor component (A). Single BHJ devices have achieved power conversion efficiencies (***PCE***s) in the range of 7-9%.[4, 5]

The effect of the BHJ structure on device performance has been extensively studied.[6, 7] The active morphology generally consists of the acceptor-rich, donor-rich phases, and the intermixed phase, interfacial region, between them.[8] Generally the

dissociation of excitons into free carriers occurs in the mixed D:A phases in the interfacial region, where excitons would subsequently undergo charge separation. Phase separation between the D and A phases is such that pathways are created for photocarriers to be transported through the D or A phases of the active layer to the electrodes, where they are collected.[9, 10] A large interfacial region between the D and A rich phases would increase the photocarrier generation, and therefore the short circuit current ($\boldsymbol{J_{SC}}$), provided that recombination is low.[11-13] It is also known that recombination could take place at the interfacial region, so the structure within the interfacial region is important. It follows that the D-rich and A-rich domain sizes and phase purities are also important factors that influence the overall device efficiency. For example, large D and A domain sizes would generally be associated with a smaller interfacial region. Hence the carrier density and $\boldsymbol{J_{SC}}$ would be reduced correspondingly, as the probability of exciton dissociation would decrease. With regard to the phase purity/crystallinity, highly crystalline conjugated polymer phases enable high hole mobility, which is beneficial for device performance.[14] The purity and crystallinity of the polymer-rich phase may be disrupted due to the diffusion and mixing of the acceptor molecules, which would exacerbate the effects of recombination and consequently affects device parameters.[15] Clearly, the device performance is critically dependent on the morphology of the BHJ; the magnitudes of the $\boldsymbol{J_{SC}}$, the fill factor ($\boldsymbol{FF}$) and the open circuit voltage ($\boldsymbol{V_{OC}}$) will vary based on changes in the morphology of the active layer.

Recent simulations suggest that the phase purity and the structure of the D:A interfacial region could be of greater importance than the domain size toward

determining the exciton dissociation and carrier collection process and consequently the $\boldsymbol{J_{SC}}$.[16, 17] Specifically, they showed that a well-connected network of domains of width 4 nm, with high domain purity and narrow D:A interfacial region, outperformed the morphology with diffuse interfacial region and impure domains despite the fact that the domain size was 10 nm; 10 nm is suggested to be the typical exciton diffusion length.[18] This difference in $\boldsymbol{PCE}$s was attributed to the fact that gains due to improved domain connectivity, and larger domain sizes, were offset by increased charge trapping due to diffuse interfacial regions. The simulations further suggested that increased purity of the domain phases and narrowing the interfacial region would have a more immediate impact on improving the device performance than optimizing the domain sizes. It is known experimentally that the length-scales of phase separation increase along with the phase purity, which has a potential counterbalancing effect.[19-21]

In this study we investigated the interrelations between aspects of the morphology, the carrier dynamics and the device performance. We produced three fundamentally different morphologies of the P3HT:phenyl-C_{61}-butyric acid methyl ester ($PC_{61}BM$) (1:1) BHJ system, using different processing strategies: solvent casting, thermal annealing and super critical carbon dioxide ($scCO_2$) processing. In a recent study we showed that $scCO_2$ processing was as a low-temperature processing protocol for organic solar cells.[22] The morphologies (differing degrees of phase purities, or degrees of intermixing, and average domain sizes) were examined using energy filtered transmission electron microscopy (EFTEM) and UV-vis absorption spectroscopy. The transport properties (charge carrier densities, carrier mobilities and non-geminate recombination) were

examined using photo-CELIV. It is evident from this study that trade-offs between changes in the morphology and associated changes in magnitude of the effects on transport parameters, and device parameters, need to be considered in device design.

3.2 EXPERIMENTAL SECTION

3.2.1 Materials

Details of P3HT and PEDOT:PSS are included in Chapter 2. $PC_{61}BM$ with 99.5% purity was purchased from American Dye Source Inc. and used as received.

3.2.2 Experiments

3.2.2.1 Device fabrication

ITO-coated glass substrates were ultrasonicated and cleaned in deionized water, acetone and isopropanol sequentially for 10 minutes for each step. The substrates were then treated under UV-ozone for 10 minutes. ~50 nm PEDOT:PSS were subsequently spincoated on the substrates, followed by 20 min thermal annealing at 120 °C to remove excess water. After the annealing, the substrates were transferred to nitrogen filled glovebox (oxygen<0.1 ppm, moisture<0.1 ppm) immediately for active layer spincoating and electrode deposition.

P3HT:$PC_{61}BM$ (1:1) solutions were prepared by dissolving highly regioregular P3HT and $PC_{61}BM$ in chlorobenzene. The solution was then shaken on a stirrer for 10 hours to make it homogeneous. After being filtered by 0.45 μm filters, the solution was

spin coated on PEDOT:PSS pre-coated ITO substrates to form the active layers (~100 nm). Thin films were spin-cast from chlorobenzene/P3HT:$PC_{61}BM$ (1:1) solutions. A subset of these samples was thermally annealed at temperature $\boldsymbol{T}$=150 °C for 15 min; another set was processed using $scCO_2$ under conditions of pressure $\boldsymbol{P}$=10.34 MPa and $\boldsymbol{T}$=50 °C for 5, 15, 30 and 45 min. These different conditions were used in order to create materials different morphologies. We note here that in our previous study, a chlorobenzene/7vol% nitrobenzene mixture was used to cast the samples. This mixture yields samples of different morphologies.

Quantitatively different morphologies may be produced through the use of different $scCO_2$ processing conditions, time $\boldsymbol{t}$, pressure $\boldsymbol{P}$ and temperature $\boldsymbol{T}$. $scCO_2$ is a mild plasticizing solvent for the blend and has a mildly preferential interaction. The activity of this solvent is readily changed by variations in $\boldsymbol{T}$ and $\boldsymbol{P}$. Therefore the extent of separation (domain sizes and purity/intermixing) may be manipulated by experimentally changing $\boldsymbol{T}$, $\boldsymbol{P}$ and $\boldsymbol{t}$. Details about $scCO_2$ processing apparatus and procedure can be found elsewhere.[22]

After the processing of the active layers, the devices were completed by depositing 1 nm lithium fluoride and 100 nm Al as the top electrode using thermal evaporation through shadow masks, at a typical pressure of 10^{-7} mbar. The $scCO_2$-processed samples were exposed to air while transferred between the $scCO_2$ apparatus and the glove box. For photo-CELIV measurement, the LiF was omitted in order to minimize the injection current and Al was 70 nm.[23]

3.2.2.2 EFTEM

The active layer morphology was studied using EFTEM in a TEM (JEOL 2100F) equipped with a Gatan #863 Tridiem imaging filter, operated at an acceleration voltage of 200 kV. The active layer of the devices was floated from deionized water and picked up onto copper grids (Ted Pella, Inc.) prior to TEM. The spectral images were collected using an energy slit width of 8eV and a step width of 0.2 eV, from -5 to 40 eV, covering the zero loss regime and plasmon loss regime on the energy loss spectra.

3.2.2.3 UV-vis absorption spectroscopy

Absorption measurement were conducted with a spectrophotometer (Perkin Elmer Lambda 750S) using a thin film accessory.

3.2.2.4 Photo-CELIV

Measurements were conducted in a cryostat (Janis VPF-100), which provides a vacuum of 1 mTorr and a wide range of temperatures. Laser pulses (Quantel BrilliantEazy, λ=532 nm) were incident from the ITO side and the intensity was attenuated using neutral density filters. A linearly increasing voltage was applied over the device, using a function generator (BK Precision 4075), to extract the photo-generated current transient, which was amplified by a preamplifier (FEMTO DLPCA-200) and recorded by a digital oscilloscope (Tektronix TDS3052C).

3.2.2.5 J-V curve characterization

Photocurrent curves were measured under ambient condition at AM 1.5G (Oriel solar simulator) illumination using a semiconductor parameter analyzer (Agilent 4156C).

3.3 RESULTS AND DISCUSSION

EFTEM and UV-vis absorption spectroscopy both provide a consistent assessment of the relative degrees of intermixing and phase purities of the samples. Images of the morphologies of the active layers, processed using different strategies,[19, 22] and examined using EFTEM, are shown in Figure 3.1 for the as-cast sample (a, d), $scCO_2$ processed sample (b, e), and thermally annealed sample (c, f). Spectral images were taken from -5.0 eV to 40.0 eV, with a step size of 0.2 eV. Due to the offset in the plasmon peak positions in the electron energy loss spectra (EELS) of P3HT and $PC_{61}BM$, image contrast based on local composition was obtained by using the appropriate range(s) of energy loss, where one species produces a higher scattering intensity than the other.[24] In the energy range between 21.7 eV and 25.9 eV, the P3HT-rich phase appears bright (Figures 3.1(a), (b) and (c)); between energies 31.7 eV and 37.1 eV, the $PC_{61}BM$-rich phase renders bright (Figures 3.1(d), (e) and (f)).

A cursory examination of Figures 3.1(a), (b) and (c) reveals that the thermally annealed sample possesses a well-developed domain structure; the P3HT rich and $PC_{61}BM$ rich phases in the as-cast and sc-CO2 processed samples appear to be much smaller and less defined due to significantly more intermixing between the phases. The P3HT-rich domain sizes of the $scCO_2$ processed samples are comparable to those of the

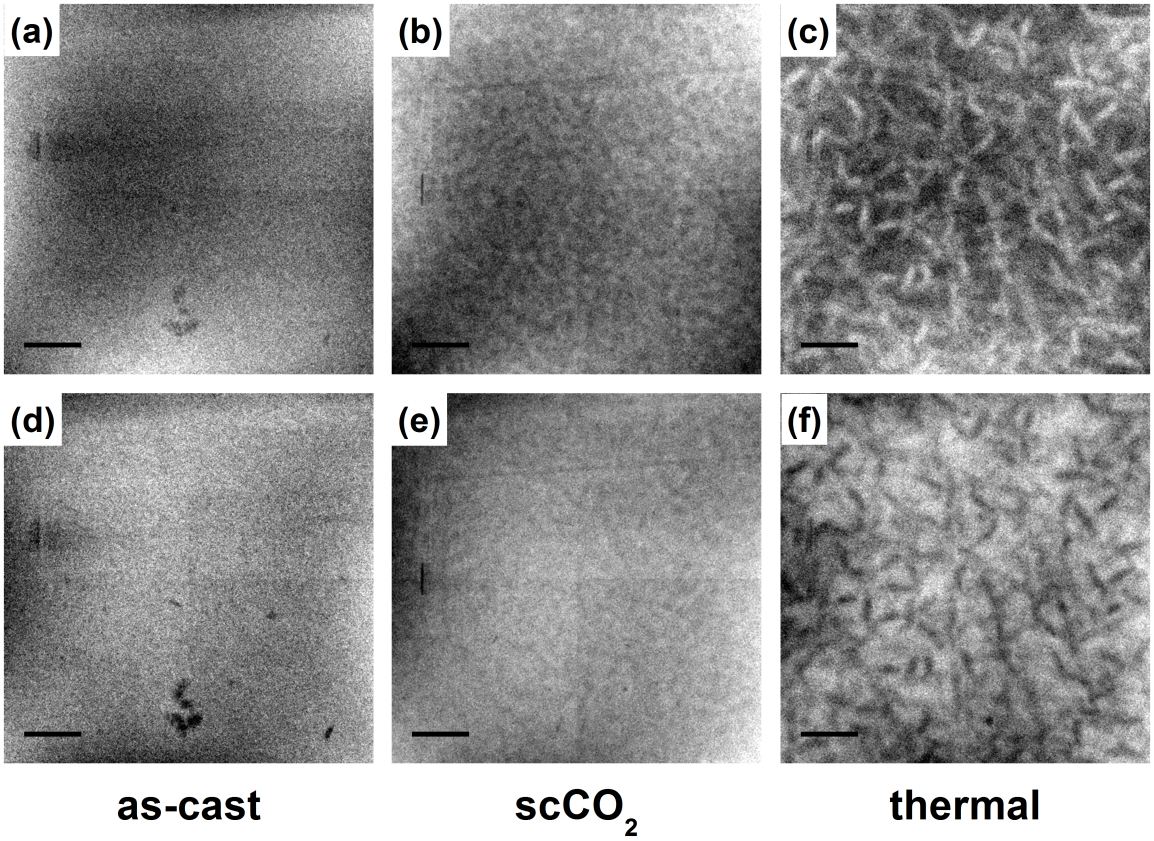

Figure 3.1 EFTEM images of P3HT:$PC_{61}BM$ (1:1) thin films spun from chlorobenzene solution. (a), (d) show results from as-cast, (b),(e) from $scCO_2$ annealing and (c), (f) from thermal annealing. In the top row, the energy window is selected that P3HT component is bright and $PC_{61}BM$ component is dark while in bottom row, P3HT component dark and $PC_{61}BM$ component bright. All scale bars are 50 nm.

as-cast sample, whereas those of the thermally annealed sample are appreciably larger. Because of the small domain sizes of the as-cast and $scCO_2$ processed samples, the interfacial region between their donor and acceptor phases is much larger than that of the thermally annealed sample. As mentioned in the Introduction, photogenerated excitons must reside within, or migrate to, the interfacial region in order to be dissociated; they would otherwise undergo geminate recombination within the phase where they were generated. In the P3HT:$PC_{61}BM$ BHJ system, most excitons are generated within the P3HT-rich phase because the P3HT absorption peak resides in the visible range whereas

the $PC_{61}BM$ absorption peak resides in the ultraviolet range. Smaller P3HT-rich domain sizes and larger interfacial areas should lead to higher initial charge carrier densities in the as-cast and $scCO_2$ processed samples than in the thermally annealed sample, for the same illumination intensity. Note that with smaller P3HT-rich domains, the pathway for holes to be transported through the active layer and reach the anode is appreciably longer and the probability of trapping and/or recombination would therefore be higher.

Qualitative information about the relative phase purities between samples was obtained by extracting the selected-area EELS spectra from the EFTEM images. Based on visual contrast, as seen in Figure 3.1, small regions (c.a. 5 x 5 nm^2) corresponding to P3HT- and $PC_{61}BM$-rich phases were selected from multiple locations across the entire imaged area: five each from the as-cast sample, ten each from the $scCO_2$ processed sample and ten each from the thermally annealed sample. The EELS spectra of these selected regions, and of the full imaged area, were extracted from the images, and the plasmon peak positions were calculated from a Gaussian fit. Representative EELS spectra and their Gaussian fits are shown in the supporting information section, Figure 3.6. The average peak position and standard deviation were calculated for the selected areas corresponding P3HT- and $PC_{61}BM$-rich areas, respectively; the results are summarized in Figure 3.2.

The two dash-dot lines in Figure 3.2 are plasmon peak positions of pure P3HT and of pure $PC_{61}BM$; this was discussed earlier.[22] The dashed line denotes the average plasmon peak position associated with a fully-mixed (homogeneous) P3HT:$PC_{61}BM$ (1:1) blend. The location of this line was calculated to be approximately 24.11 eV by taking

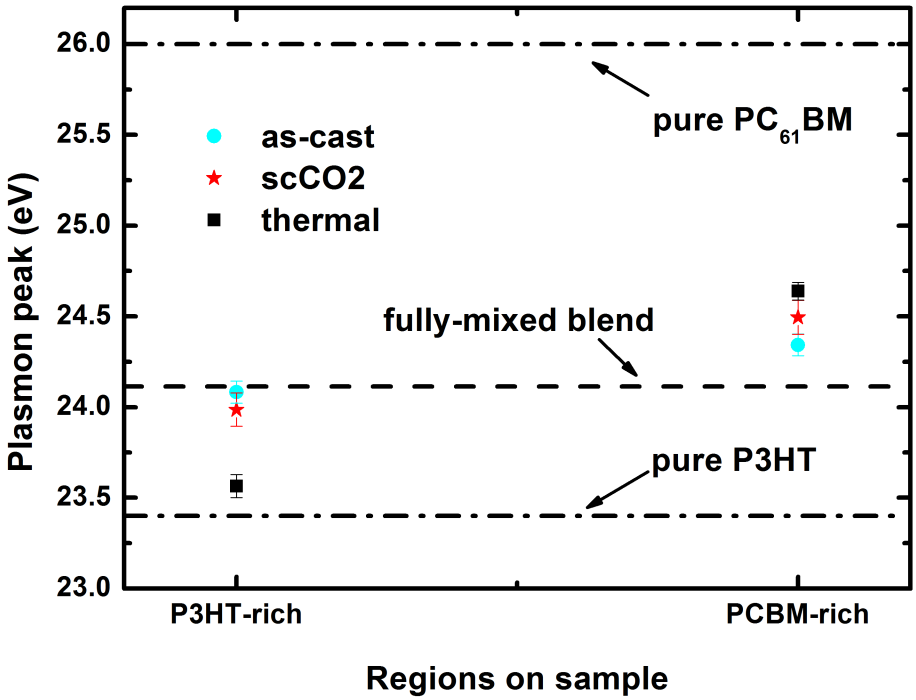

Figure 3.2 Plasmon peak positions of P3HT and $PC_{61}BM$ rich domains acquired from EFTEM images of P3HT:$PC_{61}BM$ (1:1) samples processed under different conditions.

the plasmon peak of the fully imaged area. The extent to which each data point deviates from the location of this line is a qualitative indicator of the purity of the phase, relative to the overall blend composition. As expected, the phase purity is lowest in the as-cast sample; the peak positions of P3HT-rich and $PC_{61}BM$-rich "domains" are very close to that of a homogeneous 1:1 mixture. Both $scCO_2$ processing and thermal annealing induced a greater extent of phase separation and improved the phase purity of the domains. This is indicated by the larger deviation of their peak positions, with the highest phase purity exhibited by the thermally-annealed sample. It is worth noting, however, that unlike thermal annealing, $scCO_2$ processing improved the phase purity without significantly coarsening the domains (readily controlled through changes in ***t***, ***P*** and ***T***),

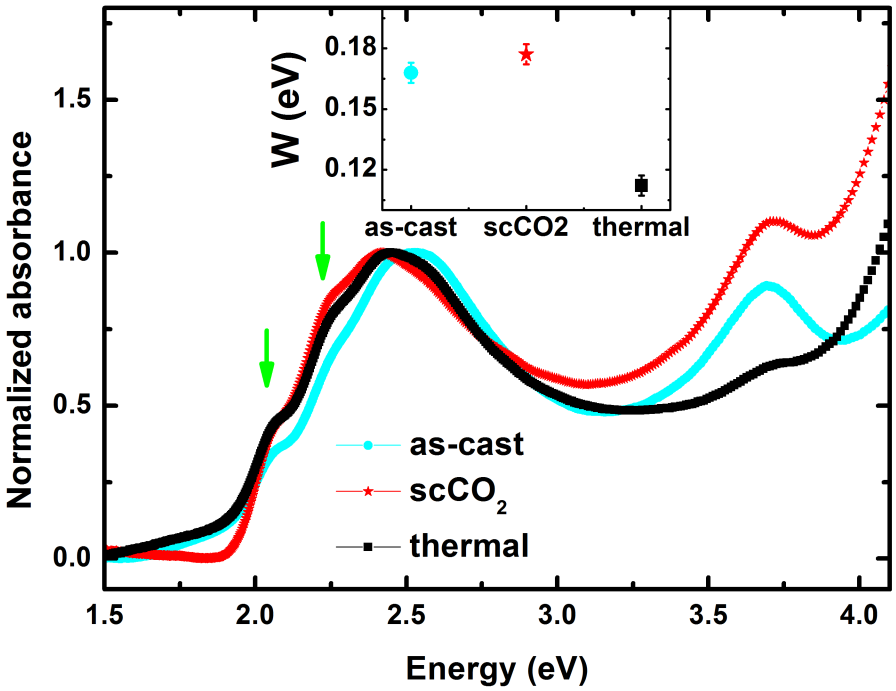

Figure 3.3 UV-vis absorption spectra of as-cast, $scCO_2$ processed and thermal annealed samples. Inset shows the free exciton bandwidths W.

which could be useful for processing material systems where macroscopic aggregation upon thermal annealing becomes problematic with regards to exciton diffusion lengths.[25]

The foregoing investigation indicates that the purity of the P3HT and $PC_{61}BM$ phases of the thermally annealed and $scCO_2$ processed samples are enhanced in relation to that of the as-cast sample; this observation is corroborated by subsequent UV-vis absorption spectroscopy measurements. Absorption spectra of three samples are shown in Figure 3.3. The absorption in the lower energy (<2.5 eV) region of the spectrum of the P3HT:$PC_{61}BM$ (1:1) blend is primarily due to P3HT absorption, while at higher energies (>2.5 eV) the absorption is from both P3HT and $PC_{61}BM$.[26] It is generally accepted that

the ordering of $PC_{61}BM$ aggregates has a negligible effect on the device performance.[24, 27] Therefore, only the P3HT spectra is of particular interest in our study.

The two peaks (shoulders) denoted by arrows in Figure 3.3 are associated with absorption by the crystalline P3HT phase. The interchain π-π interactions, which constitute low energy states, are responsible for the lower energy peak, whereas the peak located at energy 2.4 eV is due to the more disordered amorphous P3HT phase, in which high energy intrachain states are formed.[28, 29] The relative intensities of the two lower energy shoulders are therefore good indicators of the degree of polymer chain ordering/packing in the P3HT phase. Both shoulders, located at ~2.1 eV and ~2.25 eV, are more pronounced in the $scCO_2$ processed and the thermally annealed samples than in the as-cast sample, indicating an increased degree of ordering/packing of the P3TH polymer chains in the domains. This is consistent with the EFTEM/EELS measurements discussed earlier. We note that it is well documented that when $PC_{61}BM$ resides between P3HT chains they disrupt ordering. Therefore the exclusion of $PC_{61}BM$ from P3HT-rich domain would be associated with increased ordering/packing of P3HT chains. This improved ordering would facilitate higher hole mobilities, which we discuss later.[14]

The UV-Vis spectra provide additional information about the electronic structure. To this end, the free exciton bandwidths $\boldsymbol{W}$ were calculated using information from the UV-vis spectra using the following equation:

$$\frac{A_{0-0}}{A_{0-1}} \approx \left(\frac{1 - 0.24W / E_p}{1 + 0.073W / E_p} \right)^2 \tag{4.1}$$

where $\boldsymbol{A_{0-0}}$and $\boldsymbol{A_{0-1}}$ are peak absorbances, identified by arrows in Figure 3.3; $\boldsymbol{E_p}$ is the intermolecular vibrational energy, which is fixed to 0.179 eV. The results are shown in the inset in Figure 3.3. The magnitude of $\boldsymbol{W}$ is indicative of the conjugation length and of the size of the P3HT aggregates; the latter has a larger effect.[28] A larger value of $\boldsymbol{W}$ is indicative of a smaller conjugation length, which would be associated with a larger degree of disorder. The thermally annealed sample has the smallest $\boldsymbol{W}$ whereas the $scCO_2$-processed sample has the largest. For the crystalline P3HT phase in the active layer, W is proportional to the nearest neighbor interchain excitonic interaction, based on the nearest-neighbor-only approximation. This nearest neighbor interaction becomes weaker with increasing conjugation length in the polymer chain.[28] The smallest $\boldsymbol{W}$, exhibited by the thermally annealed sample, is indicative of a longer conjugation length. This is consistent with the highest phase purity, and manifested in the red-shift of the absorption peak at ~2.4 eV. As the conjugation length increases, the optical gap decreases due to stronger intrachain coupling between neighbor thiophene rings; this causes the bathochromic shift.[28] Interestingly, the $scCO_2$-processed sample has the largest $\boldsymbol{W}$, suggesting a shorter conjugation length. However the purer phases and red-shifted absorption peak suggests a longer conjugation length compared to the as-cast sample. This apparent discrepancy is attributed to the fact that $\boldsymbol{W}$ also increases with coarsening aggregate size.[28] The slightly larger P3HT aggregate size of the $scCO_2$-processed sample has a larger effect on the magnitude of $\boldsymbol{W}$ than that due to the effect of longer conjugation length. This is the reason that the $scCO_2$-processed sample has the largest $\boldsymbol{W}$ of the three samples.

The value of ***W*** also manifests information about the width of the Gaussian distribution of density of localized states; the localized states may serve as carrier traps, at the HOMO and LUMO levels.[30] This suggests that the $scCO_2$-processed sample has the deepest distribution of traps, whereas the thermally annealed sample has the shallowest distribution. In energetically disordered organic materials such as P3HT, charge carriers are transported via hopping between localized states. As the localized states distribution gets deeper in the $scCO_2$-processed sample, charge carriers are more likely to be trapped and recombine with opposite charges. So the largest values of ***W*** in the $scCO_2$-processed sample would be indicative of the highest free carrier recombination rate. This information is corroborated by the photo-CELIV experiments, which directly measures the carrier recombination, as discussed below.

The charge carrier transport properties, including charge carrier densities, mobilities and recombination rates, of devices processed using different protocols were characterized using photo-CELIV; the results are plotted in Figure 3.4. In photo-CELIV, after a specified interval of time delayed after the initial application of a short incident laser pulse, a linearly increasing voltage is applied to the device to extract charge carriers.[31] Typical current transients in the dark (in the absence of a laser pulse) and for different delay intervals are reported in the supporting information section, Figure 3.7, for all three samples. The dynamics of the charge carrier densities are plotted as a function of delay time on a log-log scale in Figure 3.4(a). For all samples, it was evident that as the delay time increased, the density of the extracted charge carriers decreased due to recombination in the active layer. Based on the microsecond time scales in our study, this

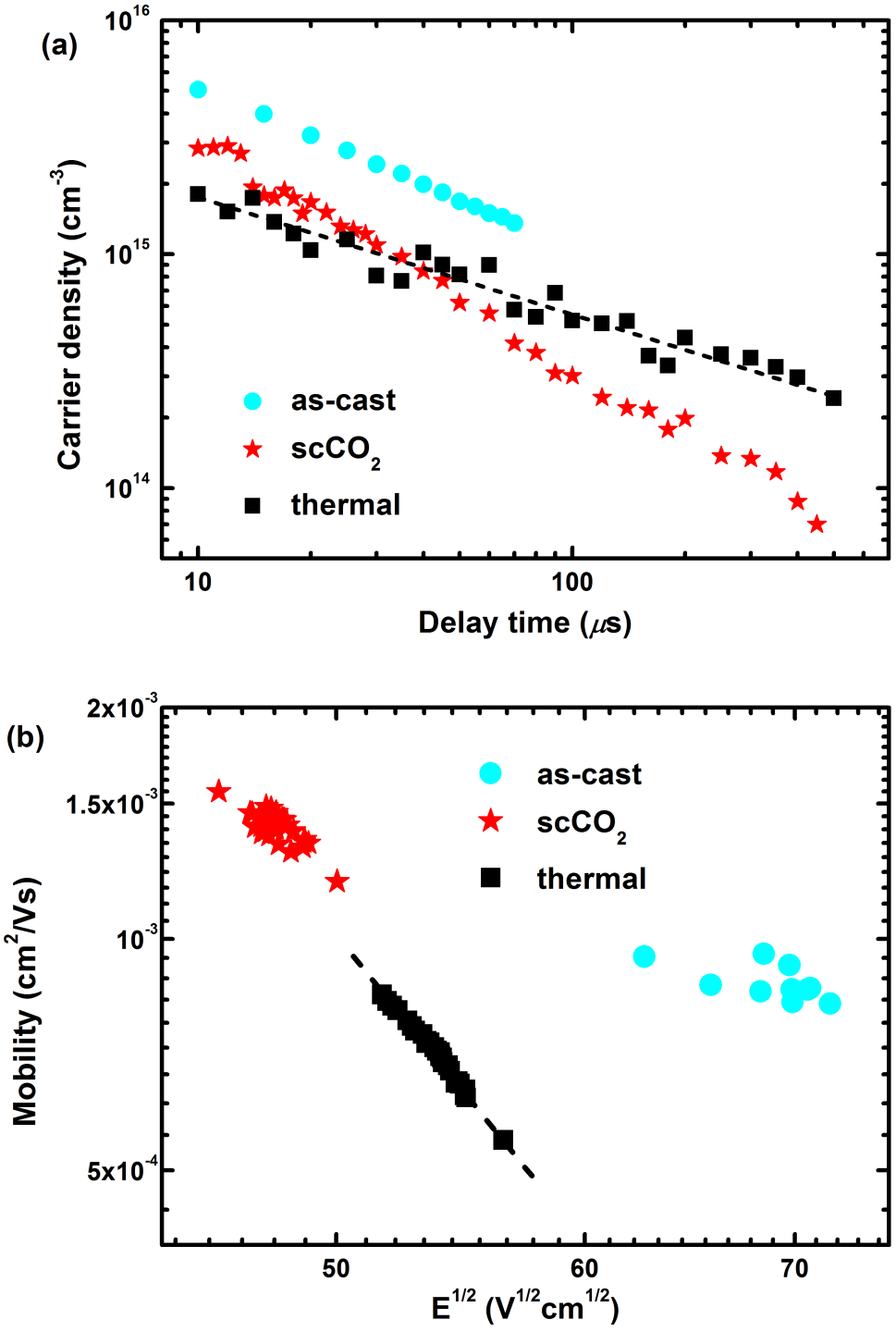

Figure 3.4(a) Concentration of extracted charge carriers as a function of delay time and (b) Electric field dependence of carrier mobility characterized by photo-CELIV measurement on devices processed under different conditions. Dashed lines are for guides to the eye only.

would be non-geminate recombination of free charge carriers during transport, after the exciton dissociation. This is because the exciton lifetime before dissociation is comparable to sub-nanosecond time scales in the P3HT:$PC_{61}BM$ system.[32]

During the delay time from 10 μs to 500 μs, all decay curves exhibit a power law dependence on time, where $\boldsymbol{n(t) \propto t^{\alpha}}$. By fitting the data sets to the power law formula and extrapolating to $\boldsymbol{t}$ = 0 μs, the initial carrier densities $\boldsymbol{n(0)}$ was extracted from the for each sample: $\boldsymbol{n(0)_{as-cast}}$ = (1.94±0.05)×10^{16} cm^{-3}, $\boldsymbol{n(0)_{scCO_2}}$ = (2.76±0.28)×10^{16} cm^{-3} and $\boldsymbol{n(0)_{thermal}}$ = (5.54±0.52)×10^{15} cm^{-3}. To be exact, $\boldsymbol{t}$ should be extrapolated to the time immediately after the exciton dissociation instead of 0; however, this sub-nanosecond time scale is negligible in relation to the time resolution limit and the calculation. Our calculations, not surprisingly indicate that the initial charge carrier density after exciton dissociation is almost 4 times larger in the as-cast sample and 5 times larger in the $scCO_2$ processed sample than in the thermally annealed sample. The relative differences between the initial carrier densities are consistent with information we learned about the structures of the samples: the interfacial (intermixed) regions of the $scCO_2$ processed and as-cast samples are significantly larger than those of the thermally annealed sample. While the morphologies of the as-cast and the $scCO_2$ processed samples are very similar, $\boldsymbol{n(0)_{scCO_2}}$ is ~40% larger than $\boldsymbol{n(0)_{as-cast}}$. We attribute this to the details of the morphology that contribute to a reduction of geminate recombination of excitons thus enabling the formation of additional free carriers in the $scCO_2$-processed sample.[33]

The free carrier recombination rates, reflected in the exponents $\boldsymbol{\alpha}$, were exacted by fitting the data to the power law formula, yielding $\boldsymbol{\alpha_{as-cast}}$ = -0.61±0.01, $\boldsymbol{\alpha_{scCO_2}}$ = -

0.96±0.04 and $\alpha_{thermal}$ = -0.50±0.03. The free carrier recombination is most significant in the $scCO_2$-processed sample and least in the thermally annealed sample. This observation is consistent with the morphology and the free exciton bandwidth analysis. Morphologically, a less connected network of the P3HT phase in the $scCO_2$-processed sample would be responsible for trapping/recombination. The largest free exciton bandwidth exhibited by the $scCO_2$-processed sample indicates that carriers are least likely to escape once they are trapped at those sites; hence they would recombine with opposite charges. Higher recombination rates in the as-cast and $scCO_2$ processed sample are consistent with the lower FFs, as shown below, determined from the J-V curves of the as-cast and the $scCO_2$ annealed solar cells. In other words a smaller percentage of free carriers arrive at the electrodes and are collected.[34]

Larger recombination rates are also consistent with lower V_{OC}, as discussed by Ripollet et al.[35] The V_{OC} is primarily determined by the difference between the quasi-Fermi levels (i.e. chemical potentials) E_{F_n} and E_{F_p} of holes and electrons, respectively, under illumination conditions; specifically $V_{OC} = (E_{F_n} - E_{F_p})/q$, where q is the elementary charge.[35] As electrons recombine with holes in these energetically disordered systems,[36] the difference between E_{F_n} and E_{F_p} decreases, leading to a lower V_{OC}. The trends in the magnitudes of the V_{OC} exhibited by the devices are consistent with this notion.

The shape of the charge carrier density decay is noteworthy. The recombination dynamics in these systems is distinctly different from the Langevin bimolecular recombination, which is usually assumed to occur in disordered organic systems in which

the carrier density dynamics takes the form of $\boldsymbol{n(t) = n(0)/[1 + (t/\tau_B)]}$, where $\boldsymbol{\tau_B}$ is the bimolecular lifetime.[23] That Langevin bimolecular recombination does not describe our system is well documented.[37-39] In fact, different models have been proposed to account for the difference between the actual recombination and the classical Langevin recombination.[40-43] In disordered systems the charges follow paths, via a hopping mechanism, along the A- and D-rich domains, which reduces the probability of recombination, compared to their ordered inorganic counterparts where band transport occurs.

The charge carrier mobilities were also determined and plotted on a semi-log scale as a function of the electric field in Figure 3.4(b). The photo-CELIV technique does not distinguish between hole or electron transport so the apparent mobilities we extracted are due to contributions from both types of carriers.[31] The values of the mobilities were calculated using

$$\mu = \frac{2d^2}{3At_{max}^2\left(1 + 0.36\frac{\Delta j_{max}}{j_0}\right)} \tag{4.2}$$

where $\boldsymbol{d}$ is the film thickness, $\boldsymbol{A}$ the voltage ramping rate, $\boldsymbol{t_{max}}$ the time at which the current density transient reaches maximum, $\boldsymbol{j_0}$ the displacement current and $\boldsymbol{\Delta j_{max}}$ the difference between maximum current density and $\boldsymbol{j_0}$; $\boldsymbol{t_{max}}$, $\boldsymbol{j_0}$ and $\boldsymbol{\Delta j_{max}}$ are retrieved from the current density transients.

The electric field dependencies of carrier mobilities in all cases is well-described by the Poole-Frenkel relationship $\boldsymbol{\mu(E) = \mu_{E=0} exp(CE^{1/2})}$; negative slopes at this relatively low electric field are commonly observed in P3HT systems[44, 45] at room

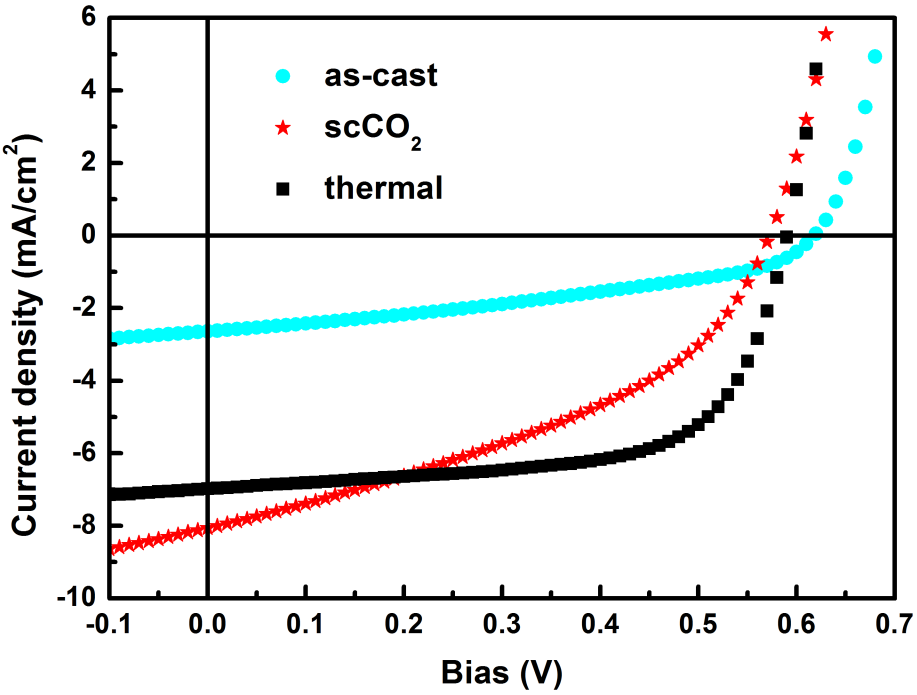

Figure 3.5 ***J-V*** *curves of P3HT:$PC_{61}BM$ (1:1) devices processed under different conditions. For as-cast devices,* $\boldsymbol{J_{SC}}$ *= 2.64 mA/cm^2,* $\boldsymbol{V_{OC}}$ *= 0.62 V,* $\boldsymbol{FF}$ *= 0.38,* $\boldsymbol{PCE}$ *= 0.62%; for scCO2 processed devices,* $\boldsymbol{J_{SC}}$ *= 8.1 mA/cm^2,* $\boldsymbol{V_{OC}}$ *= 0.58 V,* $\boldsymbol{FF}$ *= 0.40,* $\boldsymbol{PCE}$ *= 1.9%; for thermally annealed devices,* $\boldsymbol{J_{SC}}$ *= 7.0 mA/cm^2,* $\boldsymbol{V_{OC}}$ *= 0.60 V,* $\boldsymbol{FF}$ *= 0.64,* $\boldsymbol{PCE}$ *= 2.7%.*

temperature and are attributed to the energetic and structural disorder in the system.[46] Since our goal is to associate the value of the mobility with the $\boldsymbol{J_{SC}}$, when there is no external electric field, all mobilities were fitted using the Poole-Frenkel equation to obtain $\boldsymbol{\mu_{E=0}}$; $\boldsymbol{\mu_{E=0|as-cast}}$ = (6.63±0.37)×10^{-3} $cm^2V^{-1}s^{-1}$, $\boldsymbol{\mu_{E=0|scCO_2}}$ = (1.59±0.54)×10^{-2} $cm^2V^{-1}s^{-1}$ and $\boldsymbol{\mu_{E=0|thermal}}$ = (9.47±0.96)×10^{-2} $cm^2V^{-1}s^{-1}$. It is interesting to note that the relative magnitudes of the mobilities reported here are entirely consistent with the degree of phase purity reported above. The highest mobilities were measured in the thermally annealed sample, which possessed the highest degree of phase purity, followed by the $scCO_2$-processed sample.

Finally we discuss the device characteristics in further detail, in light of the foregoing information about the transport properties. The ***J-V*** curves of devices $scCO_2$ annealed or thermal annealed for different times are reported in the section containing supporting information, Figure 3.8; all the parameters are summarized in Table 3.1. The ***J-V*** curves of P3HT:$PC_{61}BM$ (1:1) devices processed under different conditions are shown in Figure 3.5; the device performance indicators for each processing condition are reported in the figure caption. All values were not corrected for spectral mismatch. The $scCO_2$-processed sample exhibits the highest short circuit current, whereas the as-cast sample exhibits the lowest, $\boldsymbol{J_{SC}^{thermal} \sim J_{SC}^{scCO2} \sim 3 J_{SC}^{as-cast}}$. Recall that the initial carrier densities were such that $\boldsymbol{n(0)_{scCO2} \sim n(0)_{as-cast} \sim 5 n(0)_{thermal}}$. This suggests that the recombination of carriers in the $scCO_2$-processed sample is appreciably larger than in the thermally annealed sample. The recombination rates determined by the CELIV experiments confirm this assessment.

The significantly larger $\boldsymbol{J_{SC}}$ in the $scCO_2$ processed sample compared to the as-cast suggests that improving the phase purity would enhance the device performance to a larger degree than optimizing the domain size, considering that the domain sizes of both samples are comparable.

With regard to the $\boldsymbol{V_{OC}}$, the $scCO_2$-processed sample possesses a lower value than the thermally annealed sample. This has been explained; it is due to faster recombination rates in the $scCO_2$-processed sample, which is responsible for a decrease of the difference between the quasi-Fermi levels of holes and electrons. Comparing the thermally annealed and as-cast samples, we found that the $\boldsymbol{V_{OC}}$ of the thermally annealed sample is slightly

smaller than that of the as-cast sample. This is attributed to the longer conjugation length of P3HT polymer chains in the thermally annealed sample, which is consistent with the higher phase purity and reflected in the red-shifted absorption peak in the UV-Vis spectra in Figure 3.3. The HOMO of P3HT increases along with the conjugation length. Noting that the $\boldsymbol{V_{OC}}$ is approximately proportional to the difference between the HOMO of donor phase and the LUMO of acceptor phase, the longer conjugation length in P3HT would be responsible for this lower $\boldsymbol{V_{OC}}$. A similar relationship was also determined for different annealing times, as shown in Table 3.1.

The fill factor, determined to be $\boldsymbol{FF_{as-cast}}$ = 0.38, $\boldsymbol{FF_{scCO_2}}$ = 0.40, $\boldsymbol{FF_{thermal}}$ = 0.64, for the samples, is associated with many variables and cannot be fully explained by a single transport.[47] However, the higher recombination rates in the as-cast and $scCO_2$-processed samples ($\boldsymbol{\alpha_{as-cast}}$ = -0.61±0.01, $\boldsymbol{\alpha_{scCO_2}}$ = -0.96±0.04, $\boldsymbol{\alpha_{thermal}}$ = -0.50±0.03), which may be due to both disconnected domains and a deep distribution of localized states, at least qualitatively, explains the lower $\boldsymbol{FF}$ in those samples. Based on the results of the $scCO_2$ processed and thermally annealed samples, it is clear that the size and connectivity of domains have a significant effect on the recombination and consequently the $\boldsymbol{FF}$. Consistently lower $\boldsymbol{FF}$s in $scCO_2$ processed samples are reported in Table 3.1 for different annealing times.

3.4 CONCLUSIONS

We investigated the relation between the morphology of the active layer of a BHJ solar cell and the device performance. P3HT:$PC_{61}BM$ active-layer materials possessing three fundamentally different morphologies, characterized by domain size, phase purity and interfacial region, were prepared using different processing strategies (solvent casting, thermal annealing, $scCO_2$ processing).

The primary difference between the $scCO_2$-processed samples and the thermally annealed samples is the sc-CO2 processed samples possessed appreciably smaller average domain sizes. It is noteworthy that while the initial carrier densities of these samples were such that $\boldsymbol{n(0)_{scO_2}}$~5 $\boldsymbol{n(0)_{thermal}}$, the thermally annealed samples had comparable $\boldsymbol{J_{SC}}$s, and slightly better $\boldsymbol{PCE}$s than those of the $scCO_2$–processed samples. This was due to recombination rates that were twice as large in the sc-CO_2-processed samples: $\boldsymbol{\alpha_{scCO_2}}$ = -0.96±0.04 and $\boldsymbol{\alpha_{thermal}}$ = -0.50±0.03. The difference between the relaxation rates is also consistent with the lower device fill factors exhibited by the $scCO_2$-processed sample ($\boldsymbol{FF_{scCO_2}}$ = 0.40 and $\boldsymbol{FF_{thermal}}$ = 0.64).

The average domain sizes of the as-cast and the $scCO_2$-processed samples were comparable and their carrier densities were comparable: $\boldsymbol{n(0)_{as-cast}}$ = (1.94±0.05)×10^{16} cm^{-3}~ $\boldsymbol{n(0)_{scCO_2}}$ = (2.76±0.28)×10^{16} cm^{-3}. However, the $\boldsymbol{PCE}$s and the short circuit currents in the $scCO_2$-processed sample were three times as large as the as-cast sample. This is associated with the fact that the $scCO_2$-processed samples possessed higher degrees of phase purity and order than the as-cast samples. The carrier mobilities of the

$scCO_2$ samples were moreover, approximately 3 times as large $\boldsymbol{\mu_{E=0|as-cast}}$ = (6.63±0.37)×10^{-3} $cm^2V^{-1}s^{-1}$ and $\boldsymbol{\mu_{E=0|scCO_2}}$ = (1.59±0.54)×10^{-2} $cm^2V^{-1}s^{-1}$, which is consistent with the higher degrees of purity and order in the $scCO_2$ processed sample.

The foregoing provided insight into the connection between aspects of the morphology of the active layer, various transport parameters and device performance. This in principle provides further insight into morphological design for devices.

3.5 SUPPORTING INFORMATION

We note here that clearly the interface is of finite width of many nanometers.

Representative EELS spectra and corresponding Gauss fittings are displayed in Figure 3.6. We note here that the selected regions for EELS spectra were small in size (5 nm × 5 nm each) and were positioned in the center of each randomly chosen domain (5 domains for the as-cast sample and 10 domains for the thermally annealed and $scCO_2$ processed samples each) across the entire image area.

Exemplary transient currents from photo-CELIV characterization are shown in Figure 3.7. The charge carrier density was calculated by integrating the current density over time. For each sample, a decreased current density with delay time indicates fewer charge carriers are collected due to free carrier recombination.

$\boldsymbol{J}$-$\boldsymbol{V}$ curves of samples annealed in $scCO_2$ (10.34 MPa, 50 °C) and at high temperature (150 °C) for different periods of time are shown in Figure 3.8. All parameters, along with those from as-cast sample are summarized in Table 3.1. The

evolution of J_{SC}, V_{OC} and FF in the P3HT:$PC_{61}BM$ device as a function of annealing time has been studied and can be found elsewhere.[19, 22, 33, 48, 49]

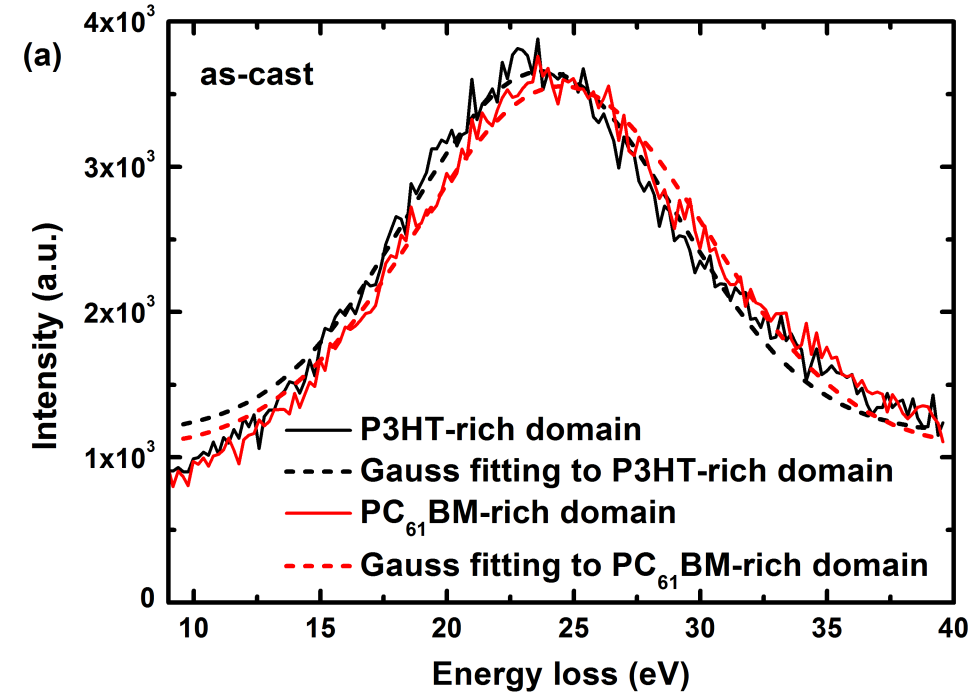

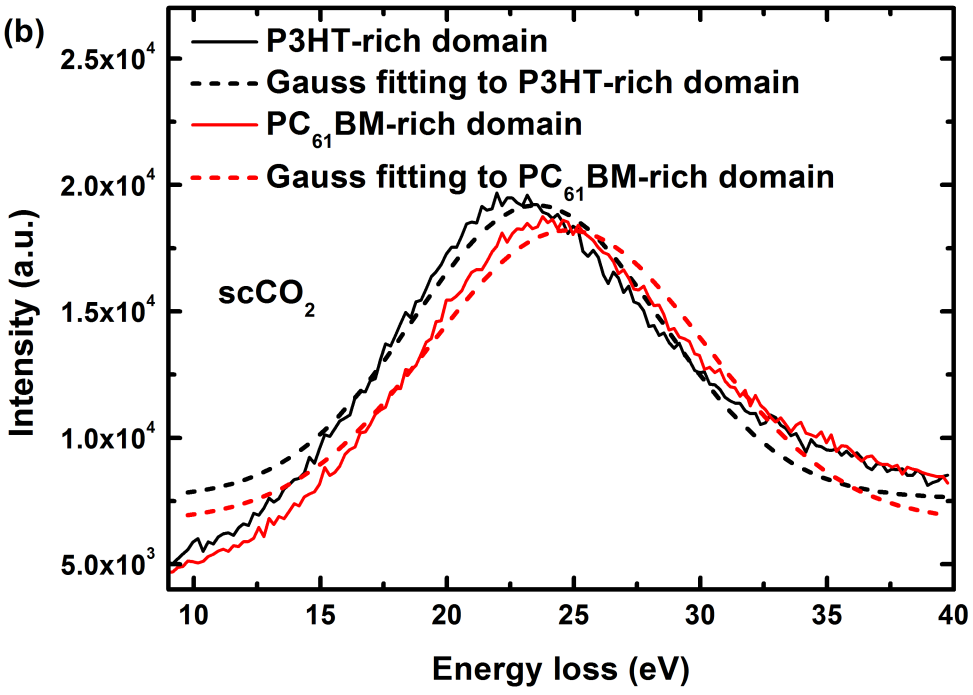

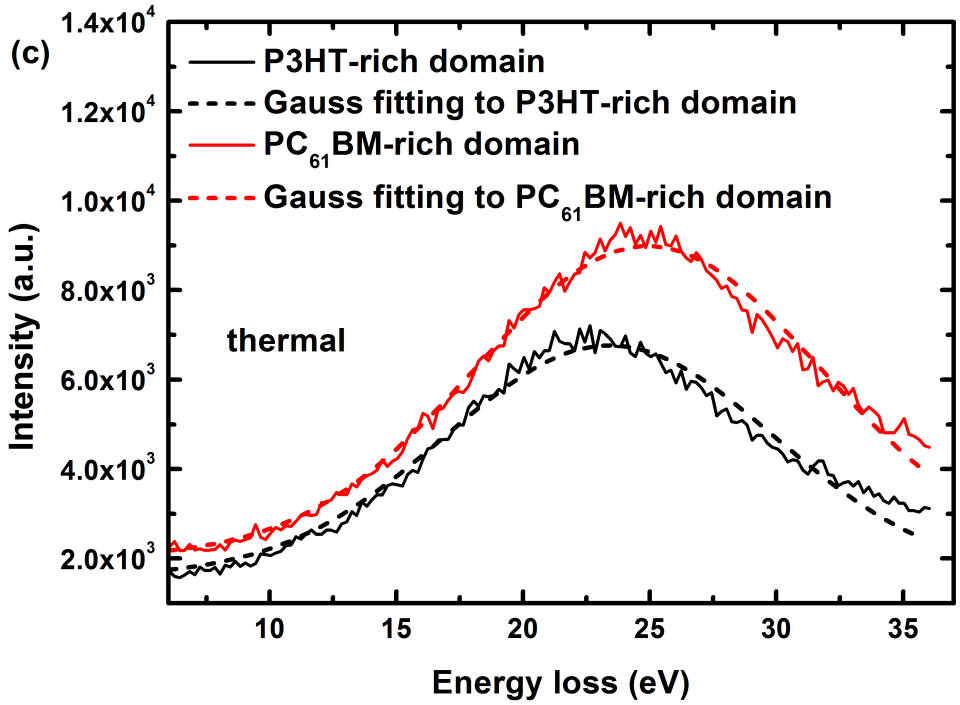

Figure 3.6 Representative EELS spectra and corresponding Gaussian peak fittings for both P3HT-rich and $PC_{61}BM$-rich domains from samples processed under different conditions: (a) as-cast, (b) processed in $scCO_2$ at 10.34 MPa and 50 °C for 30 min, and (c) annealed at 150 °C for 15 min.

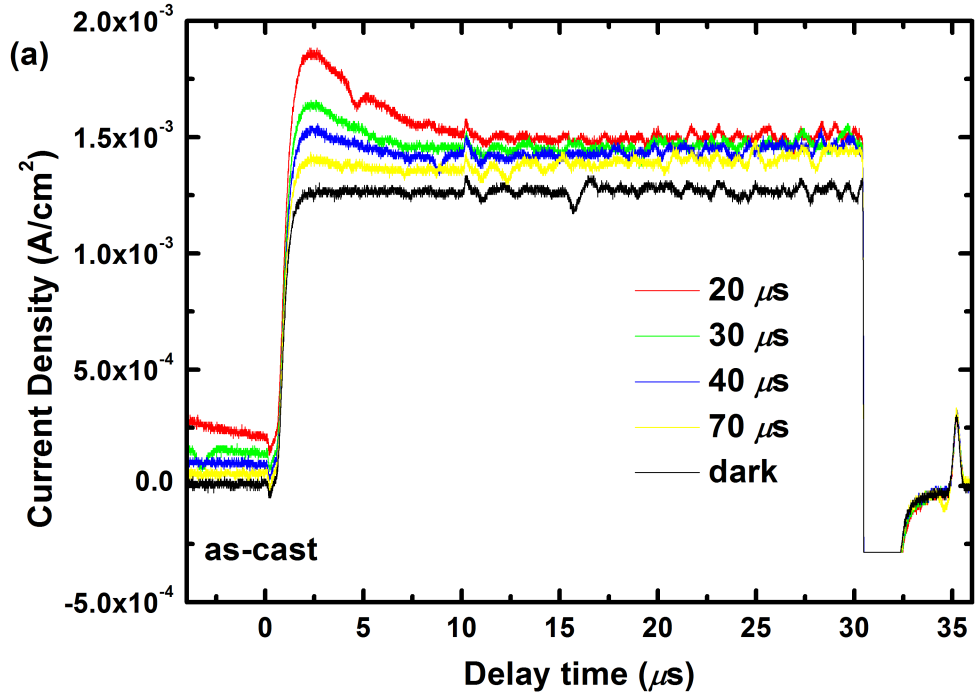

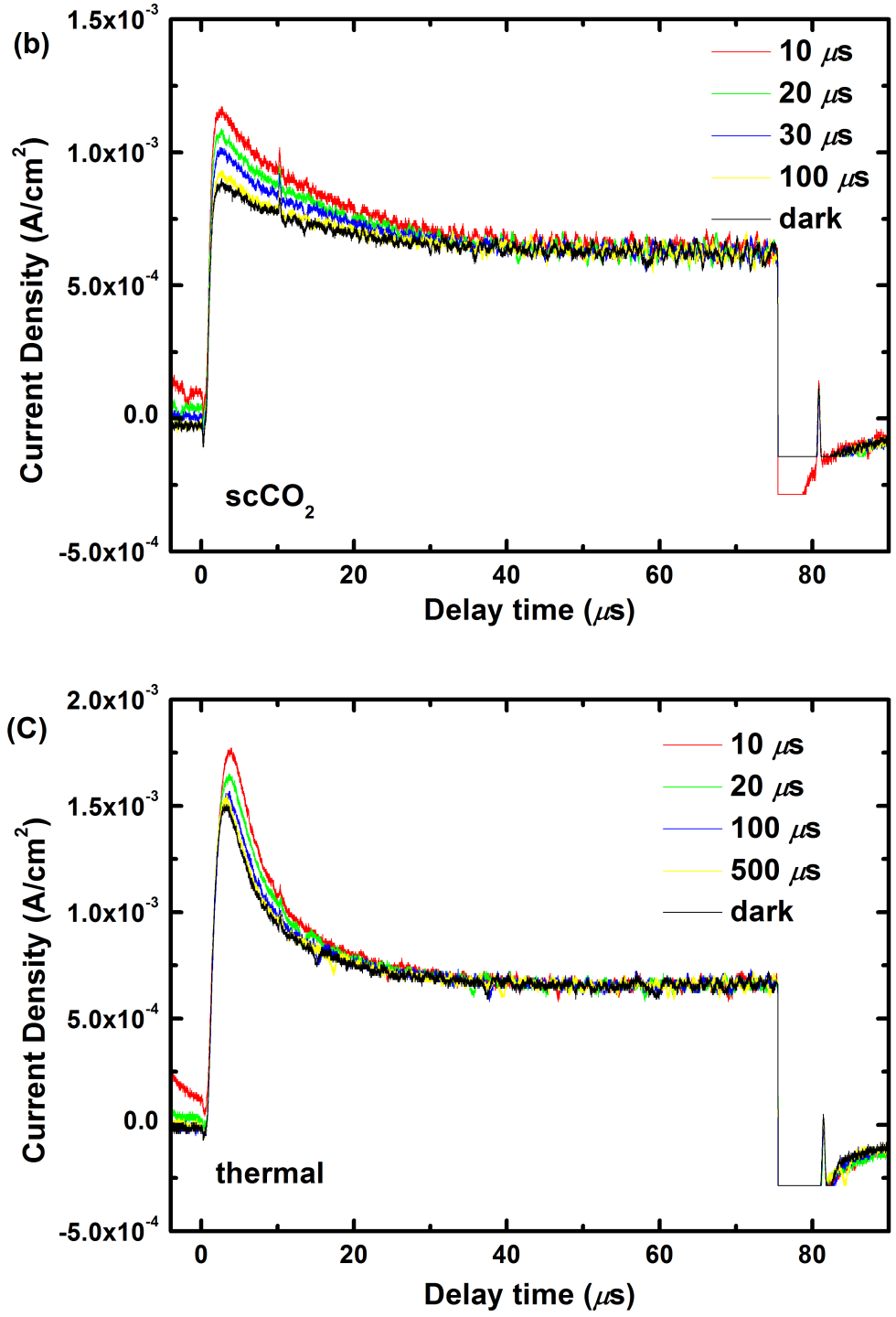

Figure 3.7 Representative photo-CELIV current transients from P3HT:$PC_{61}BM$ (1:1) devices of different processing conditions: (a) as-cast, (b) $scCO_2$ processed, and (c) thermal annealed.

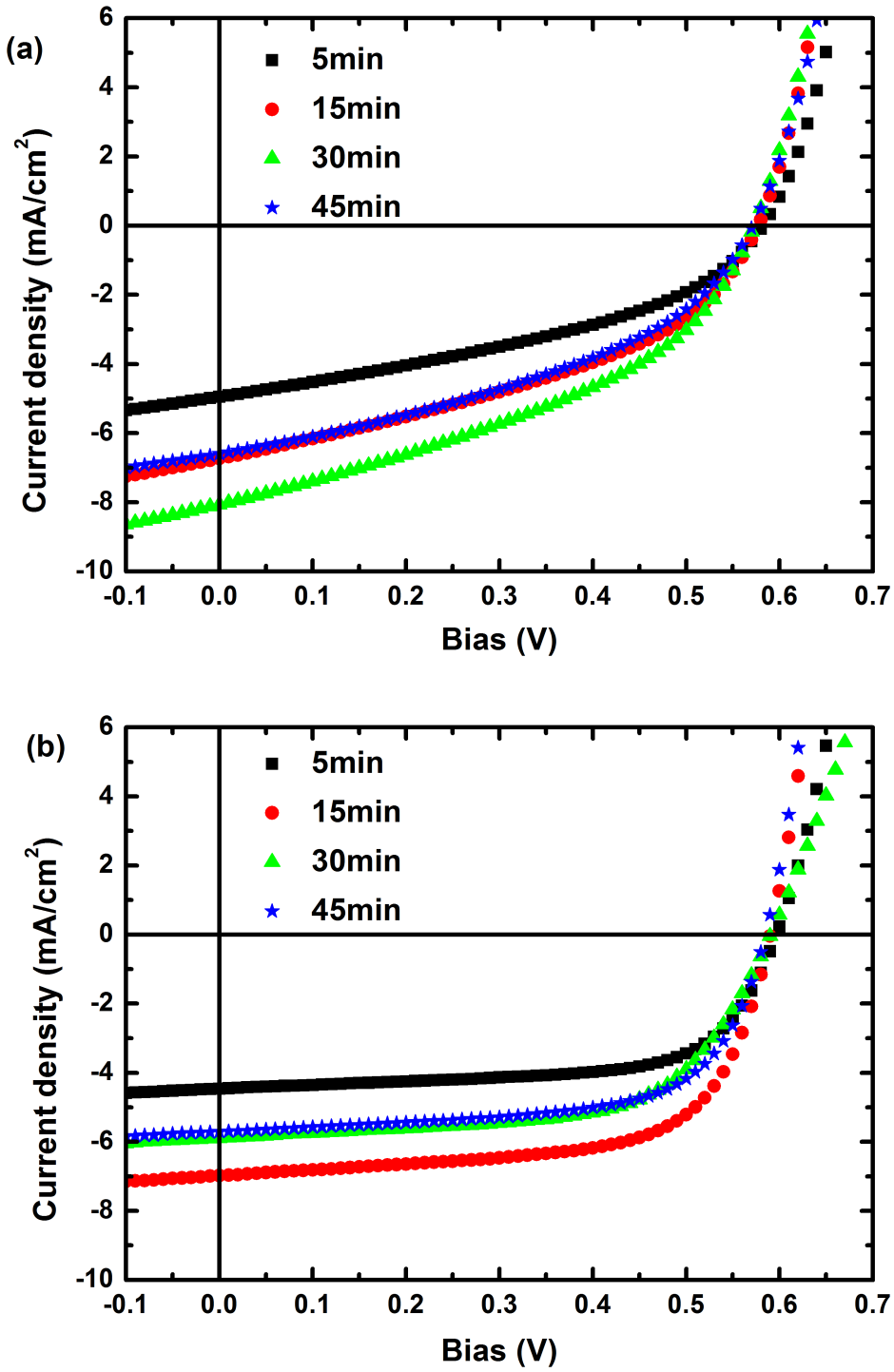

Figure 3.8 Current density-voltage curves of P3HT:PC$_{61}$BM (1:1) devices (a) processed in scCO$_2$ at 10.34 MPa and 50 °C and (b) thermal annealed at 150 °C for different periods of time.

Table 3.1 Device Performance Parameters of P3HT:$PC_{61}BM$ (1:1) BHJ Devices Prepared from Chlorobenzene

	as-cast	$scCO_2$ processing				thermal annealing			
		5 min	15 min	30 min	45 min	5 min	15 min	30 min	45 min
V_{OC} (V)	0.62	0.59	0.58	0.58	0.58	0.60	0.60	0.60	0.60
J_{SC} (mA/cm^2)	2.64	5.0	6.7	8.1	6.6	4.5	7.0	5.9	5.7
FF (%)	38	39	41	40	40	65	64	60	64
PCE (%)	0.62	1.2	1.6	1.9	1.5	1.8	2.7	2.1	2.2

3.6 REFERENCES

1. Kim, J. Y.; Lee, K.; Coates, N. E.; Moses, D.; Nguyen, T.-Q.; Dante, M.; Heeger, A. J. *Science* **2007,** 317, (5835), 222-225.
2. Hoth, C. N.; Schilinsky, P.; Choulis, S. A.; Brabec, C. J. *Nano Letters* **2008,** 8, (9), 2806-2813.
3. Krebs, F. C.; Gevorgyan, S. A.; Gholamkhass, B.; Holdcroft, S.; Schlenker, C.; Thompson, M. E.; Thompson, B. C.; Olson, D.; Ginley, D. S.; Shaheen, S. E.; Alshareef, H. N.; Murphy, J. W.; Youngblood, W. J.; Heston, N. C.; Reynolds, J. R.; Jia, S.; Laird, D.; Tuladhar, S. M.; Dane, J. G. A.; Atienzar, P.; Nelson, J.; Kroon, J. M.; Wienk, M. M.; Janssen, R. A. J.; Tvingstedt, K.; Zhang, F.; Andersson, M.; Inganäs, O.; Lira-Cantu, M.; de Bettignies, R.; Guillerez, S.; Aernouts, T.; Cheyns, D.; Lutsen, L.; Zimmermann, B.; Würfel, U.; Niggemann, M.; Schleiermacher, H.-F.; Liska, P.; Grätzel, M.; Lianos, P.; Katz, E. A.; Lohwasser, W.; Jannon, B. *Solar Energy Materials and Solar Cells* **2009,** 93, (11), 1968-1977.
4. Liang, Y.; Xu, Z.; Xia, J.; Tsai, S.-T.; Wu, Y.; Li, G.; Ray, C.; Yu, L. *Advanced Materials* **2010,** 22, (20), E135-E138.
5. He, Z.; Zhong, C.; Su, S.; Xu, M.; Wu, H.; Cao, Y. *Nat Photon* **2012,** 6, (9), 593-597.
6. Peet, J.; Heeger, A. J.; Bazan, G. C. *Accounts of Chemical Research* **2009,** 42, (11), 1700-1708.
7. Brabec, C. J.; Heeney, M.; McCulloch, I.; Nelson, J. *Chemical Society Reviews* **2011,** 40, (3), 1185-1199.
8. Pfannmöller, M.; Flügge, H.; Benner, G.; Wacker, I.; Sommer, C.; Hanselmann, M.; Schmale, S.; Schmidt, H.; Hamprecht, F. A.; Rabe, T.; Kowalsky, W.; Schröder, R. R. *Nano Letters* **2011,** 11, (8), 3099-3107.
9. Sariciftci, N. S.; Smilowitz, L.; Heeger, A. J.; Wudl, F. *Science* **1992,** 258, (5087), 1474-1476.
10. Barker, J. A.; Ramsdale, C. M.; Greenham, N. C. *Physical Review B* **2003,** 67, (7), 075205.
11. Moses, D.; Wang, J.; Heeger, A. J.; Kirova, N.; Brazovski, S. *Proceedings of the National Academy of Sciences* **2001,** 98, (24), 13496-13500.
12. Koster, L. J. A.; Smits, E. C. P.; Mihailetchi, V. D.; Blom, P. W. M. *Physical Review B* **2005,** 72, (8), 085205.
13. Yu, G.; Gao, J.; Hummelen, J. C.; Wudl, F.; Heeger, A. J. *Science* **1995,** 270, (5243), 1789-1791.
14. Sirringhaus, H.; Brown, P. J.; Friend, R. H.; Nielsen, M. M.; Bechgaard, K.; Langeveld-Voss, B. M. W.; Spiering, A. J. H.; Janssen, R. A. J.; Meijer, E. W.; Herwig, P.; de Leeuw, D. M. *Nature* **1999,** 401, (6754), 685-688.
15. Treat, N. D.; Brady, M. A.; Smith, G.; Toney, M. F.; Kramer, E. J.; Hawker, C. J.; Chabinyc, M. L. *Advanced Energy Materials* **2011,** 1, (1), 82-89.
16. Lyons, B. P.; Clarke, N.; Groves, C. *Energy & Environmental Science* **2012,** 5, (6), 7657-7663.
17. Groves, C. *Energy & Environmental Science* **2013,** 6, (11), 3202-3217.

18. Shaw, P. E.; Ruseckas, A.; Samuel, I. D. W. *Advanced Materials* **2008,** 20, (18), 3516-3520.
19. Kim, Y.; Choulis, S. A.; Nelson, J.; Bradley, D. D. C.; Cook, S.; Durrant, J. R. *Applied Physics Letters* **2005,** 86, (6), 063502-3.
20. McNeill, C. R.; Halls, J. J. M.; Wilson, R.; Whiting, G. L.; Berkebile, S.; Ramsey, M. G.; Friend, R. H.; Greenham, N. C. *Advanced Functional Materials* **2008,** 18, (16), 2309-2321.
21. Moulé, A. J.; Meerholz, K. *Advanced Functional Materials* **2009,** 19, (19), 3028-3036.
22. Amonoo, J. A.; Glynos, E.; Chen, X. C.; Green, P. F. *The Journal of Physical Chemistry C* **2012,** 116, (39), 20708-20716.
23. Mozer, A. J.; Sariciftci, N. S.; Lutsen, L.; Vanderzande, D.; Osterbacka, R.; Westerling, M.; Juska, G. *Applied Physics Letters* **2005,** 86, (11), 112104-3.
24. Drummy, L. F.; Davis, R. J.; Moore, D. L.; Durstock, M.; Vaia, R. A.; Hsu, J. W. P. *Chemistry of Materials* **2011,** 23, (3), 907-912.
25. Peumans, P.; Yakimov, A.; Forrest, S. R. *Journal of Applied Physics* **2003,** 93, (7), 3693-3723.
26. Marsh, R. A.; Hodgkiss, J. M.; Albert-Seifried, S.; Friend, R. H. *Nano Letters* **2010,** 10, (3), 923-930.
27. Yang, X.; van Duren, J. K. J.; Rispens, M. T.; Hummelen, J. C.; Janssen, R. A. J.; Michels, M. A. J.; Loos, J. *Advanced Materials* **2004,** 16, (9-10), 802-806.
28. Spano, F. C. *The Journal of Chemical Physics* **2005,** 122, (23), 234701-15.
29. Frank C, S. *Chemical Physics* **2006,** 325, (1), 22-35.
30. Clark, J.; Chang, J.-F.; Spano, F. C.; Friend, R. H.; Silva, C. *Applied Physics Letters* **2009,** 94, (16), 163306-3.
31. Pivrikas, A.; Sariciftci, N. S.; Juška, G.; Österbacka, R. *Progress in Photovoltaics: Research and Applications* **2007,** 15, (8), 677-696.
32. Scheblykin, I. G.; Yartsev, A.; Pullerits, T.; Gulbinas, V.; Sundström, V. *The Journal of Physical Chemistry B* **2007,** 111, (23), 6303-6321.
33. Keivanidis, P. E.; Clarke, T. M.; Lilliu, S.; Agostinelli, T.; Macdonald, J. E.; Durrant, J. R.; Bradley, D. D. C.; Nelson, J. *The Journal of Physical Chemistry Letters* **2010,** 1, (4), 734-738.
34. Zhang, Y.; Dang, X.-D.; Kim, C.; Nguyen, T.-Q. *Advanced Energy Materials* **2011,** 1, (4), 610-617.
35. Garcia-Belmonte, G.; Bisquert, J. *Applied Physics Letters* **2010,** 96, (11), 113301-3.
36. Ripolles, T. S.; Guerrero, A.; Garcia-Belmonte, G. *Applied Physics Letters* **2013,** 103, (24), 243306-5.
37. Montanari, I.; Nogueira, A. F.; Nelson, J.; Durrant, J. R.; Winder, C.; Loi, M. A.; Sariciftci, N. S.; Brabec, C. *Applied Physics Letters* **2002,** 81, (16), 3001-3003.
38. Nogueira, A. F.; Montanari, I.; Nelson, J.; Durrant, J. R.; Winder, C.; Sariciftci, N. S.; Brabec, C. *The Journal of Physical Chemistry B* **2003,** 107, (7), 1567-1573.
39. Nelson, J.; Choulis, S. A.; Durrant, J. R. *Thin Solid Films* **2004,** 451–452, (0), 508-514.

40. Adriaenssens, G. J.; Arkhipov, V. I. *Solid State Communications* **1997,** 103, (9), 541-543.
41. Koster, L. J. A.; Mihailetchi, V. D.; Blom, P. W. M. *Applied Physics Letters* **2006,** 88, (9), 093511-3.
42. Groves, C.; Greenham, N. C. *Physical Review B* **2008,** 78, (15), 155205.
43. Szmytkowski, J. d. *Chemical Physics Letters* **2009,** 470, (1–3), 123-125.
44. Mozer, A. J.; Sariciftci, N. S. *Chemical Physics Letters* **2004,** 389, (4-6), 438-442.
45. Huang, B.; Glynos, E.; Frieberg, B.; Yang, H.; Green, P. F. *ACS Applied Materials & Interfaces* **2012,** 4, (10), 5204-5210.
46. Bässler, H. *physica status solidi (b)* **1993,** 175, (1), 15-56.
47. Kim, M.-S.; Kim, B.-G.; Kim, J. *ACS Applied Materials & Interfaces* **2009,** 1, (6), 1264-1269.
48. Li, G.; Shrotriya, V.; Yao, Y.; Yang, Y. *Journal of Applied Physics* **2005,** 98, (4), 043704-5.
49. Ma, W.; Yang, C.; Gong, X.; Lee, K.; Heeger, A. J. *Advanced Functional Materials* **2005,** 15, (10), 1617-1622.

CHAPTER 4
POWER FACTOR DOUBLING IN STRAINED SILICON THIN FILMS WITH NANOMESH

4.1 INTRODUCTION

Thermoelectric materials can interconvert heat and electrical energy. Materials with high ZT > 1~2 are desired for highly efficient thermoelectric devices; such high ZTs are usually found in heavily doped semiconductors such as Bi_2Te_3, Sb_2Te_3 and PbTe.[1] Compared to these materials, the most studied semiconductor Si has several apparent advantages including its abundance on the Earth, its nontoxicity and easy integration into existent microelectronic and optoelectronic devices. However, silicon has only emerged as a promising thermoelectric material very recently.[2-4] The biggest challenge is the thermal conductivity κ of Si; at 300 K, $\kappa^{Si} \approx 150$ $Wm^{-1}K^{-1}$, leading to a very low $ZT \approx 0.01$. κ^{Si} has contributions from a variety of particles or quasiparticles including charge carriers (holes or electrons) and phonons (lattice vibrations),

$$\kappa_{total}^{Si} = \kappa_e^{Si} + \kappa_{ph}^{Si} \tag{4.1}$$

κ_e^{Si} can be estimated via the Wiedemann-Franz law

$$\kappa_e^{Si} = \sigma L T \tag{4.2}$$

$\boldsymbol{L} \approx 2.44\times10^{-8}$ $W\Omega K^{-2}$ is the Lorentz number. With high doping level (~10^{20} cm^{-3}), $\boldsymbol{\kappa_e^{Si}} \approx 1$ $Wm^{-1}K^{-1}$ at room temperature. So $\boldsymbol{\kappa_{total}^{Si}}$ is dominated by the phonon transport, which can also be evaluated by

$$\boldsymbol{\kappa_{ph}^{Si} = \frac{1}{3} Cvl} \tag{4.3}$$

where $\boldsymbol{C}$ is the specific heat capacity, $\boldsymbol{v}$ is the average phonon velocity and $\boldsymbol{l}$ is the phonon mean free path. For bulk silicon, the phonon mean free path ranges from 1 nm to 10 μm, more than 67% of which is above 100 nm.[5] Therefore, nanostructures with feature sizes under 100 nm may induce significant boundary scattering to phonons and effectively reduce the phonon contribution to $\boldsymbol{\kappa_{total}^{Si}}$. As a result, high $\boldsymbol{ZT}$s may be achieved in low-dimensional nanostructured silicon. For example, Boukai et al. demonstrated that the $\boldsymbol{\kappa_{total}^{Si}}$ was reduced to 0.76 $Wm^{-1}K^{-1}$ at 300 K in 10 nm wide silicon nanowires fabricated by the superlattice nanowire pattern transfer method.[2] Tang et al also showed that $\boldsymbol{\kappa_{total}^{Si}}$ was decreased to 1.9 $Wm^{-1}K^{-1}$ at 300 K in 100 nm thick holey silicon films with pitch of 55 nm fabricated by block copolymer (BCP) lithography.[4] While the power factors of these nanostructured silicon were kept comparable to that of the bulk silicon, such orders of magnitude reduction of $\boldsymbol{\kappa_{total}^{Si}}$ resulted in tremendous enhancement of $\boldsymbol{ZT}$; 20 nm wide silicon nanowires reached $\boldsymbol{ZT} \approx 1$ at 200 K, 10 nm wide silicon nanowires reached $\boldsymbol{ZT} \approx 0.6$ at 350 K and the holey silicon films achieved $\boldsymbol{ZT} \approx 0.4$ at 300 K.

While nanostructure engineering is demonstrated as a successful approach to reduce the thermal conductivity, it is challenging to further maximize $\boldsymbol{ZT}$ by decreasing

the characteristic sizes below 10 nm. The electron mean free path is below 10 nm for deeply doped silicon so feature size smaller than this scale may have a setback on the electric conductivity.[3, 6] Methods to increase the power factor are therefore being explored as an alternative. The most direct way to improve the electric conductivity is to tune the doping level. However, while heavier doping usually increase the electric conductivity according to

$$\sigma = ne\mu \tag{4.4}$$

where n is the carrier concentration and μ is the carrier mobility, the thermopower of heavily doped semiconductors has a negative dependence on carrier concentration

$$S = \frac{8\pi^2 k_B^2}{3eh^2} m^* T \left(\frac{\pi}{3n}\right)^{2/3} \tag{4.5}$$

where m^* is the effective mass of the carrier. So an optimal doping level is usually required for high power factor and ZT.[1] Besides tuning the carrier concentration, another effective way to enhance the power factor is to use strained silicon instead of unstrained one. Tensile strained silicon has been used in n-channel MOSFETs to increase electron mobility through the channel. This idea was first proposed and succeeded in Intel's 90 nm processing to improve the transistor performance by more than 10%.[7-9] The improvement in electron mobility leads to an increase in electrical conductivity, which was challenging to be tailored beyond desired doping level. Application of strained silicon to thermoelectrics has also been explored, but only on a theoretical calculation basis; experimental results proving the concept have not been reported to our best knowledge.

We hereby propose to use biaxial tensile strained silicon thin films to improve the power factor. Though the thermal conductivity is beyond the scope of this project, the power factor was still characterized in strained silicon thin films with nanomesh structure, which should possess a very low thermal conductivity. We hope the power factor results presented here can be referenced for full characterization of $\boldsymbol{ZT}$ in similar strained silicon thin films with nanomesh structure in the future. About 0.86% biaxial tensile strain was initially embedded in the silicon thin film; this level decreased to 0.80% after the nanomesh patterning. By incorporating such biaxial tensile strain into nanomesh silicon thin films, we achieved 300~500% enhancement in $\boldsymbol{\sigma}$ in the near room temperature range and doubled the power factor at 300 K.

4.2 EXPERIMENTAL SECTION

4.2.1 Materials

The strained silicon wafers were custom-made in Soitec and used as received. They are biaxial tensile strain silicon thin films with <100> orientation on insulator (SSOI, 14 nm strained Si/150 nm thermal SiO_x/680 μm Si) using the bond and etch back technology developed by T.S. Drake, et al.[10] Basically, silicon films were epitaxially grown on Si_xGe_{1-x} substrate. The larger lattice constant of Si_xGe_{1-x} forces the Si lattice constant to expand and consequently generate biaxial tensile strain in the thin films, as shown in Figure 4.1. As the Si film grows thicker, the substrate effect diminishes and new layers

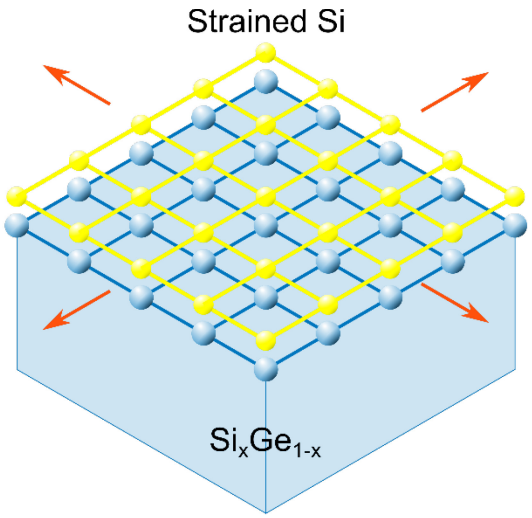

Figure 4.1 A scheme of epitaxially growing Si thin film on Si_xGe_{1-x} substrate. Red arrows indicate biaxial tensile strain induced by the discrepancy between lattice constants of Si and Si_xGe_{1-x}.

become unstrained. So strained silicon films can only made be on the order of 10 nm.

4.2.2 Experiments

4.2.2.1 Device fabrication

The strained silicon layer of each SSOI wafer was first doped with phosphorous using solid targets in rapid thermal annealing furnace at 900 °C for 2 min. A few nanometer thick layer of random copolymer PS-*r*-PMMA was then spincoated onto the top surface and thermally annealed at 190 °C for 17 hours to neutralize the surface. A thin film (~100 nm) of asymmetric BCP PS(46k)-b-PMMA(21k) was subsequently spincoated onto the surface to form vertically cylindrical nanostructures; PMMA cylinders have diameters of ~18 nm and the center to center distance between neighboring cylinders (pitch) is ~34 nm. After being annealed at 190°C for 12 hours, the SSOIs were irradiated with UV to crosslink the PS matrix and subsequently rinsed with acetic acid

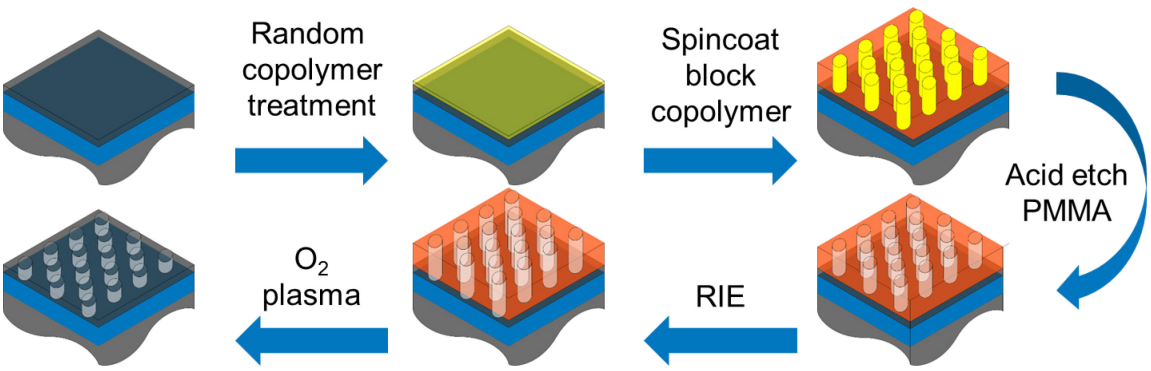

Figure 4.2 A scheme of patterning nanomesh structure onto strained silicon thin films using the BCP method.

and water to remove the PMMA cylinder cores. With PS as a nanomesh template, the samples were subjected to reactive ion etching (CF_4) to create nanomesh structure in the strained silicon thin film. Finally, the remaining PS was removed by O_2 plasma. The whole fabrication procedure is displayed in Figure 4.2.

4.2.2.2 Scanning Electron Microscopy

The scanning electron microscopy (SEM) was conducted on Hitachi SU8000 in-line SEM.

4.2.2.3 Confocal Raman Spectroscopy

The confocal Raman spectroscopy was conducted on an inVia Raman microscope (Renishaw). A laser light ($\lambda = 514\,nm$) and a 100× Leica microscopic objective was used to spatially filter the analysis volume of the samples to provide a spatial resolution of 0.5 μm.

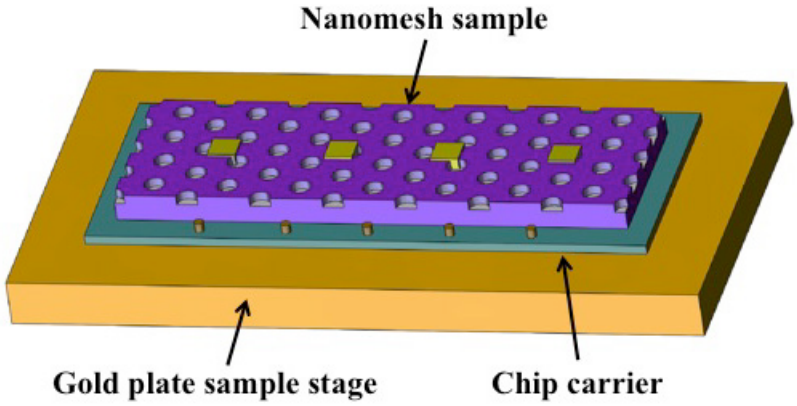

Figure 4.3 A scheme of four-point probe measurement of electrical conductivity of the strained silicon thin films with nanomesh.

4.2.2.4 Electrical Conductivity Measurement

For electrical conductivity, the four-point probe measurement was conducted on a SSOI device (2 inch×1 inch) as shown in Figure 4.3. The four contact pads (150 μm×150 μm) were defined by photolithography with 1000 μm spacing and Ti/Pt (10 nm/100 nm) was deposited using electron-beam evaporation at a base pressure of ~2×10^{-6} Torr. After the liftoff, the device was annealed in forming gas at 350 °C for 5 min. The strained silicon thin film on the edges of each SSOI device was etched away by XeF_2 to avoid electrical leakage from the top strained silicon layer to the silicon handle. The device was thermally attached to a chip carrier by silver paste. The four contact pads were then wire bonded to four pins on the chip carrier which was mounted to the sample stage of a cryostat (VPF-500, Janis). A sourcemeter (2400 SourceMeter, Keithley) was used to feed current through the outer two pins on the chip carrier and measure voltage between the

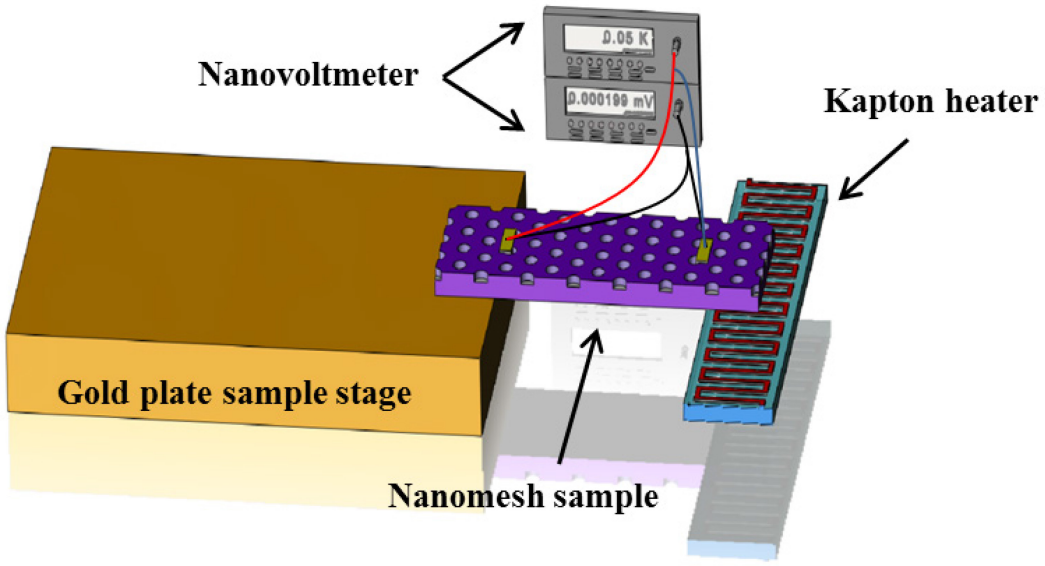

Figure 4.4 A scheme of thermopower measurement of strained silicon thin films with nanomesh.

inner two pins to characterize the strained silicon thin film sheet resistance. The sheet resistance was then converted into electrical conductivity.

4.2.2.5 Thermopower Measurement

The thermopower was measured in the same cryostat. Once a steady temperature gradient was established across the SSOI device, both temperature and voltage drops were measured simultaneously by two nanovoltmeters (2182A, Keithley) as shown in Figure 4.4. The left side of the device was attached to the sample stage of the cryostat and the right side was attached to a Kapton heater; the Kapton heater served as the heat source while the temperature controlled sample stage served as a heat sink. Similarly to the electrical conductivity measurement, two Ti/Pt (10 nm/100 nm) contact pads (5 mm×1 mm) were patterned about 1 cm apart on the strained silicon thin film with nanomesh via

electron beam evaporation at a base pressure of ~2×10^{-6} Torr, followed by the same forming gas annealing used in electrical conductivity sample preparation. Two pairs of twisted Ph-Br (Cu (94.8%), Sn (5%), Ph (.2%); OD 0.005 inch, polyimide insulation) wires were used for voltage measurement to lower the noise level. Two type-T (copper–constantan) thermocouples were soldered with indium onto the two contact pads to measure the temperature difference. A self-programmed Labview VI was utilized for voltage and temperature collection. The thermopower was measured in vacuum (10^{-6} Torr) environment to minimize heat loss through air conduction and convection and to prevent contamination from surrounding media.

4.3 RESULTS AND DISCUSSION

SEM images of the strained silicon thin films with nanomesh are shown in both top view (Figure 4.5(a)) and side view (Figure 4.5(b)). Figure 4.5(a) shows that the top strained silicon film was uniformly patterned with the hexagonally arranged nanomesh structure. The holes are ~18 nm in diameter and the pitch is ~34 nm, as shown in the Figure 4.5(a) inset; the porosity is calculated to be ~23%. These dimensions are inherited from the BCP template structure and may be tunable via varying the copolymer compositions. Figure 4.5(b) reveals the cross section of SSOI wafers in a tilted view. The top strained silicon layer is ~10 nm based on the contrast, which is confirmed by atomic force microscopy. It also shows that the nanomesh is completely etched through the top layer by reactive ion etching.

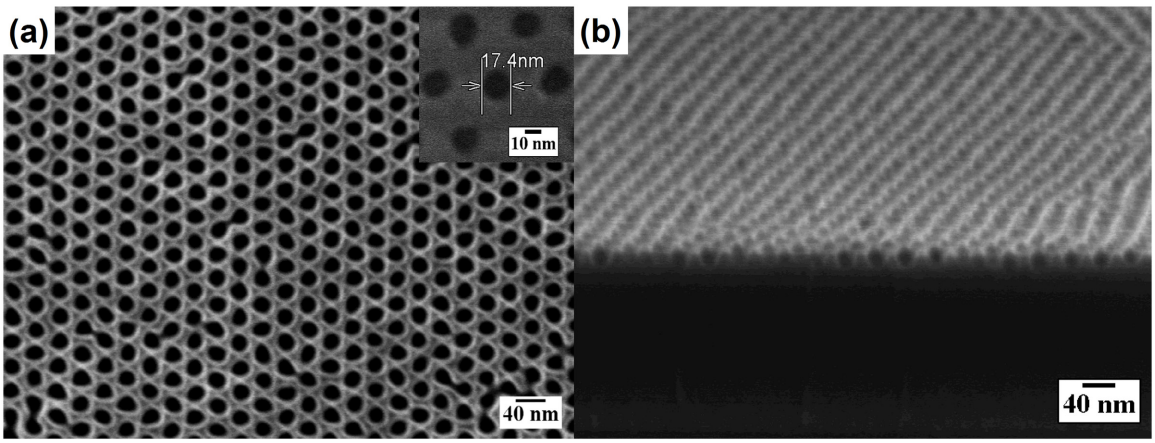

Figure 4.5 (a) top view and (b) cross section view of the strained silicon thin films after the nanomesh patterning.

The nanomesh pattern transfer to the strained silicon thin film may cause slight local strain relaxation due to breaking of strained Si bonding and creation of additional free surfaces. However, the net biaxial tensile strain in the nanomesh film is expected to be preserved by the underlying SiO_x layer. The magnitude of the net biaxial tensile strain before and after the nanomesh patterning was characterized using confocal Raman spectroscopy and normalized spectra are presented in Figure 4.6. In Figure 4.6a, spectrum of bulk silicon without nanomesh (solid curve) shows one major peak while spectra of strained silicon films without nanomesh exhibit an extra minor peak at a smaller wavenumber before (dash curve) and after (dash dot curve) the doping. These two peaks are associated with unstrained and strained silicon bonding, respectively, as labeled in the figure.[10] The unstrained Si peaks in the two spectra of the strained silicon films are attributed to the scattering from the silicon handle beneath the SiO_x layer.[11] The sandwiched SiO_x layer has a broad Raman peak beyond 2000 cm^{-1}, which is outside the detection range here.[12] Complete overlapping of these two spectra also suggests that

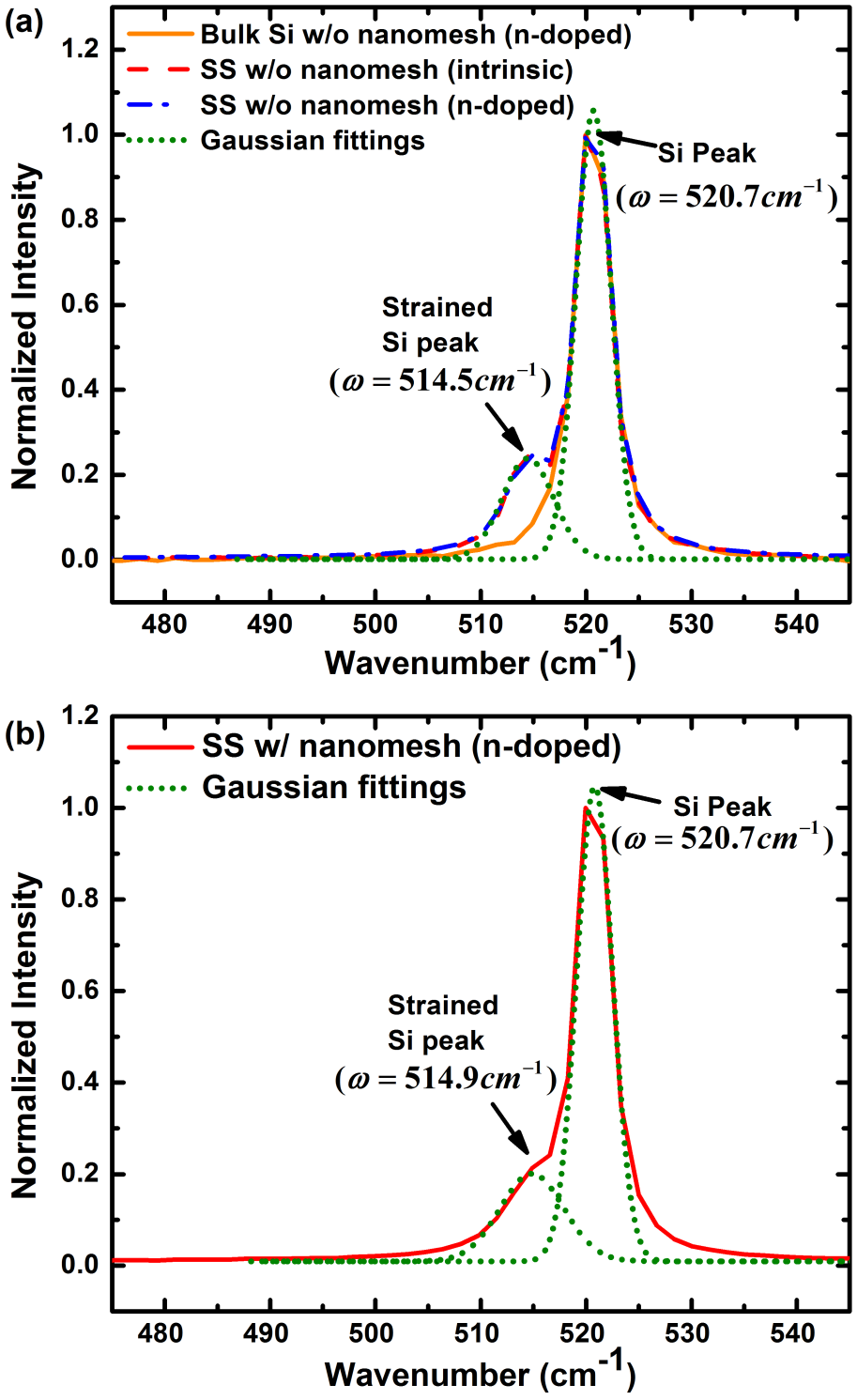

Figure 4.6 Confocal Raman spectra of strained silicon thin films (a) before and (b) after the nanomesh patterning.

doping with smaller phosphorus atoms does not affect the pre-existing biaxial tensile strain significantly. Gaussian fitting (dotted curves) of the strained silicon spectra reveals the positions of Si peak and strained Si peak to be 520.7 cm^{-1} and 514.5 cm^{-1}. The redshift of strained Si peak indicates a reduced energy barrier for photons to overcome and engage in inelastic Raman scattering, as a result of the biaxial tensile strain in silicon bonding. The wavenumber difference between these two peaks ($\boldsymbol{\Delta\omega}$) can be used to determine the strain level ($\boldsymbol{\varepsilon}$) in the strained silicon thin film using[10]

$$\boldsymbol{\varepsilon = 1.38 \times 10^{-3} \Delta\omega} \tag{4.6}$$

The strain level before nanomesh patterning is $\boldsymbol{\varepsilon} = 0.86\%$. The spectrum of doped strained silicon thin film with nanomesh is shown in Figure 4.6(b). A similar Gaussian fitting is performed, revealing the strained Si peak at 514.9 cm^{-1}. Using the same equation, the strain level is calculated to be 0.80%, which proves the expected weak relaxation of the biaxial tensile strain after nanomesh patterning. This level of strain has significant effects on the silicon band structure and improves electrical conductivity and power factor, as discussed below.

The electrical conductivity was characterized by the standard four-point probe method on both strained and unstrained silicon thin films for direct comparison. A correction factor of 1.5 determined by a COMSOL simulation, is also included to compensate for the inhomogeneity of the nanomesh film in measurement. The electrical conductivity $\boldsymbol{\sigma}$ is then determined by

$$\boldsymbol{\sigma = \frac{1.5}{dR_s}} \tag{4.7}$$

where $\boldsymbol{d}$ is the strained silicon nanomesh film thickness and

$$\boldsymbol{R_s = 4.53\frac{V}{I}} \tag{4.8}$$

is the sheet resistance, 4.53 being the correction factor for four-point probe measurement on thin films due to the geometrical confinement of the current.

Conductivities of the strained and unstrained silicon nanomesh thin films are shown in Figure 4.7a. Both films exhibit positive dependence of conductivity on temperature, indicating more electrons are excited to the conduction band at elevated temperature. More importantly, Figure 4.7a shows that the conductivity of the strained silicon thin film with nanomesh is approximately 4 times higher than that of the unstrained silicon thin film with nanomesh at 300 K; such substantial enhancement is throughout the entire temperature range from 230 K to 380 K. This is mostly attributed to the electron mobility enhancement due to conduction band splitting under biaxial tensile strain, as shown in the Figure 4.7a inset. In strained silicon, the six-fold degenerate conduction band minima (Δ_6) split into two groups under biaxial tensile strain, with two equivalent cross-plane valleys in [001] direction (Δ_2) shifting downwards and four equivalent in-plane valleys along [100] and [010] directions (Δ_4) shifting upwards. The energy gap between Δ_2 and Δ_4 is strain dependent and characterized to be ~125 meV for the 0.80% biaxial tensile strain level.[13] The conduction band splitting gives rise to enhanced electron mobility,

$$\boldsymbol{\mu = \frac{e\tau}{m^*}} \tag{4.9}$$

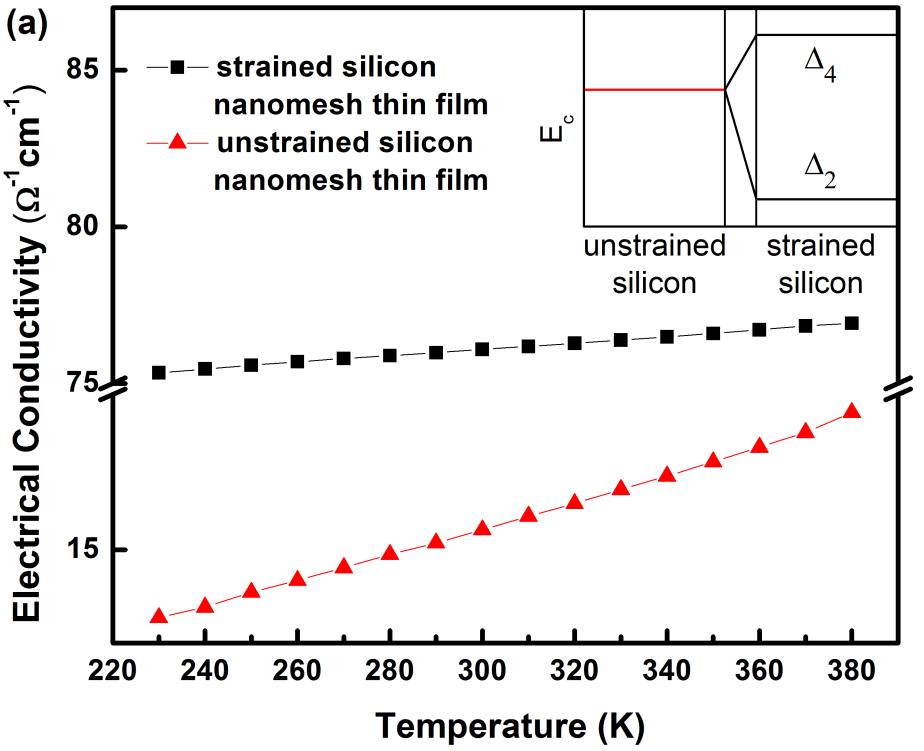
(a)
strained silicon nanomesh thin film
unstrained silicon nanomesh thin film
Electrical Conductivity ($\Omega^{-1}cm^{-1}$)
85
80
75
15
220
240
260
280
300
320
340
360
380
Temperature (K)
E_c
Δ_4
Δ_2
unstrained silicon
strained silicon

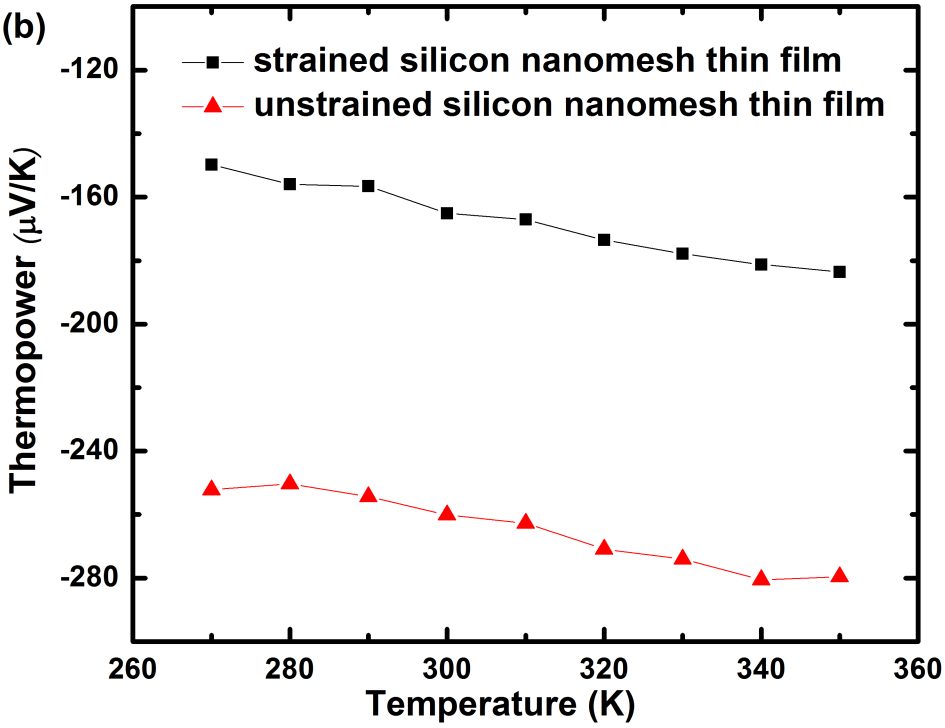
(b)
strained silicon nanomesh thin film
unstrained silicon nanomesh thin film
Thermopower (μV/K)
-120
-160
-200
-240
-280
260
280
300
320
340
360
Temperature (K)

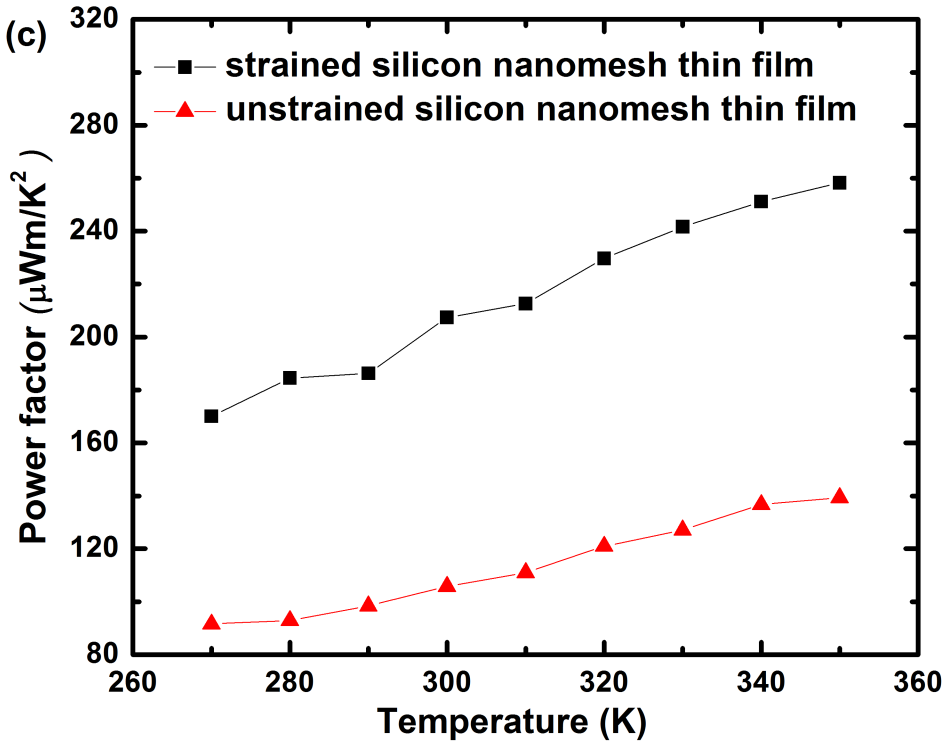

Figure 4.7 Temperature dependence of (a) electrical conductivity; (b) thermopower and (c) power factor of both unstrained and strained silicon thin films with nanomesh. Inset shows the conduction band splitting under the biaxia tensile strain.

due to reduced electron effective mass $\boldsymbol{m}^*$ and increased electron mean free scattering time $\boldsymbol{\tau}$.[14] In unstrained silicon, the effective mass is determined by the six equivalent ellipsoidal valleys,

$$\frac{6}{m^*} = \frac{4}{m_t} + \frac{2}{m_l} \tag{4.10}$$

where $\boldsymbol{m_l}$ = 0.93$\boldsymbol{m_0}$ is the longitudinal mass and $\boldsymbol{m_t}$ = 0.21$\boldsymbol{m_0}$ is the transverse mass. At sufficient strain level, the energy level of Δ_2 is lower than that of Δ_4 so electrons are redistributed to Δ_2; therefore only the transverse mass of the Δ_2 valleys contributes to the electron mobility.[15] The electron scattering time also increases due to the suppression of inter-valley elastic scattering with optical phonons, which results from strain induced

conduction band splitting.[16] The increased electron mobility gives rise to the 400% enhancement in the electrical conductivity of strained silicon thin film with nanomesh.

It is also shown that the temperature dependence of the electrical conductivity of the strained silicon thin film with nanomesh is weaker than that of the unstrained one. As for the temperature dependence,

$$\sigma \propto \exp\left(-\frac{E}{2k_B T}\right) \tag{4.11}$$

for doped semiconductors with the energy gap E between the dopant level and the conduction band serving as the activation energy. Fitting of the unstrained silicon data gives $E \approx 0.041$ eV, which is consistent with the phosphorus doping.[17] Similarly, E is estimated to be 0.002 eV for the strained silicon film. Such energy gap difference 0.039 eV is due to the aforementioned conduction band splitting and confirmed by high-resolution soft X-ray absorption spectroscopy.[18] For strained silicon thin films with nanomesh, the conduction band splitting results in weaker temperature dependence. It is also noticeable that our electrical conductivity values are an order of magnitude lower than those reported by another group.[4] This is primarily because our doping level 4×10^{17} cm^{-3} (from Hall measurement) is two orders lower than their doping level. With higher doping level, we expect to see larger electrical conductivity enhancement in strained silicon films.

Thermopower was further examined on these films. The measured thermopower was negative because electron was the dominant charge carrier in n-typed doped films (Figure 4.7b). In both films, the thermopower actually goes to higher absolute values

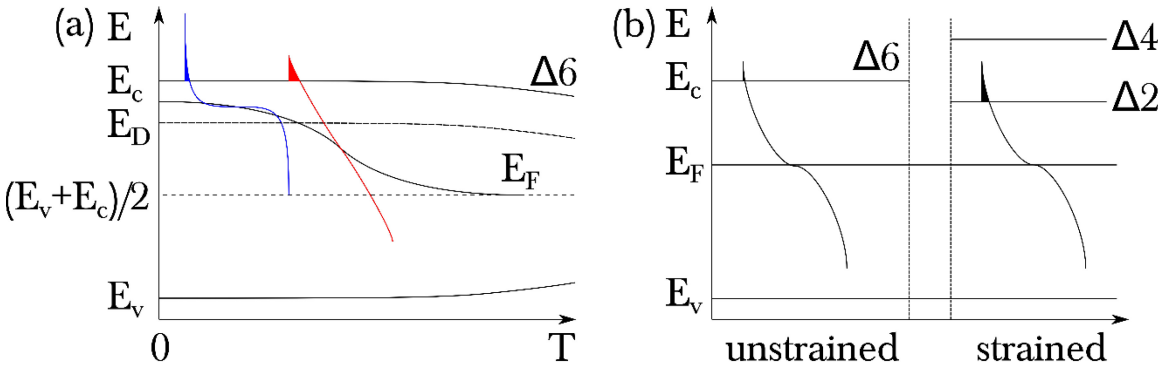

Figure 4.8 Schemes of influences of (a) temperature and (b) biaxial tensile strain on the energy distribution of transport electrons.

almost linearly as the temperature increases. A similar trend has also been experimentally observed from 150 K to 300 K in a 100 nm thick, 55 nm pitch silicon nanomesh thin film.[4] Such positive correlation between the thermopower and temperature can be recovered for different doping levels using an *ab initio* method and explained by the Boltzmann transport model under the relaxation time approximation.[15] Essentially, it is suggested that a narrow distribution of the energy of the electrons participating in the transport renders a good thermopower.[19] So as the Fermi level gradually shifts to the middle of the energy gap with increasing temperature, the energy distribution of electrons in the conduction band narrows (Figure 4.8a) and the thermopower improves. Moreover, the thermopower of strained silicon thin film with nanomesh exhibits a 36.5% reduction compared with the unstrained sample at 300 K. The reduction is also consistent with the *ab initio* calculation where the thermopower is expected to drop in biaxial tensile strained silicon.[15] From the perspective of energy distribution, the lowered Δ_2 broadens the energy distribution of conduction electrons (Figure 4.8b) so the thermopower is

reduced. Saturation of the thermopower would be observed under sufficient strain when all the electron occupation states in Δ_4 valleys are transferred to Δ_2 valleys.

The power factors $\boldsymbol{S^2\sigma}$ for both strained and unstrained silicon thin films with nanomesh were compiled based on the electrical conductivity and thermopower results. Figure 4.7c shows that there is a ~100% increase in the power factor for the strained silicon thin film with nanomesh at 300 K compared with that of the unstrained silicon thin film as a result of the significant electrical conductivity enhancement. Besides the biaxial tensile strain level, the power factor also depends on the doping concentration. For the 0.8% tensile strain silicon in this study, the power factor may be maximized with a doping concentration of 10^{20} cm^{-3}.[1]

4.4 CONCLUSIONS

This study for the first time demonstrates the great potential of biaxial tensile strained silicon for thermoelectric applications. At the doping level of 4×10^{17} cm^{-3}, strained silicon thin film with nanomesh exhibited ~400% enhancement in electrical conductivity but a ~36% reduction in thermopower compared to unstrained silicon thin film with nanomesh at 300 K. Both changes are attributed to the conduction band splitting under biaxial tensile strain. As a combined result, the power factor is almost doubled. Such a high power factor, together with greatly reduced thermal conductivity associated with the nanomesh structure, is expected to deliver several fold increase in $\boldsymbol{ZT}$. It provides a perspective to further increase thermoelectric efficiency when using the "phonon-glass electron-crystal" approach.[20, 21]

4.5 REFERENCES

1. Snyder, G. J.; Toberer, E. S. *Nat Mater* **2008,** 7, (2), 105-114.
2. Boukai, A. I.; Bunimovich, Y.; Tahir-Kheli, J.; Yu, J.-K.; Goddard Iii, W. A.; Heath, J. R. *Nature* **2008,** 451, (7175), 168-171.
3. Hochbaum, A. I.; Chen, R.; Delgado, R. D.; Liang, W.; Garnett, E. C.; Najarian, M.; Majumdar, A.; Yang, P. *Nature* **2008,** 451, (7175), 163-167.
4. Tang, J.; Wang, H.-T.; Lee, D. H.; Fardy, M.; Huo, Z.; Russell, T. P.; Yang, P. *Nano Letters* **2010,** 10, (10), 4279-4283.
5. Esfarjani, K.; Chen, G.; Stokes, H. T. *Physical Review B* **2011,** 84, (8), 085204.
6. Hippalgaonkar, K.; Huang, B.; Chen, R.; Sawyer, K.; Ercius, P.; Majumdar, A. *Nano Letters* **2010,** 10, (11), 4341-4348.
7. Thompson, S.; Anand, N.; Armstrong, M.; Auth, C.; Arcot, B.; Alavi, M.; Bai, P.; Bielefeld, J.; Bigwood, R.; Brandenburg, J.; Buehler, M.; Cea, S.; Chikarmane, V.; Choi, C.; Frankovic, R.; Ghani, T.; Glass, G.; Han, W.; Hoffmann, T.; Hussein, M.; Jacob, P.; Jain, A.; Jan, C.; Joshi, S.; Kenyon, C.; Klaus, J.; Klopcic, S.; Luce, J.; Ma, Z.; McIntyre, B.; Mistry, K.; Murthy, A.; Nguyen, P.; Pearson, H.; Sandford, T.; Schweinfurth, R.; Shaheed, R.; Sivakumar, S.; Taylor, M.; Tufts, B.; Wallace, C.; Wang, P.; Weber, C.; Bohr, M. In *A 90 nm logic technology featuring 50 nm strained silicon channel transistors, 7 layers of Cu interconnects, low k ILD, and 1 /spl mu/m/sup 2/ SRAM cell*, Electron Devices Meeting, 2002. IEDM '02. International, 8-11 Dec. 2002, 2002; 2002; pp 61-64.
8. Ghani, T.; Armstrong, M.; Auth, C.; Bost, M.; Charvat, P.; Glass, G.; Hoffmann, T.; Johnson, K.; Kenyon, C.; Klaus, J.; McIntyre, B.; Mistry, K.; Murthy, A.; Sandford, J.; Silberstein, M.; Sivakumar, S.; Smith, P.; Zawadzki, K.; Thompson, S.; Bohr, M. In *A 90nm high volume manufacturing logic technology featuring novel 45nm gate length strained silicon CMOS transistors*, Electron Devices Meeting, 2003. IEDM '03 Technical Digest. IEEE International, 8-10 Dec. 2003, 2003; 2003; pp 11.6.1-11.6.3.
9. Mistry, K.; Armstrong, M.; Auth, C.; Cea, S.; Coan, T.; Ghani, T.; Hoffmann, T.; Murthy, A.; Sandford, J.; Shaheed, R.; Zawadzki, K.; Zhang, K.; Thompson, S.; Bohr, M. In *Delaying forever: Uniaxial strained silicon transistors in a 90nm CMOS technology*, VLSI Technology, 2004. Digest of Technical Papers. 2004 Symposium on, 15-17 June 2004, 2004; 2004; pp 50-51.
10. Drake, T. S.; Chléirigh, C. N.; Lee, M. L.; Pitera, A. J.; Fitzgerald, E. A.; Antoniadis, D. A.; Anjum, D. H.; Li, J.; Hull, R.; Klymko, N.; Hoyt, J. L. *Journal of Elec Materi* **2003,** 32, (9), 972-975.
11. Temple, P. A.; Hathaway, C. E. *Physical Review B* **1973,** 7, (8), 3685-3697.
12. Popovic, D. M.; Milosavljevic, V.; Zekic, A.; Romcevic, N.; Daniels, S. *Applied Physics Letters* **2011,** 98, (5), -.
13. Euaruksakul, C.; Li, Z. W.; Zheng, F.; Himpsel, F. J.; Ritz, C. S.; Tanto, B.; Savage, D. E.; Liu, X. S.; Lagally, M. G. *Physical Review Letters* **2008,** 101, (14), 147403.
14. Schäffler, F. *Semiconductor Science and Technology* **1997,** 12, (12), 1515.

15. Hinsche, N. F.; Mertig, I.; Zahn, P. *Journal of Physics: Condensed Matter* **2011,** 23, (29), 295502.
16. Vogelsang, T.; Hofmann, K. R. *Applied Physics Letters* **1993,** 63, (2), 186-188.
17. Solymar, L.; Walsh, D.; Knovel, *Electrical properties of materials*. Oxford University Press: Oxford ; New York, 2010; p 1 online resource (xvi, 443 p.).
18. Euaruksakul, C.; Chen, F.; Tanto, B.; Ritz, C. S.; Paskiewicz, D. M.; Himpsel, F. J.; Savage, D. E.; Liu, Z.; Yao, Y.; Liu, F.; Lagally, M. G. *Physical Review B* **2009,** 80, (11), 115323.
19. Mahan, G. D.; Sofo, J. O. *Proceedings of the National Academy of Sciences* **1996,** 93, (15), 7436-7439.
20. Yu, J.-K.; Mitrovic, S.; Tham, D.; Varghese, J.; Heath, J. R. *Nat Nano* **2010,** 5, (10), 718-721.
21. Li, X.; Maute, K.; Dunn, M. L.; Yang, R. *Physical Review B* **2010,** 81, (24), 245318.

CHAPTER 5

CONCLUSIONS AND OUTLOOK

Conjugated polymer thin film systems for photovoltaic application and strained silicon thin film system for thermoelectric application are studied in this thesis. Various electrical transport properties in the conjugated polymer system (charge carrier density, non-geminate recombination and carrier mobility) and in the strained silicon system (electrical conductivity, thermopower and power factor) were investigated in conjunction with full characterization of film morphology with feature sizes of tens to hundreds of nanometers (aggregation size and orientation, domain size, phase purity, tensile strain level). Such feature sizes are on the same dimension scale of materials' intrinsic physical property (exciton diffusion length, phonon mean free path) and may affect the transport properties tremendously. The investigation results bestowed us better understanding of the film morphology effect on the electrical transport in those systems, which can further guide the design for superior device performance ($\boldsymbol{J_{SC}, V_{OC}, FF, PCE, ZT}$). Specifically:

In chapter 2, we utilized ToF and CELIV to demonstrate an order of magnitude monotonic enhancement in the out-of-plane hole mobility (7.1×10^{-5} $cm^2V^{-1}s^{-1}$ to 8.6×10^{-4} $cm^2V^{-1}s^{-1}$) in pristine P3HT thin films as the film thickness increases from 80 nm to about 700; the mobility saturates at that value at thicknesses beyond. XRD showed a slight increase in the P3HT aggregate size, which may partially contribute to the mobility improvement. SE revealed a similar varying trend of the film anisotropy degree as the mobility, from much negative degree (film being highly anisotropic) in thin films to almost zero degree (film being isotropic) in thick films. Combination of XRD and SE rendered a morphological image that more and more P3HT aggregates take the face-on orientation as the film becomes thicker and the substrate induced preference of edge-on

orientation fades. Increasing ratio of face-on P3HT aggregates facilitates the carrier transport in the direction normal to the substrate and gives rise to the order of magnitude enhancement in the out-of-plane hole mobility.

In chapter 3, we employed EFTEM and UV-vis spectroscopy to investigate domain sizes and phase purities in three fundamentally different morphologies of the P3HT:PCBM (1:1) system, which were created by solvent casting, thermal annealing and $scCO_2$ processing. Domain is greatly coarsened by thermal annealing while $scCO_2$ processing hardly enlarges the domain size; interfacial areas are thus much larger in the as-cast and $scCO_2$ processed samples than in the thermal annealed samples. $scCO_2$ processing and thermal annealing both improve the phase purity and increase the P3HT polymer conjugation length. Morphological features were reconciled with electrical transport properties probed by photo-CELIV, which were further linked with device performance. Large interfacial areas gives high initial carrier density and high phase purity improves carrier mobility in the $scCO_2$ processed sample, which synergistically leads to the highest $\boldsymbol{J_{SC}}$ among three morphologies. Long P3HT conjugation length induced by $scCO_2$ processing and thermal annealing narrows the gap between the carrier quasi-Fermi levels and results in lower $\boldsymbol{V_{OC}}$ in those samples. High recombination rate resulting from large interfacial areas in the as-cast and $scCO_2$ samples yields low $\boldsymbol{FF}$.

In chapter 4, we used BCP method to pattern the nanomesh structure into the strained silicon thin films. Confocal Raman spectroscopy revealed that the biaxial tensile strain level decreased from 0.86% to 0.80% with the nanomesh patterning. Conduction band splitting induced by the remaining strain gives rise to reduction of the electron effective mass and addition to the inter-valley scattering time. The electrical conductivity therefore increases 300%-500% in the strained silicon films compared to unstrained ones. Band splitting also widens the energy distribution of transport electrons and decreases the thermopower by 30%-40%. The overall power factor is thus doubled in the near-room-temperature range.

The outlook of conjugated polymer systems for photovoltaic application is very bright as the $\boldsymbol{PCE}$ of state-of-the-art polymer solar cells is steadily advancing towards 15%

with emerging polymers of superior properties. Polymers that can deliver better chemical properties like tunable band gap or better physical properties like controllable self-assembly are being synthesized and tailored to need. Structure-property study in these new material system are certainly desired for scientific understanding of material physics and chemistry, which in return can be used as prediction and guidance for materials with excellent performance.

On the other hand, with inherently low thermal conductivity ($\boldsymbol{\kappa} \approx 0.2$ $Wm^{-1}K^{-1}$) and electrically semiconducting property, conjugated polymers are a natural candidate for near room temperature thermoelectric applications. Some pioneer works have been done, demonstrating that by tuning carrier concentration with doping, $\boldsymbol{ZT} = 0.42$ at room temperature can be achieved in PEDOT. Meanwhile, more other conjugated polymers like P3HT are being investigated for thermoelectrics. Compared to organic photovoltaics, organic thermoelectrics is more an uncharted territory, which is worth deeper exploration.